UNIVERSITY OF OKLAHOMA

GRADUATE COLLEGE

A MOLECULAR DYNAMICS STUDY OF SPATIAL FLUID DISTRIBUTION IN MIXED-WET SHALE NANOPORES

A THESIS

SUBMITTED TO THE GRADUATE FACULTY

in partial fulfillment of the requirements for the

Degree of

MASTER OF SCIENCE

By

CHANGJAE KIM
Norman, Oklahoma
2020

A MOLECULAR DYNAMICS STUDY OF SPATIAL FLUID DISTRIBUTION IN MIXED-WET SHALE NANOPORES

A THESIS APPROVED FOR THE
MEWBOURNE SCHOOL OF PETROLEUM AND GEOLOGICAL ENGINEERING

BY THE COMMITTEE CONSISTING OF

Dr. Deepak Devegowda, Chair

Dr. Ali Ousseini Tinni

Dr. Liangliang Huang

I give thanks to God who show your love and grace to me through the entire journey in United States. This thesis is also dedicated to my parents, Jin-young and Mi-ja Kim, my wife, Hye-lin Youn, and my parents-in-law, Changseok and Kyungdeok Youn, whose support has been unfaltering and enthusiastic, even when it was not easy to give it.

ACKNOWLEDGEMENTS

Most of all, I really appreciate God whose grace allowed me to endure hardships due to the pandemic situation. Some difficulties to my family and my parents pained me but you lightened the way to overcome the problems and I realized that you did not let me stray from your arms. I am thankful for the support of my wife, Hyelin Youn, who has supported me unconditionally and respected me. Without her, none of this would have been possible. She keeps me warm when I am burdened and weak under the pressure of managing my work and taking care of my family. She is the most precious person to me whom I can give everything. I am also blessed to have my son, Aaron Wonjae Kim, during this pandemic situation. His existence keeps me from being discouraged and gives my life reason. With my family, I am optimistic for the journey in my life.

I give thanks to my parents, Jin-young and Mi-ja Kim for they have devoted their lives to raise me and my younger sister despite the hardships in their life. Their reckless love and support has made me look at the world full of happiness. I am also thankful to my parents-in-law, Changseok and Kyungduk Youn. They love me like their own son and lavish me with support and affection. Their Christian life is a role model for me and my wife to emulate. I am thankful for my younger sister, Ji-won Kim, who encouraged me to face the challenge of studying abroad and took care of my parents instead of me. I thank my sister-in law and her husband, Aelin Youn and Hamin Choi, who has supported my family and stayed by our side.

I am really grateful for the support of Dr. Deepak Devegowda. He gave me the opportunity to study at the University of Oklahoma, one of the most outstanding universities in Petroleum Engineering. I could not have reached this moment without his careful mentorship and support in my academic journey and life.

I would like to thank my committee members, Dr. Ali Tinni and Dr. Liangliang Huang. They provided informative comments and discussions in the classroom and research meetings for my research works.

I give thanks to my colleagues, Dr. Felipe Perez and Hao Xiong. Apart from academic discussion, they truly listened to my life and shared both joys and sorrows. I am delighted to have them by my side.

Additionally, I would like to thank Dr. Jeonghwan Lee, my academic advisor at Chonnam National University. His thoughtful guidance in my studies and life has let me experience the pleasure of achievement under challenging situations.

Finally, I am grateful to the University of Oklahoma's Mewbourne School of Petroleum and Geological Engineering for their longstanding support. The family-like atmosphere and great care helpd me finalize my studies. I will not forget my time from the beginning to the end of my journey in Norman.

TABLE OF CONTENTS

LIST OF TABLES

LIST OF FIGURES

ABSTRACT

Mixed wet pores are abundant in shales, yet there is little to no information on the behavior of fluids confined within pores characterized by one hydrophilic and one hydrophobic surface. This mixed wettability can impact fluid storage, distribution, capillary pressures and transport through these pores. In this study, I use molecular dynamics simulations to describe the initial distribution of reservoir fluids, such as multicomponent oils and water, in pores of mixed wettability. This is an essential pre-requisite to additional studies documenting fluid transport in such pores.

The molecular model of the mixed wet pore used in this study consists of kerogen separated by some distance from a clay surface. Molecular dynamics (MD) provides the spatial distribution of water and the individual hydrocarbon species, at varying values of water concentration. In a series of additional sensitivity studies, I also evaluate the impact of salinity on the distribution of these fluids for two different arrangements of charged clay surface that are denoted as hydroxyl-potassium (H-P) and potassium-potassium (P-P) surfaces.

Throughout the entire study, the results from the equilibrated system indicate a high affinity between the heavy components, such as the asphaltene/resin fraction and the kerogen surfaces, which is to be expected. The more surprising result is the hydrogen bonding observed between the polar constituents in the asphaltene/resin fraction and water. This creates a situation where the asphaltene/resin fraction shows an affinity towards water and resides adjacent to the water adsorbed on to the clay surface. When this happens, the hydrophilic clay surface effectively becomes hydrophobic. A pore bounded by an asphaltene layer on one side and kerogen on the other is more oil-wetting than mixed-wet. The presence of asphaltenes can therefore expect to create conditions of modified wettability that will impact oil recovery, oil transport and distribution.

Another surprising result in this work is that water forms structures that bridge between opposing surfaces of the model. These water bridges are seen to happen for water concentration values larger than 20%. In other words, water is not merely just adsorbed on to the clay surfaces, but also forms these bridge-like structures. However, when the salinity is even moderately increased, the water bridges dissipate, and water only occurs as an adsorbed phase or as a free fluid droplet. Nevertheless, I still observe a strong affinity between the asphaltene/resin fraction and water leading to a lesser degree of mixed wettability.

This study is the first, to the best of my knowledge, that considers water and multicomponent hydrocarbon mixtures in mixed-wet pores with realistic surface chemistry and constitutes a necessary first-step towards additional studies related to water and hydrocarbon transport and EOR processes in shale nanopores.

CHAPTER 1. INTRODUCTION

Shales are characterized by complex pore networks and spatially heterogeneous mineralogy with organic and inorganic matter as shown in Figure 1.1. A large percentage of shale nanopores are associated with the organic matter because of the thermal maturation process leading to the formation of hydrocarbons and the accompanying development of porosity. (Curtis et al., 2010; Sondergeld et al., 2010; Wei and Qin, 2013). The sizes of the nanopores in the organics commonly range from 5 to 100 nm, and their shapes include irregular, bubble-like, or elliptical cross sections (Loucks et al., 2009; Ougier-Simonin et al., 2016). In addition, microfractures are highly prevalent, mostly resulting from the maturation of organic matter and dehydration of clay minerals and play an important role in fluid transport.

The inorganic material in shales, such as clays, quartz, calcite, pyrite, feldspar and others are considered to be water-wet while the organic pores are generally considered to be oil-wet (Loucks et al., 2009; Sondergeld et al., 2010; Shi et al., 2013; Ougier-Simonin et al., 2016). There are, however, a few recent studies that suggest that the degree of hydrophobicity of organic pores directly increases with the degree of thermal maturity (Hu et al., 2014; Jagadisan and Heidari, 2019).

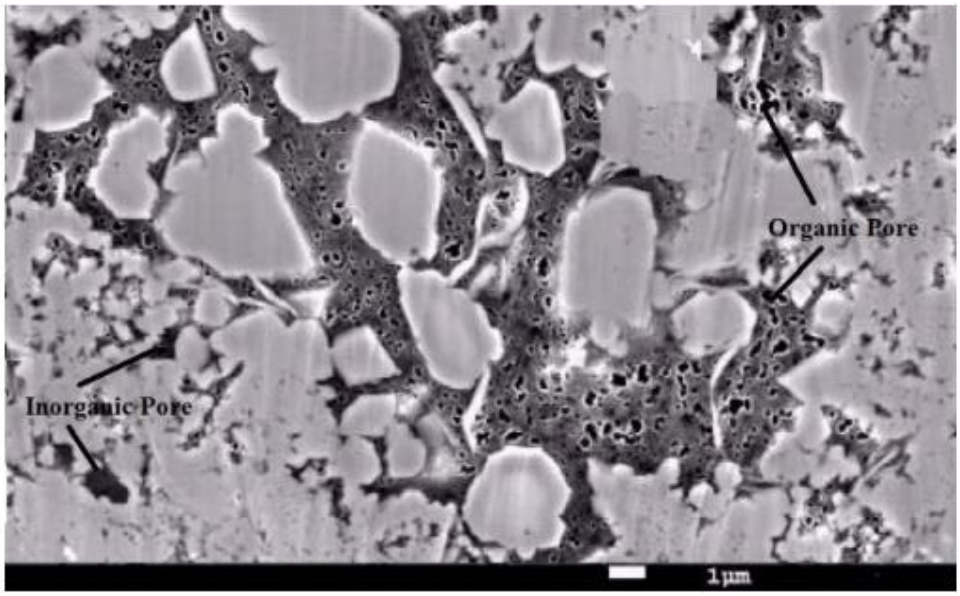

Figure 1.1. SEM image of organic/inorganic pores in shale rocks (Passey et al., 2010).

With the abundance of nanoscale-sized pores in shales, molecular dynamics (MD) simulations have become increasingly popular to describe the behavior of fluid molecules in nano- and micro-scale pores (Ambrose et al., 2012; Didar and Akkutlu, 2013; Alharthy et al., 2016; Perez and Devegowda, 2019; Baek and Akkutlu, 2019). In general, work addressing storage, PVT and transport in organic nanopores belongs to two broad groups: those using graphene-slit pore models and latter approaches that use more realistic kerogen models.

While graphene slit pores have proven useful for the study of fluid distribution in kerogen, they lack the correct pore surface chemistry and structure of kerogen. However, these initial attempts with graphite slit-pores demonstrate that the storage of single- and multi-component hydrocarbons is significantly different from conventional pore systems and show that molecular dynamics simulations are indeed warranted, simply because direct experimental observation is not possible at these length scales.

One of the earlier studies by Ambrose et al (2012) relied on the use of graphene slit pore models to investigate gas adsorption and gas density profiles for different pore widths at reservoir conditions. They report the presence of an adsorbed phase whose density varies with pressure and that is often significantly higher than the bulk fluid, thereby contributing to a considerable amount of fluid storage. Zhu and Zhao (2015) use carbon nanotube (CNT) models to investigate adsorption of methane in shale gas reservoirs and report similar results. They also indicate that for large pore widths, multilayer adsorption becomes more prevalent. In another paper, Mosher et al (2013) estimate the excess adsorption of methane in stacked carbon slit pores at subsurface conditions by using the grand canonical Monte Carlo (GCMC) simulations. They report that smaller pore sizes reach adsorption density peaks more rapidly compared to the larger pore sizes.

Wu et al. (2015), on the other hand, generate carbon nanochannel models to address competitive adsorption of gas components in kerogen nanopores. They observe the desorption of methane by carbon dioxide and nitrogen. Jin (2018) conduct a canonical Monte Carlo (CMC) test to examine the distribution of multicomponent hydrocarbons ($C_1/C_3/nC_5$) with and without confinement and show that the heavier components preferentially adsorb to the pore surfaces under confinement while not impacting the distribution of the lighter components.

An interesting aspect of hydrocarbon storage in very small pores is the 'pore-proximity' effect where pore surfaces play a significant role in governing fluid PVT behavior. Sapmanee (2011) was the first, to our knowledge, to report this effect in shales, followed by Devegowda et al in 2012. They use the results of MD simulations from Singh et al. (2009) to adjust the critical properties of various hydrocarbons to account for fluid confinement in nanopores. They report a substantial reduction in fluid saturation pressures for confined oils and gases. This has since been reported by several other authors. Didar and Akkutlu (2013), for example, study multicomponent gas PVT in

carbon slit pores. They report that the confinement effect causes phase envelope shifts as pore size decreases. Alharthy et al (2016) use a similar approach as Devegowda et al. (2012) to describe the physical properties of hydrocarbons and also report that the confinement effect lowers the bubble point pressure (Figure 1.2).

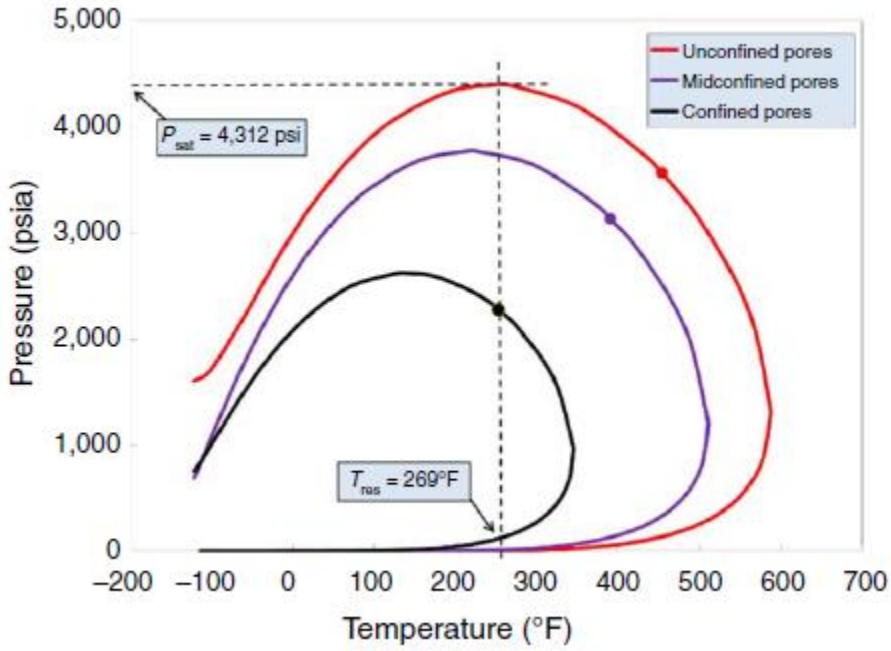

Figure 1.2. Phase envelope of bubblepoint fluid system in confined-, midconfined-, and unconfined nanopores (Alharthy et al., 2016).

Using molecular dynamics, Welch and Piri (2015) investigate retrograde condensation under nanopore confinement and report capillary condensation of the larger hydrocarbons that can impede flow even with a high-pressure gradient (Figure 1.3). Baek and Akkutlu (2019) construct multiscale graphite pore structures saturated with multicomponent hydrocarbons to provide information about the hydrocarbon distribution in nanoscale shale pores. Their simulation work indicates that a decrease of pore size leads to interpore compositional variations where smaller pores host heavier hydrocarbon mixtures (Figure 1.4).

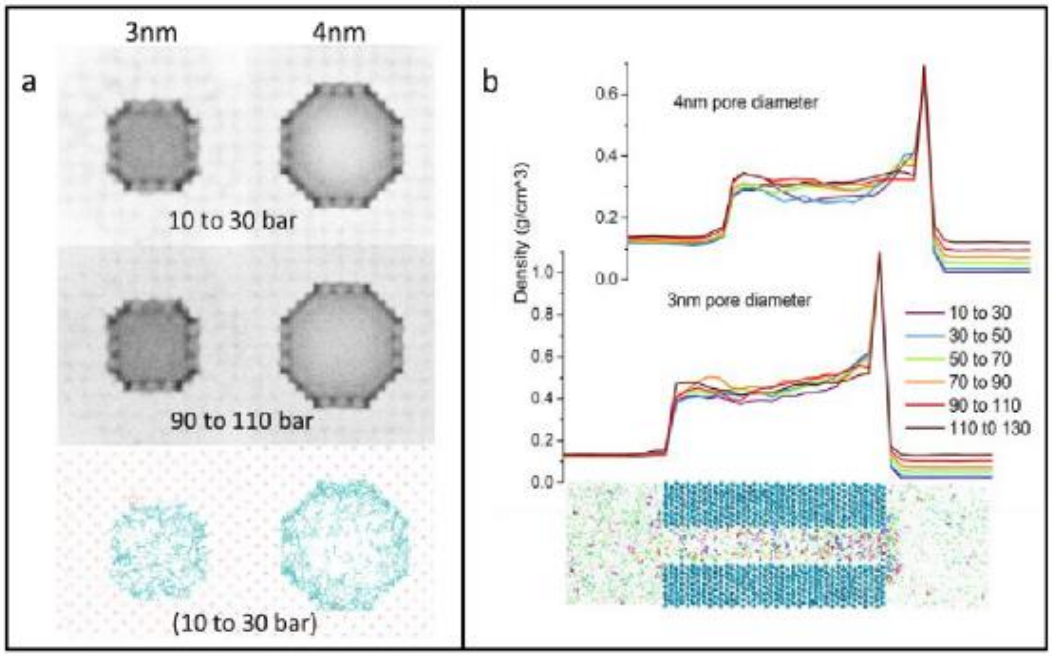

Figure 1.3. Density distribution of hydrocarbons in carbon nanotubes with pore sizes of 3 and 4 nm. (a) shows average density distribution of hydrocarbon fluid along the cross section of nano capillary tube after equilibration and (b) presents density profile along the pore axis under different pressure gradients (Welch and Piri, 2015).

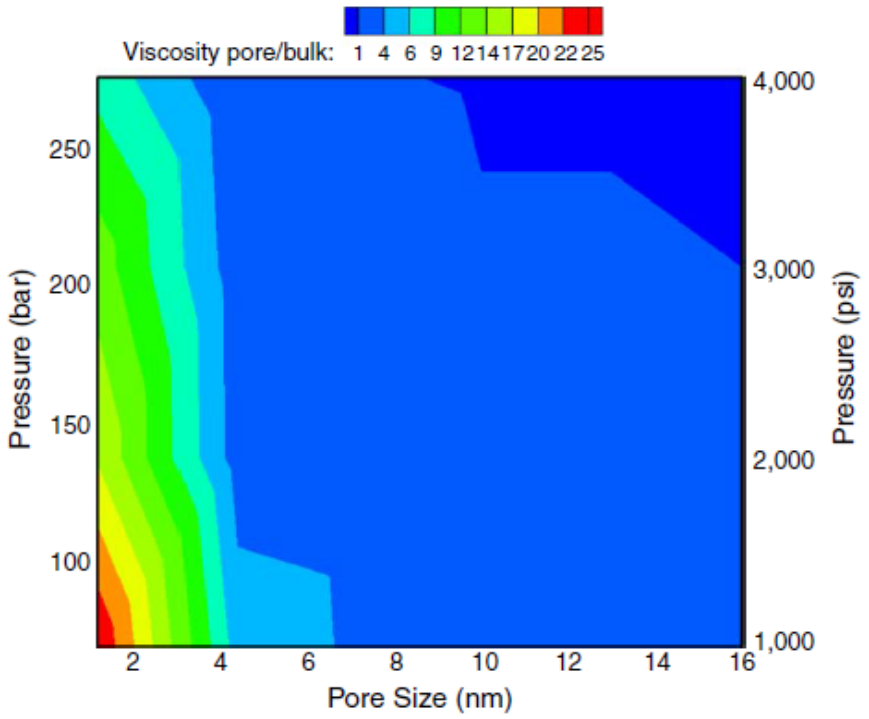

Figure 1.4. Viscosity of redistributed hydrocarbons in multiscale pore structure relative to its bulk viscosity (Baek and Akkutlu, 2019).

Because graphene slit-pore models do not represent realistic kerogen surfaces and surface chemistries, several researchers have resorted to constructing more representative kerogen models (Striolo et al., 2003; Hu et al. 2014; Diaz-Campos and Hobson, 2014; Ungerer et al., 2015; Jin, 2018; Feng and Akkutlu 2019). For example, Ungerer et al. in 2015 create molecular models representing different types of kerogen during the maturation process. The thermodynamic properties of their kerogen models show good agreement with experimental data obtained from realistic kerogen across a wide range of maturities and organic types.

In dealing with hydrocarbon storage in organic nanopores, Collell et al. (2014) compare theoretical models of adsorption with GCMC simulation to highlight the mechanisms of single- and multi-component adsorption in kerogen. Their comparison study generally shows good

agreement between the adsorption isotherms and molecular simulations, especially at lower values of pressure. Pathak et al. (2017) characterize the swelling behavior of type II kerogen in response to increases in hydrocarbon volume using two types of MD simulation models: pure kerogen and kerogen previously saturated with hydrocarbon fluids. They show that the extent of swelling depends on the type of hydrocarbon as shown in Figure 1.5 below.

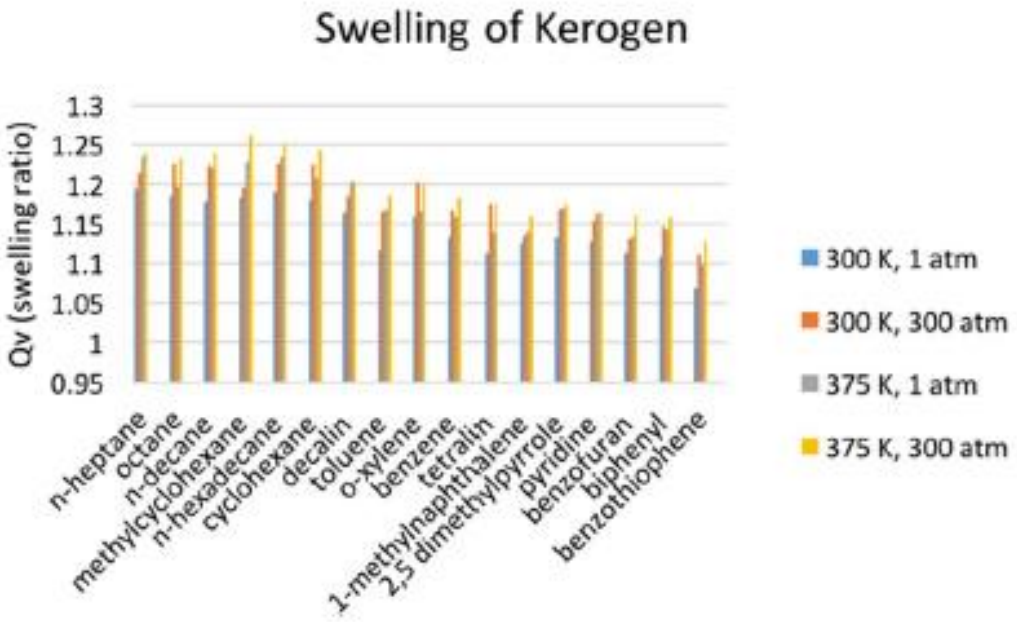

Figure 1.5. Swelling ratios of type II kerogen in presence of 17 hydrocarbon components under different temperature and pressure conditions (Pathak et al., 2017).

In another work, Bui et al (2018) generate organic pore models filled with hydrocarbon mixtures using different quenching rates to investigate the role of model building process on the resultant kerogen pore network (Figure 1.6a). They report that the kerogen models generated using a fast quenching process are associated with large pore sizes and more favorable to penetration of microemulsions as seen in Figure 1.6b.

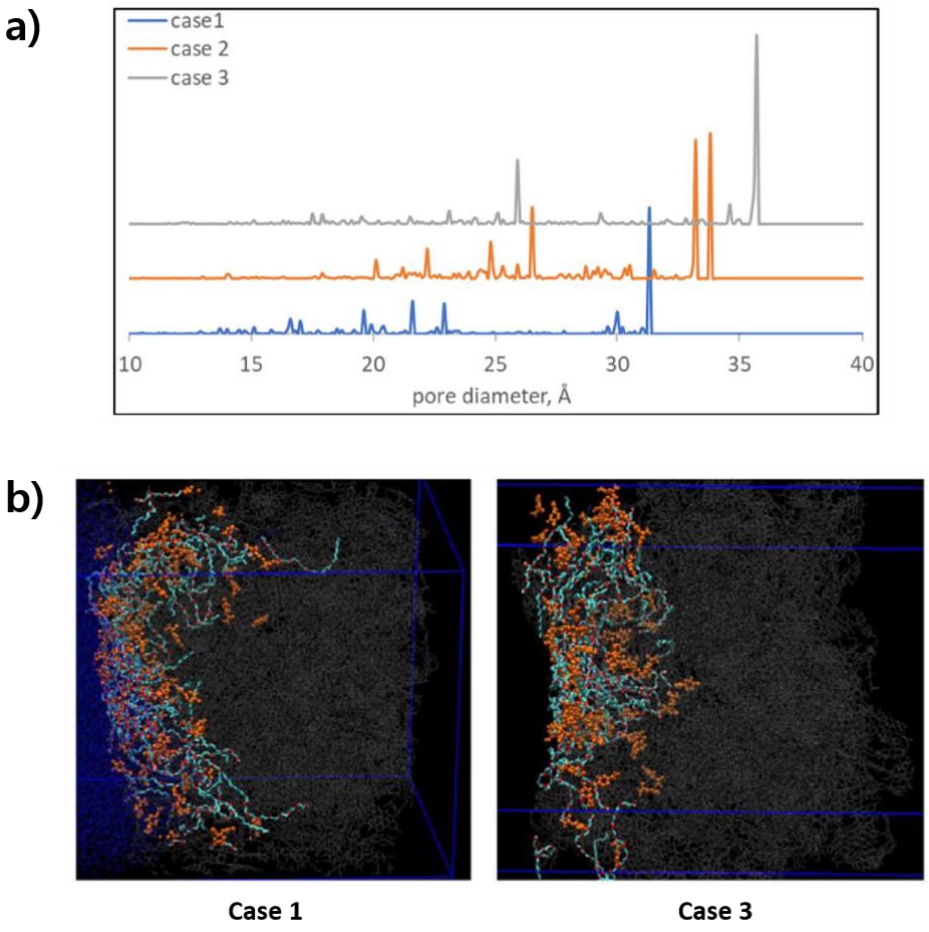

Figure 1.6. Effect of kerogen maturation on pore morphology and shale oil recovery. (a) shows pore size distribution of kerogen models with different cooling rate: case 1 (fast), case 2 (medium), and case 3 (low). (b) shows comparison of microemulsion penetration into different organic pore models (Bui et al., 2018).

Perez and Devegowda (2019) carry out MD simulations to explore the spatial distribution of reservoir fluids in kerogen corresponding to condensate/volatile oil window (Figure 1.7). They observe that the tendency for adsorption increases with increasing molecular weight. They also report that the partial or complete adsorption of heavier components in the organic pores causes pore blockage that inhibit hydrocarbon flow.

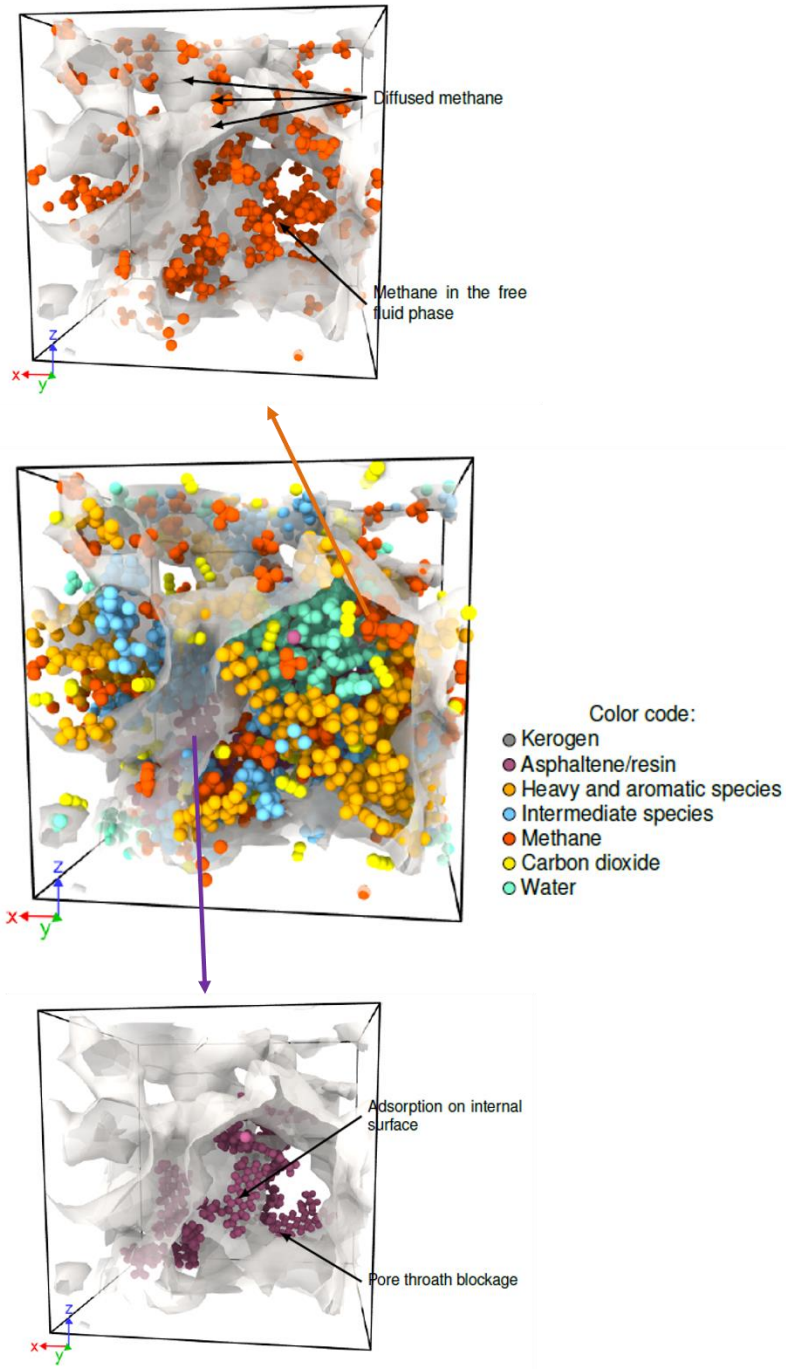

Figure 1.7. Spatial distribution of reservoir fluids within kerogen pores. The lighter components are shown to exist as a free fluid within the pore body while the heavy ends are mostly adsorbed onto kerogen surfaces. (Reprinted from Perez and Devegowda, 2019).

Although organic pores are considered to be the primary storage sites for hydrocarbons in shales, inorganic material constitutes a large percentage of the shale matrix and should be considered for fluid flow (Clementz, 1982; Borysenko et al., 2009; Curtis et al., 2011; Clarkson et al., 2013; Zhang et al., 2016; Zhao et al., 2019). Generally, clay minerals are thought to be hydrophilic (Ambrose et al., 2012; Fang et al., 2014).

In order to study the structural distribution of water, Wang et al. (2005) conduct MD simulations of water at constant temperature and volume on a two-layer muscovite slab surface. In their simulation work, the ordering of adsorbed water is shown to be restricted. A large percentage of water was shown to have a preferential orientation relative to the adsorption surface. This orientation is controlled by the presence of hydrogen bonding, surface charge distribution, and the existence of charge-balancing cations (K^+) on the clay surface. In a separate publication, Bourg and Steefel (2012) simulate water-filled silica nanopores using molecular dynamics to analyze the structure of water under confinement. Water-silica interaction in pore diameters ≥ 2 nm are shown to lead to multilayer adsorption and the remaining water forms a bulk-like liquid at the center of the pore. At smaller diameters, the structural properties of interfacial water are strongly influenced by the confinement effect. Additionally, Zhang et al. (2016) document molecular interactions between fluid mixtures (water/alkane/salts) and clay minerals at different wettability conditions (Figure 1.8).

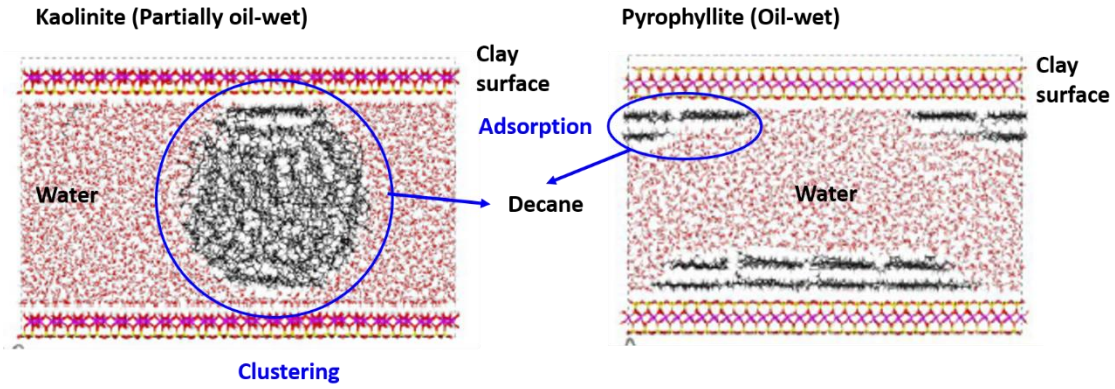

Figure 1.8. Water and hydrocarbon distribution in clay slit nanopores with different wettability conditions (Reprinted from Zhang et al., 2016). Kaolinite shows partially oil-wetting behavior with an affinity to decane and water. Pyrophyllite appears to possess fully hydrophobic surfaces with strong decane adsorption.

The results show that a difference of the surface groups alters the wettability of the basal surfaces from oil-wet to water-wet and completely water-wet. Thus, clay surfaces are seen to affect hydrocarbon adsorption as well as aggregation and transport under different wettability conditions. In a more recent work, Santos et al (2018) use molecular dynamics simulation to observe the storage of n-alkane/CO_2 mixtures confined in calcite slit nanopores (Figure 1.9). Their study shows that methane adsorbed on the calcite surface can be desorbed by the strong polar interaction between CO_2 and the clay surface. The degree of CO_2 adsorption was shown to be controlled by the number of calcium sites on the pore surface. Hao et al. (2018) also investigate adsorption behavior of methane in illite slit pore models with basal and edge surfaces using GCMC simulations. They show that the simulated adsorption capacity varies by location. In addition, Xiong et al. (2020a) construct two different illite slit nanopores, classified as hydroxyl-hydroxyl (H-H) and potassium-hydroxyl (P-H) clays, to study the behavior of water in clay nanopores

(Figure 1.10). Their study shows that the different surface with different charge distribution can result in different structures of water. The P-H surface was seen to be more favorable to generate a structure called a water bridge, in comparison to the H-H surface. Xiong et al. (2020b) additionally address the effect of salinity during hydrocarbon recovery and its impact on the water bridges.

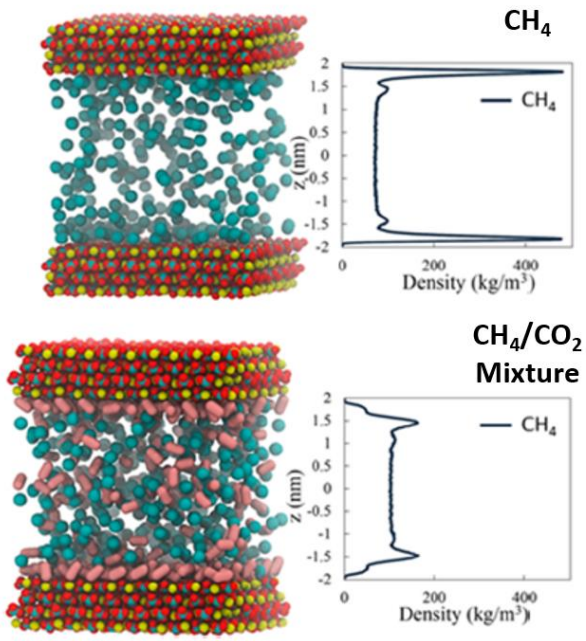

Figure 1.9. Mass density profile of pure methane and methane-carbon dioxide mixture in silica slit nanopores at 375K for pore width of 4 nm. CO_2 preferentially occupies silica surfaces, decreasing methane adsorption (Santos et al., 2018).

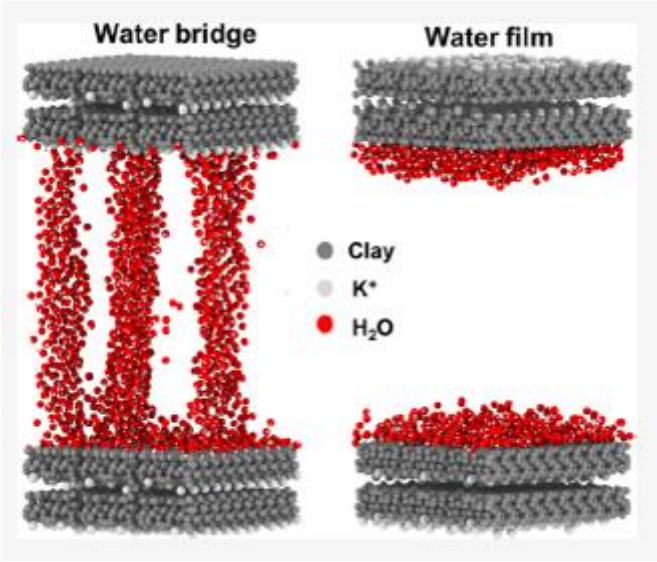

Figure 1.10. Formation of water bridges at potassium-hydroxyl surface (left) and water films at hydroxyl-hydroxyl surface (right) in 5nm illit nanopores under 350K and 400 atm (Xiong et al., 2020).

Because clay minerals with charged surfaces interact with fluid components, inorganic rock-fluid interaction can play a role in phase behavior and hydrocarbon storage. Shirono et al (2007) analyze possible phase states of water in silica nanopores at 300 K based on MD simulation runs. They indicate that pore diameter and hydration levels impact the structural and dynamical properties of water molecules leading to the formation of a distinct adsorbed layer (by fluid-mineral surface interaction), a condensed water layer (by water-water interaction) at the pore surface, and pore-filling or free water. Jin and Nasrabadi (2017) study the phase behavior of hydrocarbons in slit nanopores with different surface materials Their comparative analysis show that calcite, one of major inorganics in shale reservoirs, has a relatively higher adsorption effect than kerogen (Figure 1.11). The strong adsorption is shown to enhance the confinement effect on fluids and, consequently, a significant shift of the phase diagram was shown to occur in calcite nanopores.

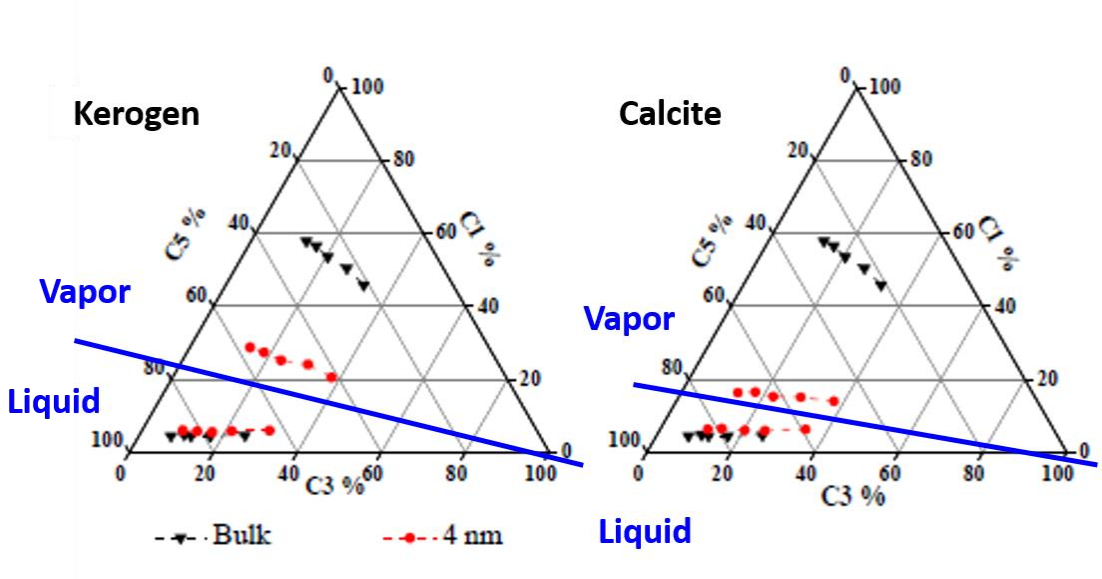

Figure 1.11. Ternary diagram of multicomponent fluid confined in pores of different surfaces. Black triangle denotes phase diagram of bulk fluid and red circle refers to the fluid confined in 4 nm pores (Reprinted from Jin and Nasrabadi, 2017).

As mentioned before, previous studies have usually addressed fluid transport in organic and inorganic matters separately, but do not provide a comprehensive understanding of fluid behavior in pores of mixed wettability. A few MD simulation works, related to mixed-wet systems, compute mechanical properties of clay-organic nanocomposites, phase behavior and multiscale fluid flow in organic/inorganic nanopores. Sedghi et al. (2014) investigate oil and water displacement inside nanoscale water-wet to oil-wet pores using non-equilibrium molecular dynamics (NEMD) simulations. They show that drainage simulation in the mixed wet pores reconfigures pore fluid distribution and surface wettability. The simulation results are in a good agreement with the computation by the Mayer-Stowe-Princen (MS-P) theory to calculate capillary pressure for two-phase displacement. Hantel et al. (2017) discuss reactive molecular simulations of mechanical reinforcement of a series of clay-organic nanocomposite systems with different interfacial cohesiveness. The mechanical behavior in the resulting nanocomposite systems is shown to be

highly associated with interface heterogeneity and interface bonding. Katti et al (2017) also study organic-inorganic interaction at atomistic scale. They initially place kerogen and heavy hydrocarbons within clay slit pores and carry out simulations at constant temperature conditions. Their final configuration indicates that heavier hydrocarbons are more attracted to clay surfaces. Yu et al. (2019) use a pore network model (PNM) with a complex nanoporous structure and significant heterogeneity to describe gas transport behavior in the shale matrix. They report that fluid-rock interactions and the proportion of organic pores influences gas permeation in the shale matrix. In a more recent work, Faisal et al (2020) model the interaction of type I kerogen with calcite surfaces to describe molecular binding of these surfaces.

These studies provide a better understanding of fluid transport and matrix structure when organic and inorganic components are present. However, they lack consideration of multicomponent hydrocarbons in mixed-wet shale pores, and even the treatment of water-hydrocarbon mixtures is lacking both at high and low salinity conditions.

In this study, I investigate the spatial fluid distribution based on fluid-fluid and solid-fluid molecular interactions from MD simulation runs in mixed-wet pores. The thesis is organized as follows: Chapter 2 describes how molecular interactions affect fluid distribution in mixed-wet nanopores. Chapter 3 explains the relationship between hydrated complexes and hydrocarbon distribution through the examination of number density profile. Finally, Chapter 4 highlights the combined effect of salinity and surface chemistry to hydrocarbon distribution in mixed-wet shale nanopores. Chapter 5 summarizes the conclusions and presents opportunities for future work.

CHAPTER 2. FLUID-FLUID AND SOLID-FLUID MOLECULAR INTERACTIONS IN MIXED-WET PORES

2.1 Introduction

This chapter describes the spatial distribution of water and hydrocarbon components when confined in mixed-wet pores based on fluid-fluid and solid-fluid molecular interactions. I first describe the construction of the model, specifically the molecular models of kerogen, the volatile oil used in this study, and the clay surfaces. As mentioned in the previous chapter, organic-rich shale reservoirs exhibit a complex mineralogy and an abundance of organic matter which can affect hydrocarbon flow and storage (Curtis et al., 2010; Sondergeld et al., 2010; Wei and Qin, 2013). X-ray microtomography, SEM imaging, atomic force microscopy (AFM) enable exploration of the microstructural features of nanoporous shale rocks (Kovscek et al., 1993; Yu et al., 2003; Kim et al., 2009; Hassenkam et al., 2009; Pak et al., 2015) yet are unable to delineate flow and storage mechanisms at the nano- and micro-scale (Bogue, 2011; Doudrick et al., 2014; Lu et al., 2019).

Molecular dynamics (MD), on the other hand, can assist in examining the configuration of oil and water in nanopores, especially when these cannot be examined by experimental means (Ungerer et al., 2006; Palmer and Debenedetti, 2014). Molecular dynamics is a deterministic computational method that captures the physical movements of particles representing atoms and molecules at the nano- and micro-scale. The particles included in the MD simulation models interact with each other, and the physical and thermodynamic properties obtained from their interactions are dictated by a designated force potential. The trajectory of all the particles is determined based on a numerical integration of Newton's second law simultaneously for all particles over time. MD simulation runs are time-consuming, taking a few hours to several weeks of computation time based on the complexity of the system to be modeled. As described in Chapter

1, MD simulations have seen increased applications in the oil and gas industry because of their ability to predict hydrocarbon behavior under nanoporous confinement. In the next section, I will describe the mixed-wet pore models used in this study.

2.2 Modeling of Mixed-Wet Shale Nanopores

The software package used for this study is the Large-scale atomic/molecular massively parallel simulation (LAMMPS) (Plimpton, 1995). The organic matter is constructed using kerogen monomers initially developed by Ungerer et al. (2015). For the inorganic material, there are several choices including clay minerals, quartz and calcite. The clay minerals include illite, montmorillonite, kaolinite, and muscovite. In this study, I use a molecular model of illite to represent inorganic surfaces because illite is the most prevalent clay mineral in shale rocks (Gualtieri et al., 2008; Galán and Ferrell, 2013; Ho and Wang, 2019). A detailed discussion of the organic and inorganic models is provided in the following subsections.

2.2.1 Clay Minerals

Illite has a layered structure in which a tetrahedral gibbsite sheet is sandwiched between two octahedral silicate sheets (Gaudette et al., 1966; Galán and Ferrell, 2013). The octahedral sheets occasionally include ionic substitution where Si^{4+} is replaced by Al^{3+}, or Al^{3+} is replaced by Mg^{2+}. The models in this study have Si^{4+} substituted octahedral sheets. The illite sheet is originally negatively charged but is neutralized by an appropriate number of potassium cations. Hence, the final formula of our clay models is defined as $K[Si_7Al]$ (Al_4) $O_{20}(OH)$. The size of the illite unit cell is 1.04 nm × 0.89 nm × 1.00 nm and in total, 45 unit cells are used to create the inorganic surface materials using Material Studio (Accelrys, 2016). The clay basal structure is of two types: hydroxyl-potassium (H-P) and potassium-potassium (P-P) surfaces, as shown in Figure 2.1, that model two different surface charge configurations.

It is important to note that the H-P structure has a negatively charged hydroxyl surface and an opposing positively charged potassium surface. The P-P clay structure has two opposing positively charged potassium surfaces. These are two end members of various intermediate possibilities of surface charge distributions. Given that clays are exposed to formation brines for extended periods of time, it is likely that the opposing surfaces have balanced charges. However, I also consider the highly imbalanced H-P structure to understand fluid behavior under those extremes.

In addition, I adopt the bond valence method to achieve charge balance of the inorganic materials by adjusting the charge of the edge oxygen (Gaudette et al., 1966; Gualtieri et al., 2008; Hao et al. 2018). The interatomic potentials of the illite model are computed using the CLAYFF force field (Cygan et al., 2004). I make the choice of CLAYFF because it is appropriate for simulating clay minerals and their interfacial reaction with aqueous solutions (Cygan et al., 2004; Cygan et al., 2012; Jin et al., 2017).

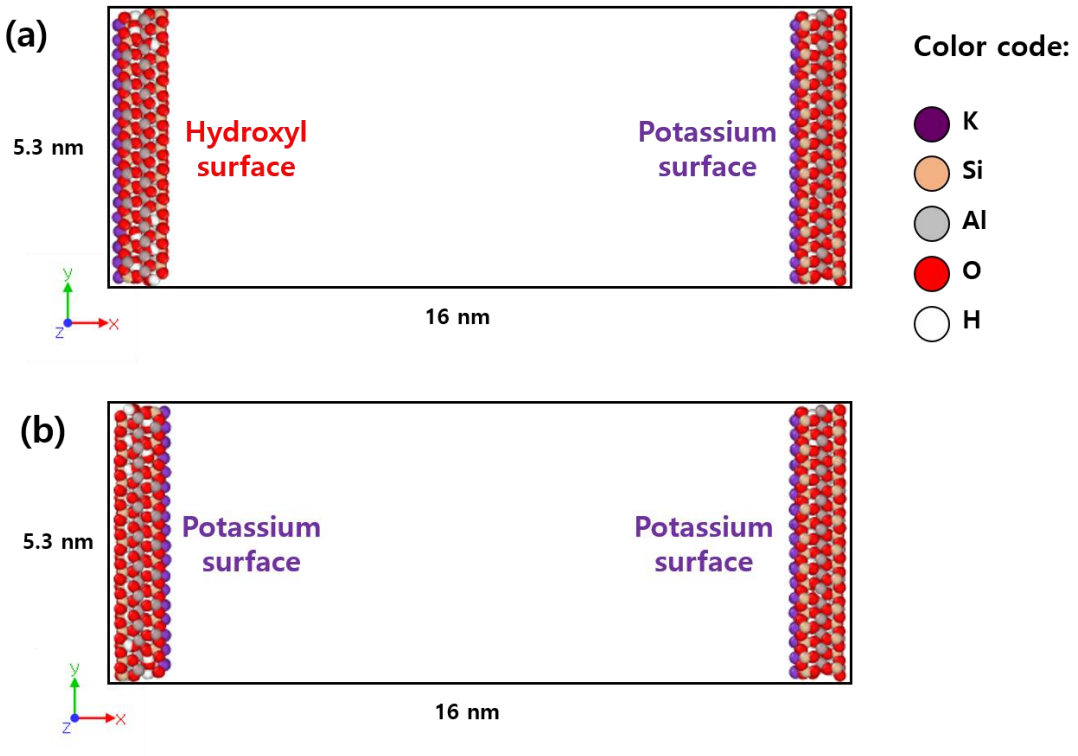

Figure 2.1. Molecular structure of (a) hydroxyl-potassium (P-H) and (b) potassium-potassium (P-P) illite surfaces. The potassium surface is positively charged while the hydroxyl surface is negatively charged.

2.2.2 Organic Matter and Fluid Components

The organic models used in this work rely on the use of the kerogen monomers with chemical formula, $C_{242}H_{219}O_{13}N_5S_2$ initially developed by Ungerer et al. (2015). For this study, I use the type II-C kerogen monomers to create the organic system belonging to the oil/gas-condensate window as shown in Figure 2.2. The construction of the kerogen models derives from the works of Yiannourakou et al (2013), Collell et al (2014b) and Ungerer et al. (2015) and matches the experimental data published by Kelemen et al (2007). They suggest that the structural characteristics of kerogen can be reproduced when at least 1,300 atoms form the models.

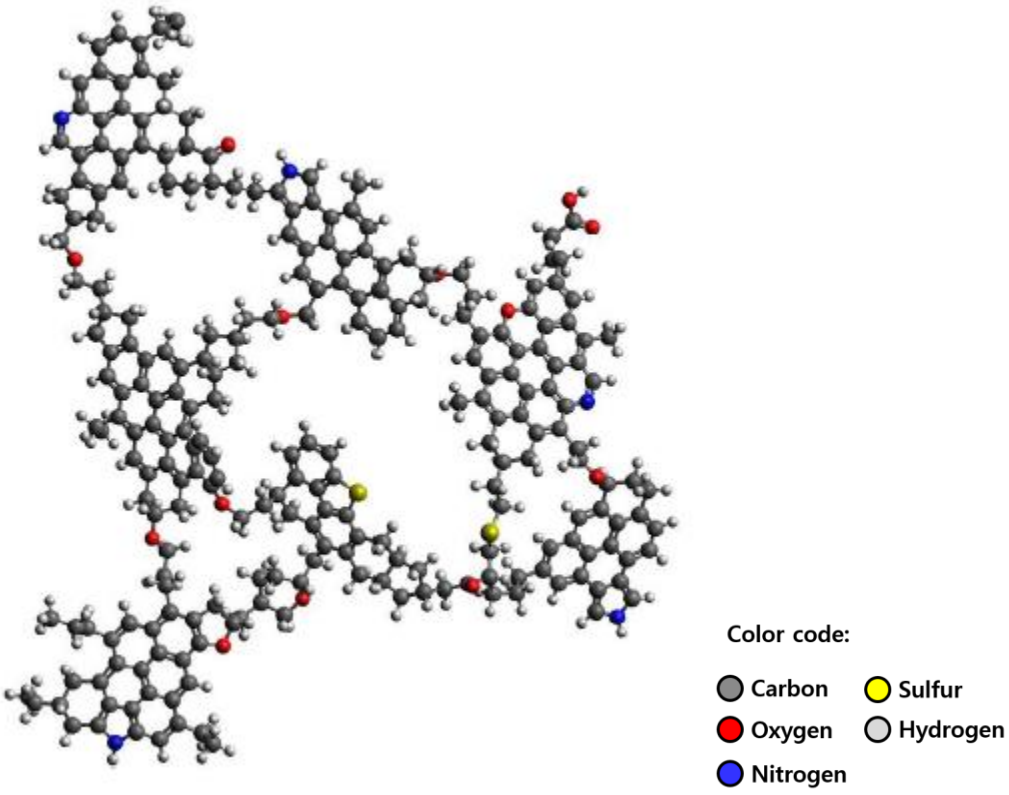

Figure 2.2. Type II-C kerogen monomer ($C_{242}H_{219}O_{13}N_5S_2$) (Ungerer et al., 2015).

I adopt the kerogen models described in Perez and Devegowda (2019) that uses 16 kerogen monomers with 7,696 atoms in total. The description of the annealing process with the fluid model is provided in the next section. Figure 2.3 shows the number of molecules for each species constituting the volatile oil and the organic kerogen. The composition of the volatile oil is shown separately in Table 2.1. The volatile oil composition is obtained from Ungerer et al. (2015) who lumped the gas condensate model created by Lagache et al. (2004).

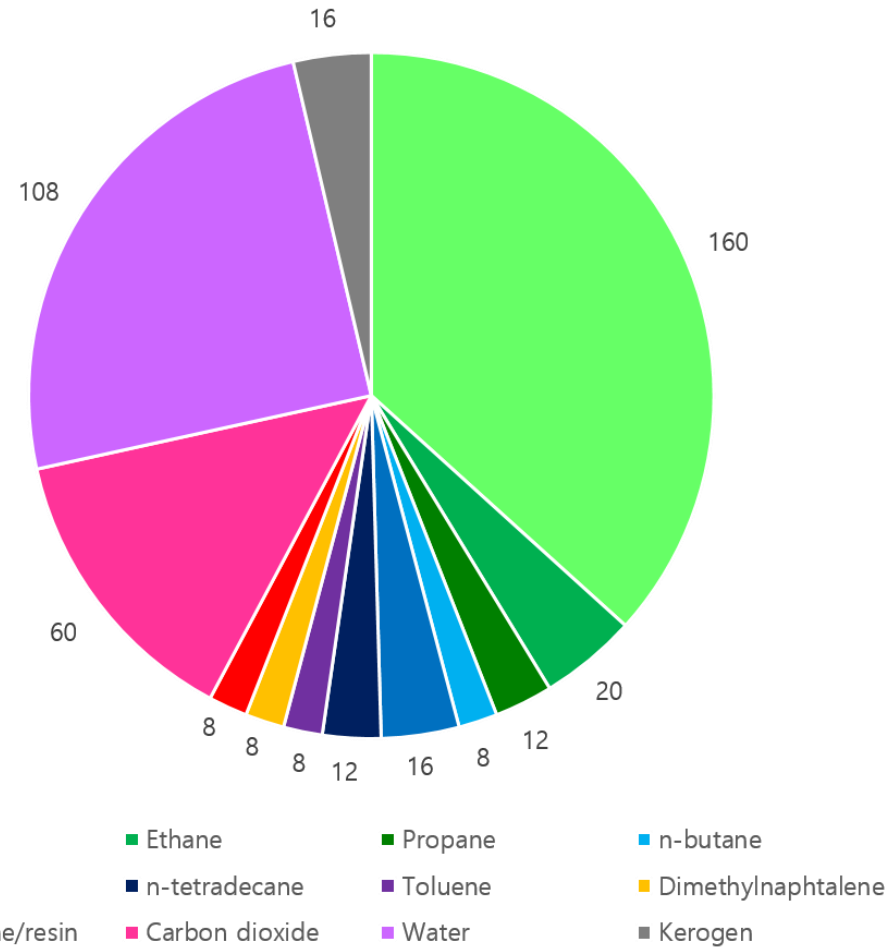

Figure 2.3. Pie chart showing the number of molecules constituting the organic kerogen and the volatile oil used in this study.

Table 2.1. The molar fraction of volatile oil.

Species	Mole fraction, %
Methane	63.5
Ethane	7.9
Propane	4.8
n-butane	3.2
n-octane	6.3
n-tetradecane	4.8
Toluene	3.2
Dimethylnaphtalene	3.2
Asphaltene/resin	3.2

A single generic molecule is used to model both the asphaltene and resin fraction (Figure 2.4) with associated polar substituents. The chemical formula is given by $C_{26}OH_{32}$. Collell et al. (2014a) show that the generic molecular formula for the asphaltene/resin fraction is a good match with the heavy products formed during maturation process. The number of water and carbon dioxide molecules is adjusted based on recommendations by Tissot and Welte (1984) who consider an atomistic balance of kerogen during thermal maturation. Water behavior is modeled using the SPC model introduced by Berendsen et al (1981).

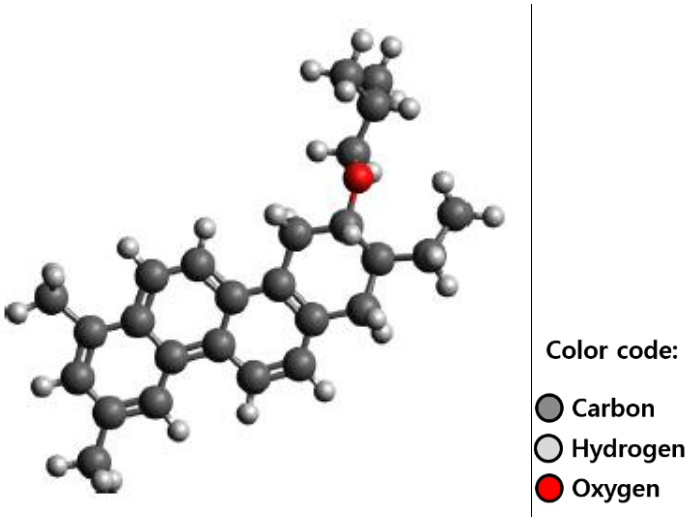

Figure 2.4. Molecular model of single generic asphaltene/resin with chemical formula $C_{26}OH_{32}$ (Collell et al., 2014a).

2.2.3 Details of the Simulation Models

The simulation procedure begins with a slow annealing process of the kerogen macromolecules and the volatile oil (Perez and Devegowda 2019). PACKMOL (Martínez et al. 2009) is used to randomly distribute all the molecular species in a 10.0 nm × 10.0 nm × 10.0 nm cubic simulation box. The models have periodic boundary conditions (PBC) in all directions. The Lennard-Jones and electrostatic forces for non-bonded interactions have a cutoff distance of 15 Å. Long distance corrections are applied to the Lennard-Jones energy beyond the cutoff, and the particle-particle particle-mesh method is used to describe the electrostatic force (Hockney and Eastwood, 1988; Sun, 1998). Molecular interactions of the kerogen monomers are calculated by the consistent-valence force field (CVFF), and optimized potential for liquid simulations (OPLS) is used to capture hydrocarbon behavior (Dauber-Osguthorpe et al., 1988; Jorgensen et al., 1996).

In the slow quenching process, all the species in the simulation box are reconfigured based on the Polak-Ribiere version of the conjugate gradient (CG) algorithm (Hestenes and Stiefel, 1952).

Quenching the organic species with fluid molecules is performed using an NVT ensemble with a Nosé–Hoover thermostat up to 1000K followed by an NPT ensemble at a pressure of 400 atm through the Parrinello-Rahman barostat (Parrinello and Rahman, 1981; Nosé, 1984a; Nosé, 1984b; Nosé, 1991). Temperature is then decreased by 100K while pressure is maintained at the same value. For each stage, the simulation is run for 500 ps with a time step is 1 fs. Finally, temperature and pressure conditions are lowered to 355K and 300 atm to achieve target reservoir conditions.

The equilibrated organic matter has a density of 1.40 ± 0.01 g/cm3, which agrees with the experimental values of 1.4 – 1.6 g/cc reported by Dang et al. (2016). I eliminate the periodic boundary condition of the kerogen models in the x-direction by extending the configuration of the simulation system. All the atoms crossing the x-boundary in the organic pore models are translocated manually to create flexible kerogen surfaces. I finally create a mixed-wet pore model by placing two illite sheets on either side of the kerogen model and the simulation box size is extended along the x-direction as shown in Figure 2.5a. The mixed-wet pores are approximately 55 nm in width at the initial state and after equilibration, the size of the pore spaces is changed to 4 nm roughly. The measurement is approximate because of the irregular structure of the kerogen surface. I then populate the void spaces on either side of the kerogen model with different fluids. The mixtures considered in this study are 80:20, 60:40, 40:60, and 20:80 volatile oil/water ratios.

A large percentage of the water molecules are placed in the void spaces, but a few are also initially placed within kerogen. The models in this work are of two types: one with water within kerogen and the other with all the water initially outside of the kerogen matrix. The water molecules within kerogen originate from the atomistic balance described earlier (Tissot and Welte, 2014). There have been a few reports of water residing in organic pores both from an experimental point of view (Chalmers and Bustin, R.M., 2007) and from a modeling viewpoint (Hu et al., 2014;

Jagadisan and Heidari, 2019). For the models with all the water residing outside of kerogen, water is replaced with carbon dioxide.

The randomly distributed fluid in the mixed-wet simulation box are packed by applying gravity forces on the two rigid illite sheets for 1,000 ps of an NVT simulation. During the procedure, all atoms of the kerogen models are kept fixed and the models go through an energy minimization step to adjust the configuration of the atoms again. After the model is packed to roughly 4-5 nm along the long pore axis (i.e., x-axis) as shown in Figure 2.5b, the NPT simulation at our target condition (355K and 300 atm) is carried out for 8 ns.

Sulfur molecules in the kerogen monomers are frozen to retain flexibility of the organic materials without impacting their macroscopic properties. Maintaining the structural characteristics allowed us to capture adsorption and swelling of the kerogen into our models (Ho et al., 2018; Obliger et al., 2018; Tesson and Firoozabadi, 2018; Wu and Firoozabadi, 2019). In the meantime, the illite structure is kept fixed except for K^+ and the H^+ ion associated with the clay surfaces. The Lorentz−Berthelot mixing rule is used to simulate the surface materials-fluid interaction as given in Eqs. 1 and 2 (Lorentz, 1881). In these equations, ε is the depth of the potential well, and σ is the finite distance at which the inter-particle potential is zero.

$$\sigma_{ij} = \frac{\sigma_{ii}+\sigma_{jj}}{2} \quad (1)$$

$$\varepsilon_{ij} = \sqrt{\varepsilon_{ii}\varepsilon_{jj}} \quad (2)$$

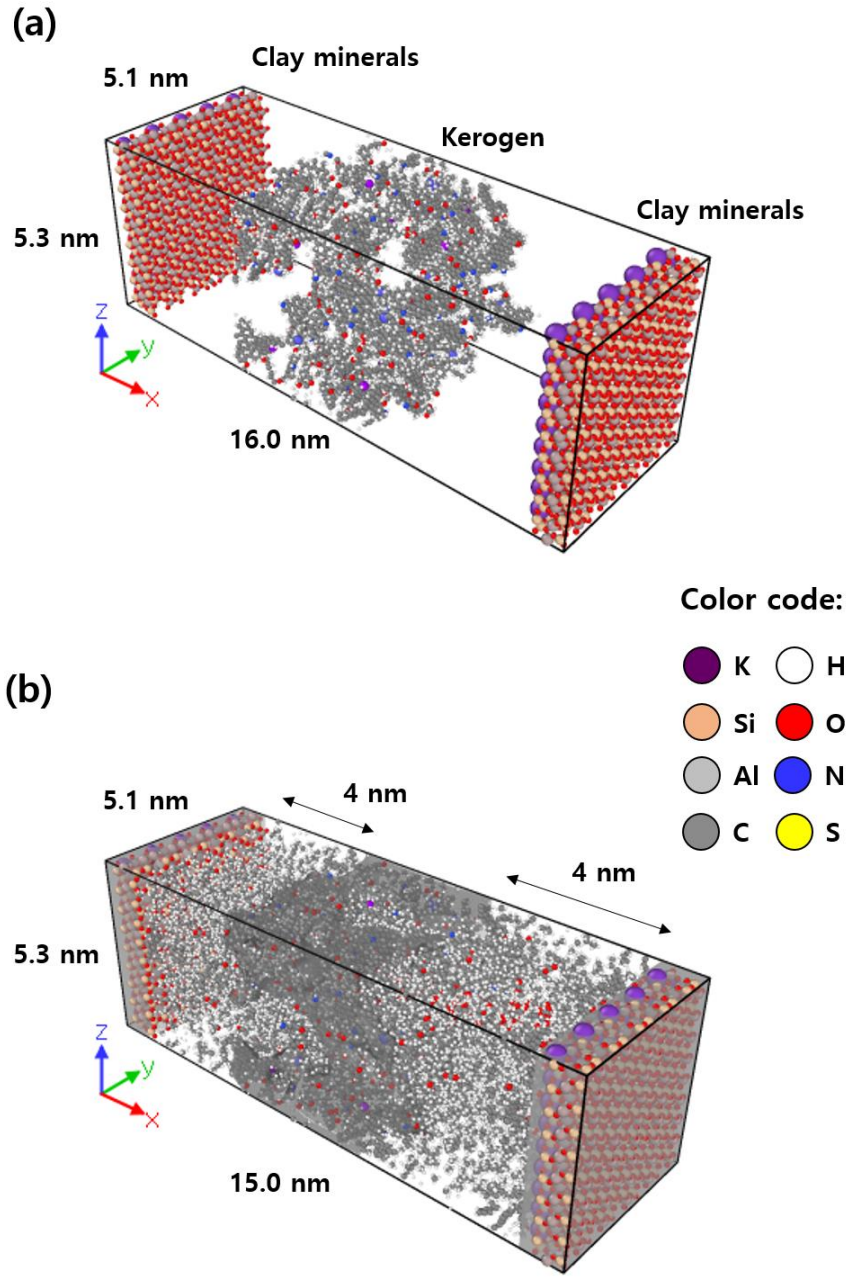

Figure 2.5. Snapshots showing (a) a mixed-wet pore structure and (b) the fluid-saturated mixed-wet pore after equilibration.

2.3 Molecular Interactions in Mixed-Wet Nanopores

In this section, I describe the fluid-pore surface and fluid-fluid interactions for all combinations of hydrocarbon species and water. The non-bonded molecular interactions are computed based on Eq. 3 (Jones, 1924; Cornell et al., 1995). The first term denotes van der Waals interaction, obtained by standard 12/6 Lennard-Jones potential, and the second term expresses electrostatic interaction based on Coulomb's law. In the equation, C is an energy conversion constant, r is the distance between two interacting particles, and q is charge of an atom, respectively.

$$E = 4\epsilon\left[\left(\frac{\sigma}{r}\right)^{12} - \left(\frac{\sigma}{r}\right)^{6}\right] + \frac{Cq_iq_j}{\epsilon r}, r < r_c \quad (3)$$

The potential energy is quantified as the sum of the Van der Waals (first term in the Eq. 3) and the electrostatic (second term in the Eq. 3) interactions. A positive sign indicates a repulsive interaction, and a negative sign denotes an attractive interaction. In order to analyze the molecular interactions, I compute interactions for every pair of fluid species and surface type in the sample. For instance, with 11 hydrocarbon species, there are a total of 11 pairs for computation of kerogen-hydrocarbon interactions. These non-bonded interactions are averaged for 2 ns over several 100 fs time steps, after model equilibration, to compute the interaction values for all the species in the models.

In this section, I computed the interactions between all fluid molecules and pore surfaces for the mixed-wet system with an H-P clay surface. I computed the molecular interactions at varying water concentration and confirmed that the degree of the interaction energy was proportional to the molar fraction for each fluid species. But the dependence could not provide an objective

interpretation about the molecular interactions I would like to investigate in the mixed-wet pores. Thus, I constructed a model includes the same number of all the fluid species to exclude the effect of concentration. The interactions are quantified in terms of the potential energy (kcal/mol) associated with the different forces. For instance, the fluid interactions with the clay surface are independently calculated for each species. The simulation box is populated with a 104 of a chosen fluid molecule and then I run a pseudo-simulation of 1ns to compute the interactions. During the computation, I alternatively turned on and off the van der Waals and Coulombic interactions to assess each force separately.

The interaction between the kerogen monomers and the fluid molecules shows the predominance of the van der Waals forces for all of the hydrocarbon species as shown in Figure 2.6. Heavy components, such as octane, tetradecane, dimethylnaphtalene, and asphaltene/resin, have approximately 350% higher attraction compared to light and intermediate components. The higher adsorption reported for heavy hydrocarbons is because of the stronger van der Waals' forces (Wang et al., 2015a; Wang et al., 2015b; Hao et al., 2018; Perez and Devegowda, 2019).

Water is the only species in which the electrostatic force is higher than the Van der Waals force. There is a small but non-negligible electrostatic interaction between the asphaltene/resin fraction and kerogen due to the attraction between the carbonyl group in the resin and electronegative atoms in the kerogen monomers (Mitchell and Speight, 1973; Wu et al., 2016).

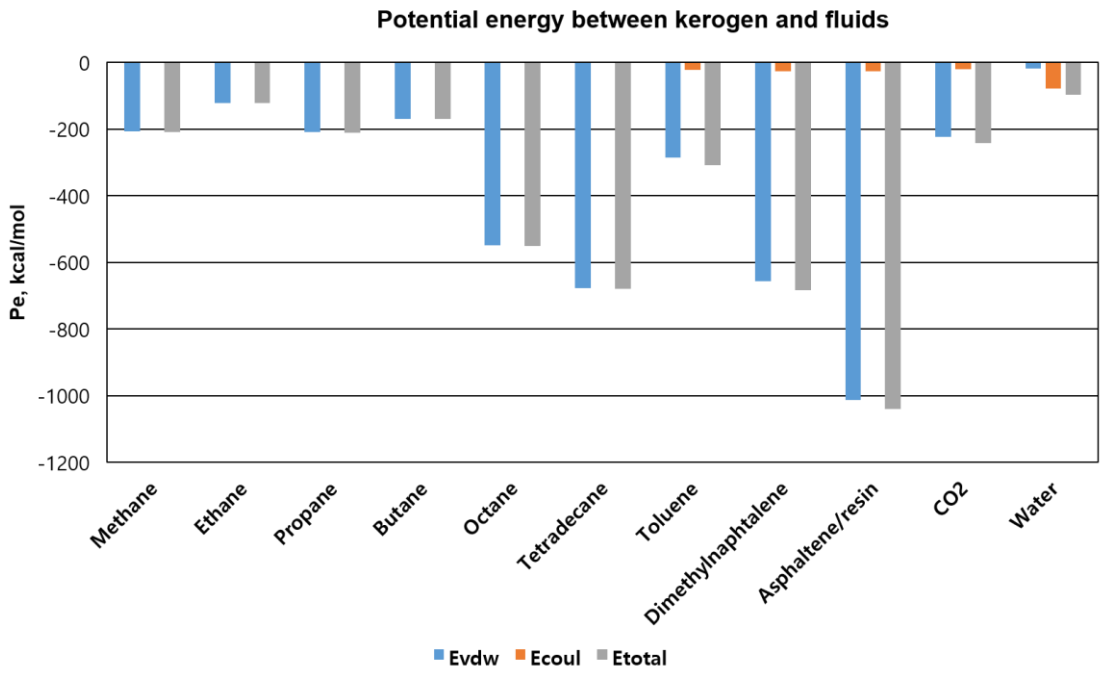

Figure 2.6. Van der Waals and Coulombic interactions between kerogen and fluid components in the simulation box with H-P clay surfaces.

Figure 2.7 presents the final configuration of asphaltene/resin molecules around kerogen surfaces. As observed in Figure 2.6, the significant van der Waals forces between the asphaltene/resin fraction and kerogen induces adsorption of the heavy compounds onto the kerogen surfaces, around the pore throats as well as on pore body. The adsorption of asphaltene/resin molecules has been shown to inhibit flow of relatively mobile hydrocarbons by pore throat blocking and restricts access of solvents to additional pore volumes (Perez and Devegowda, 2019).

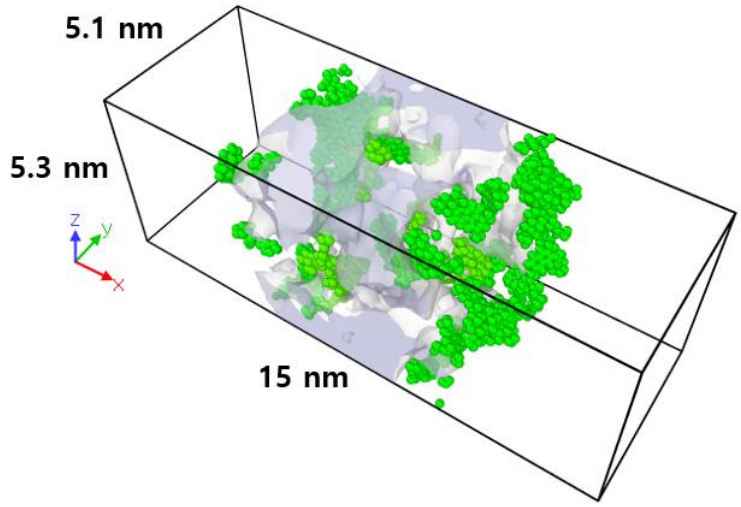

(a) H-P clay surfaces.

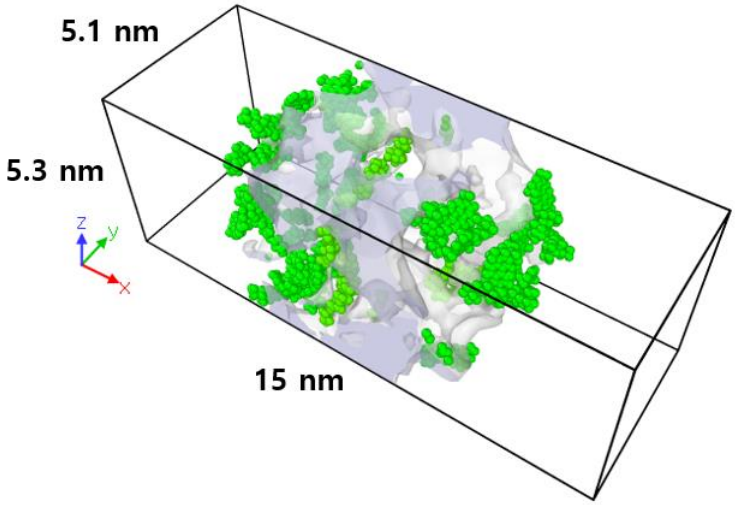

(b) P-P clay surfaces.

Figure 2.7. Spatial distribution of asphaltene/resin molecules around organic pore surfaces at 40% water concentration showing adsorption of the heavier hydrocarbon molecules on kerogen. Green color denotes asphaltene/resin molecules and transparent gray represents the kerogen surfaces. Clay is not shown for clarity.

Figure 2.8 presents the interaction energy of illite with the fluid molecules. Of all the hydrocarbon components, the heavy ends such as dimethylnaphtalene, and the asphaltene/resin fraction show relatively stronger non-bonded interactions with illite compared to the other hydrocarbon species. The light and intermediate hydrocarbons rarely interact with the illite surfaces. Toluene and dimethylnaphtalene exhibit higher electrostatic interactions with illite because methyl groups can be electrostatically attracted to sites containing electronegative atoms such as oxygen (Yaseen and Mansoori, 2018). Additionally, resins have more polar constituents than the aromatic groups leading to electrostatic interactions between oxygen atoms in asphaltenes and aluminum, or silicon, in illite surfaces.

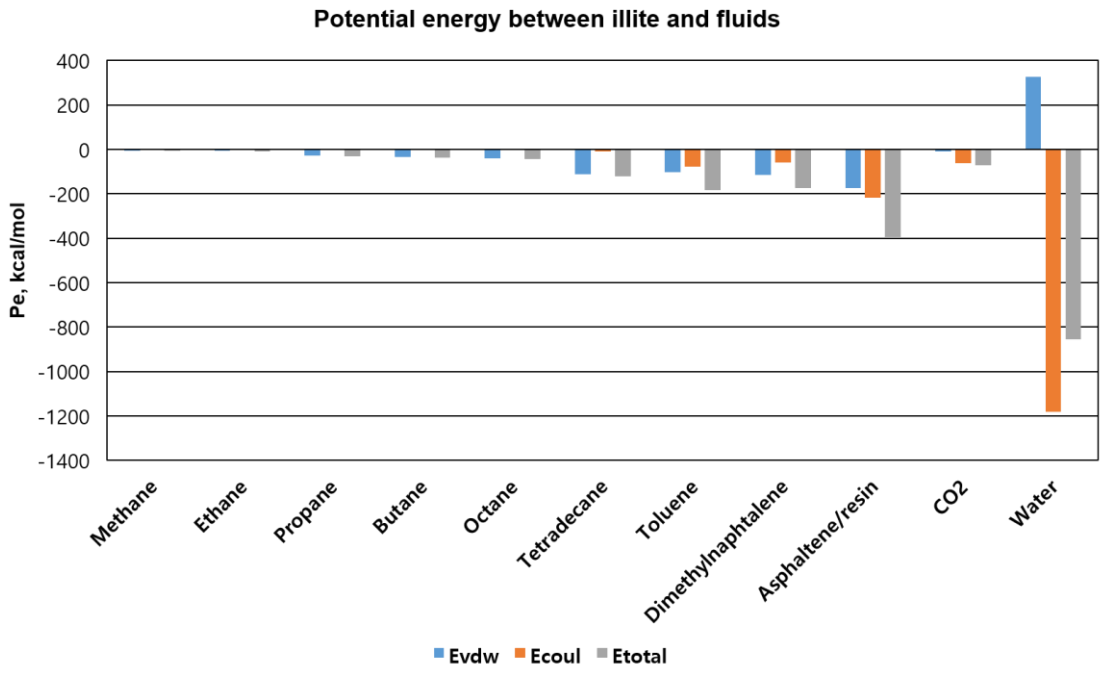

Figure 2.8. Van der Waals and Coulombic interactions between illite and fluid components in the simulation box with H-P clay surfaces.

These electrostatic interactions promote adsorption of a limited number of asphaltene/resin molecules onto the clay surfaces (Figure 2.9). This happens even in the presence of water. We also see some affinity between the asphaltene molecules and water on the clay surface on the left. Yaseen and Mansoori (2017 and 2018) also report that electronegative heteroatoms of asphaltene molecules contribute to the formation of the water-asphaltene hydrogen bonding by strong electrostatic attractions. In this work, I observe asphaltene/resin molecules adjacent to the illite surfaces (see the clay surface on the right in Figure 2.9), which reduces hydrophilicity of the clay minerals. In general, clays are considered to be hydrophilic. The results in this thesis show that, with a significant asphaltene fraction in the oil phase, the wettability of the clay surface can be altered to become more oil-wetting.

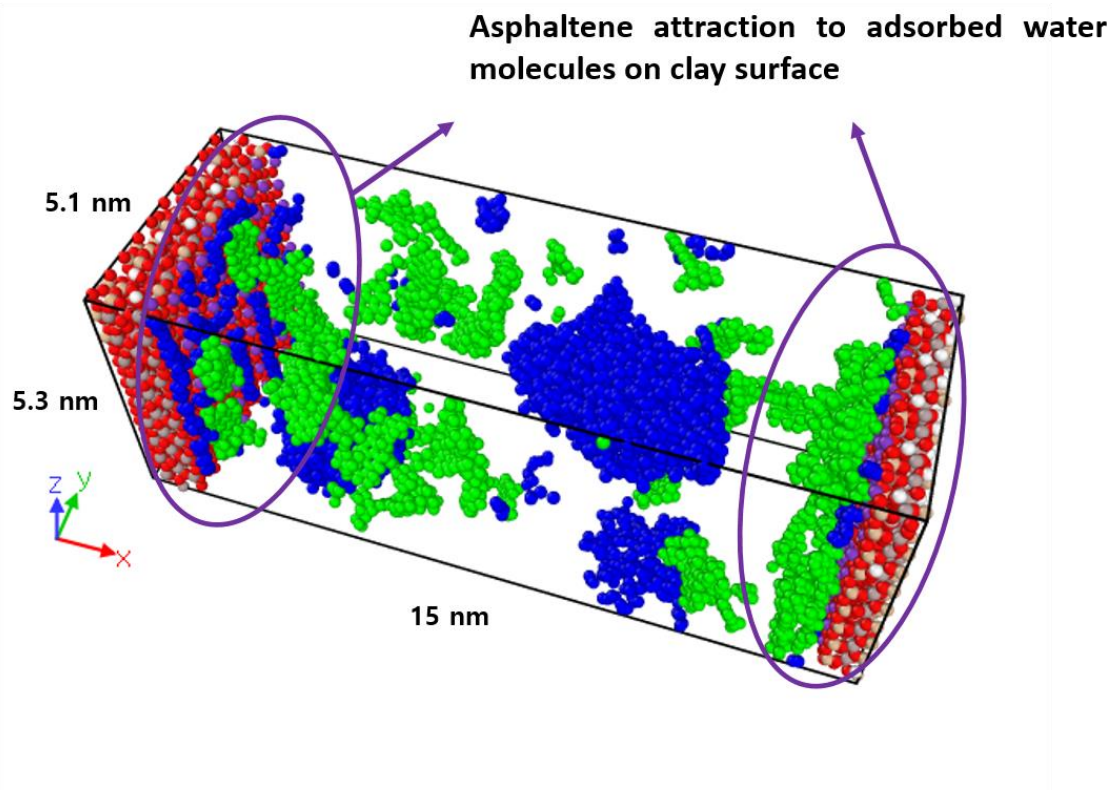

Figure 2.9. Spatial distribution of asphaltene/resin and water molecules at 40% of water concentration in the simulation box with P-P clay surfaces. Green color denotes asphaltene/resin molecules, blue color for water molecules, and other colors express atoms included in illite. Kerogen is not shown for clarity.

In terms of the interactions between water and the clay surfaces, water molecules show a positive van der Waals interaction due to repulsion between oxygen in water and the plane of oxygen in the illite sheet (Figure 2.8). Nevertheless, the hydrogen bonds (HBs) between hydrogen in water and the oxygen plane result in a robust attraction overwhelming the repulsive force. Figure 2.10 shows the spatial distribution of adsorbed water molecules on the P-P clay surface. The water molecules are mostly adsorbed onto the clay surfaces, except for a small number of water molecules forming water droplets. The strong water adsorption on clay surfaces is due to higher hydrophilic affinity of the water molecules by hydrogen bonding (Tunega et al., 2004; Zhang et al., 2015). For this hydrophilic interaction, the siloxane surface (Si−O−Si) accepts the charge of hydrogen in water while the hydroxylated surface (O−H group) accepts the charge of hydrogen and shares the charge of oxygen without water (Zhang et al., 2015; Joonaki et al., 2019; Xiong et al., 2020a).

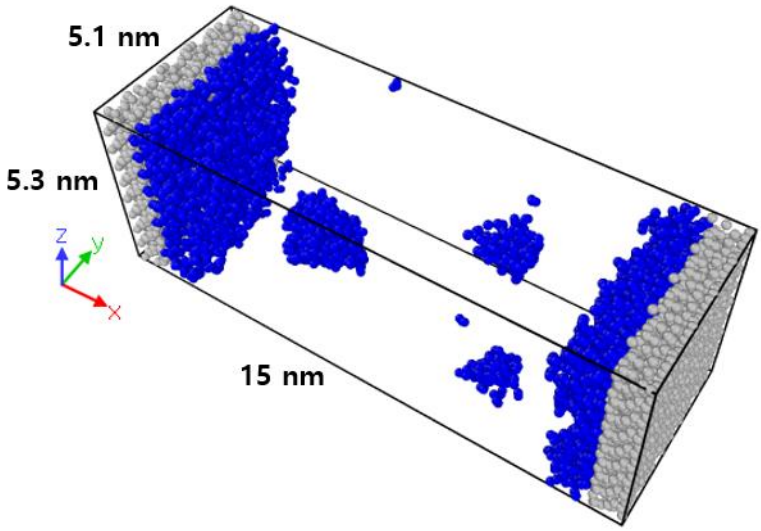

Figure 2.10. Spatial distribution of water droplets and adsorbed water layers at 60% of water concentration in the simulation box with P-P clay surfaces. The blue color denotes water molecules and the other colors express atoms included in illite. Kerogen is not shown for clarity.

In addition, I examine the molecular interactions of heavy components such as tetradecane, dimethylnaphtalene, and asphaltene/resin fraction with several other fluid molecules (Figure 2.11). In the results, the toluene and dimethylnaphtalene, including methyl groups, shows low electrostatic interaction with the three heavy ends. Yaseen and Mansoori (2017) show that the methyl group associated with dimethylnapthalene has a slight positive charge and the Coulombic interactions between different dimethylnapthalene molecules shows a repulsive like-like interaction.

The interaction of the asphaltene/resin fraction with light and intermediate components (methane and ethane) allows the heavy component to become soluble in the presence of such solvents (Mitchell and Speight, 1973; Tissot and Welte, 1984). However, the strong attractions with other asphaltene/resin molecules can also accelerate asphaltene aggregation, which is a significant challenge for the oil and gas industry, especially in the tubulars and fittings leading from the well to other facilities (Yang and Guo, 1997; Rae et al., 2001; Haji-Akbari et al., 2014).

Joonaki (2019) observed asphaltene with polar functional groups is adjacent to either adsorbed water on the clay surface or the charged clay surface. In addition, Yaseen and Mansoori (2017) described that some of water molecules solubilized in oil phase led to the asphaltene aggregation. The asphaltene precipitation can cause formation damage and reduce well deliverability by blocking pore throats (Wang and Civan, 2005; Shedid and Zekri, A.Y., 2006; Sedghi and Goual, 2016). While this study does not focus on improved oil recovery and asphaltene aggregation, these are some possible insights provided by molecular dynamics simulations.

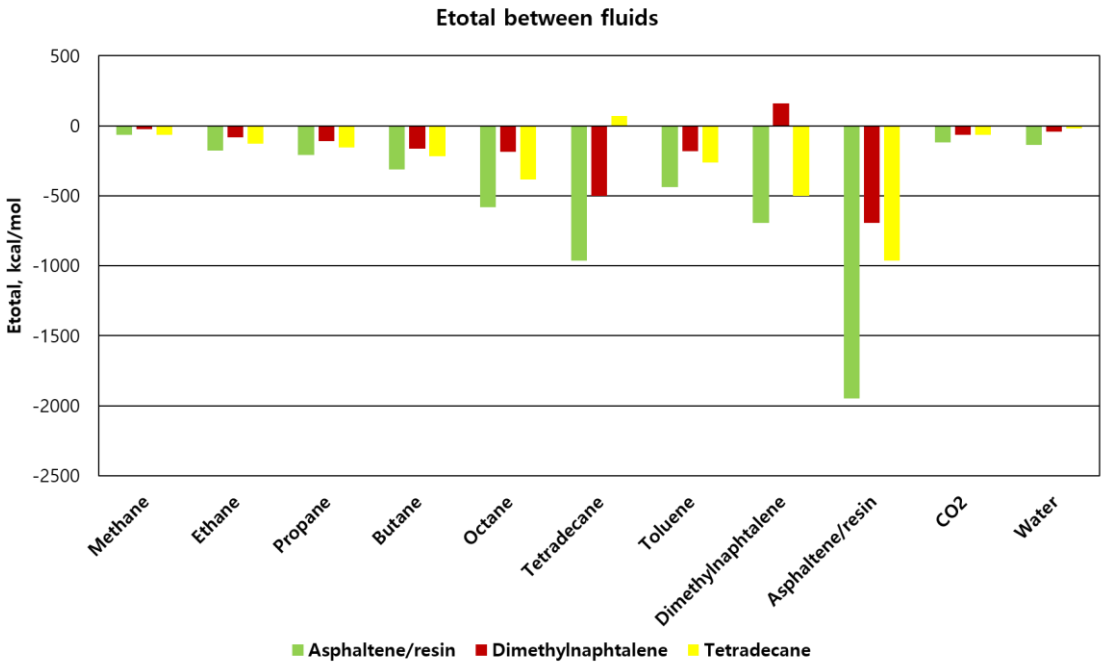

Figure 2.11. Fluid-fluid interactions between heavy components (asphaltene/resin, dimethylnaphtalene, and tetradecane) and all fluid components in the simulation box with H-P clay surfaces.

To investigate the effect of surface chemistry on fluid distribution, the same workflow as previously discussed for the H-P clay surface is also applied to the P-P surface (Figure 2.12 to 2.14). The molecular interactions computed with the P-P surface show similarities to the analysis for the H-P surface. Although these results imply that the spatial distribution of hydrocarbons will be analogous in both surface chemistries, it is important to mention that the P-P and the H-P surfaces have different surface charges. In the next section, I discuss how these surface charges impact the distribution of water in these mixed-wet pore systems.

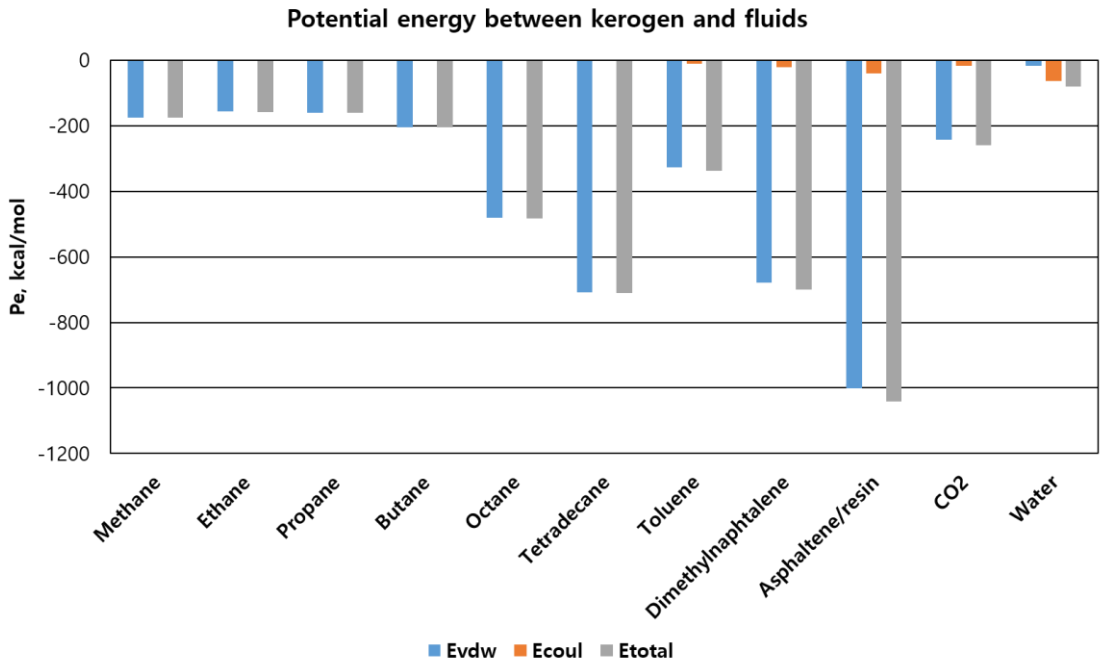

Figure 2.12. Molecular interactions between kerogen and fluid components in the simulation box with P-P clay surfaces.

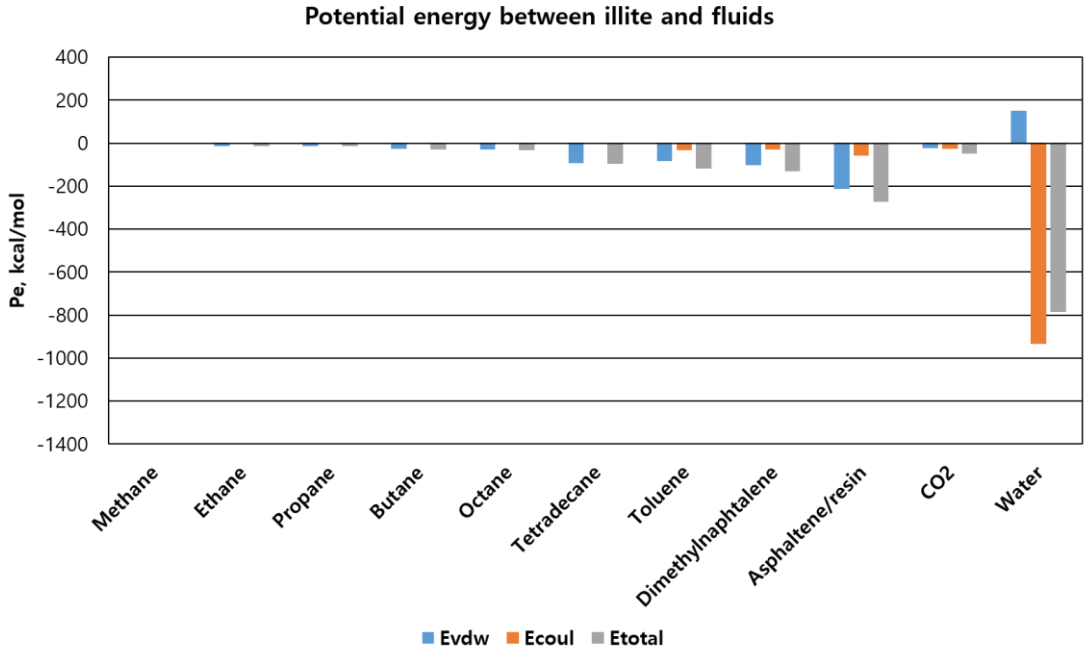

Figure 2.13. Molecular interactions between illite and fluid components in the simulation box with P-P clay surfaces.

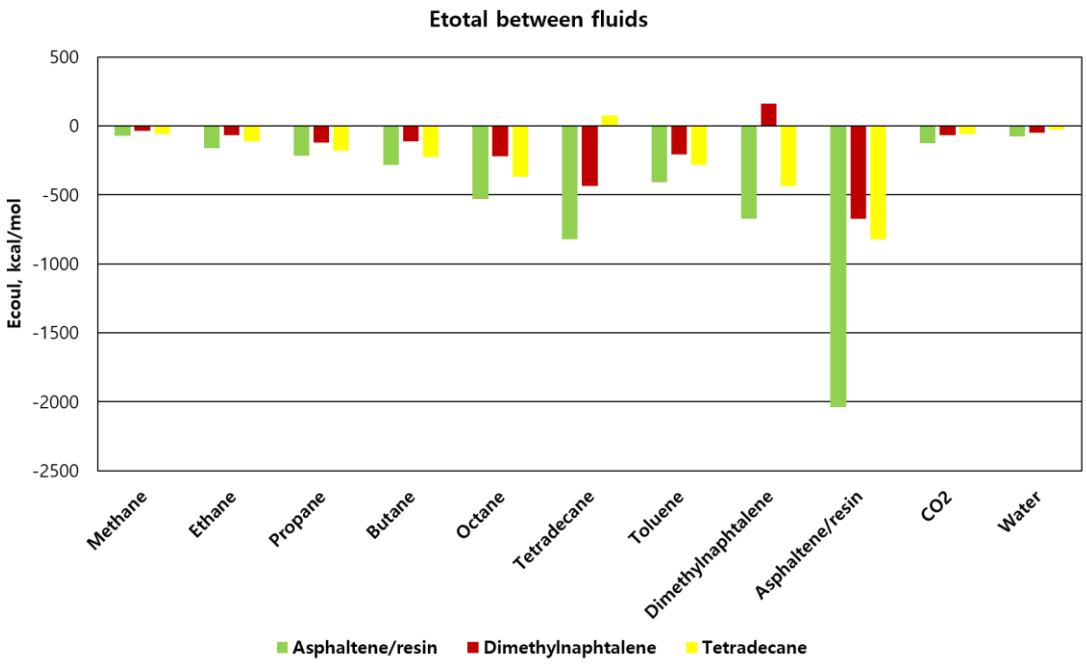

Figure 2.14. Fluid-fluid interactions between heavy components (asphaltene/resin, dimethylnaphtalene, and tetradecane) and all fluid components in the simulation box with P-P clay surfaces.

2.4 The Impact of Changing Water Saturations

In this section, I consider different water saturations in our model and describe the effect of changing saturations on the distribution of water and hydrocarbons. All of the snapshots presented are obtained by using OVITO (Stukowski, 2010).

2.4.1 Distribution of Water

The distribution of water is generally affected by electrostatic interactions with charged surfaces and polar functional groups in other molecules (Yaseen and Mansoori, 2017 and 2018).

Figure 2.15 shows water molecules distributed in the mixed-wet pore model with H-P clay surfaces at a water concentration of 20%. We observe some adsorption of water on the clay surface while several other water molecules are beginning to form a water bridge spanning the entire width of the simulation box (Figure 2.15a) when water is present within kerogen or from one clay surface to the kerogen surface in the absence of water within kerogen (Figure 2.15b). This phenomenon has been previously reported for water confined in clay surfaces (Xiong et al., 2020a; Xiong et al., 2020b; Zhan et al., 2020).

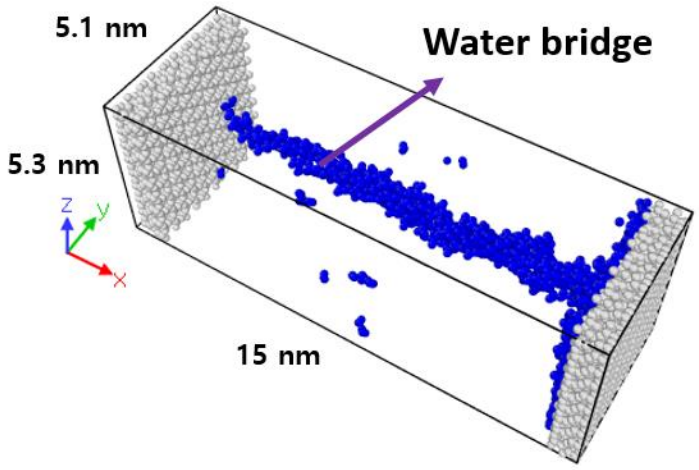

(a) Water molecules form a water bridge from one end of the pore to the other when water is present within kerogen.

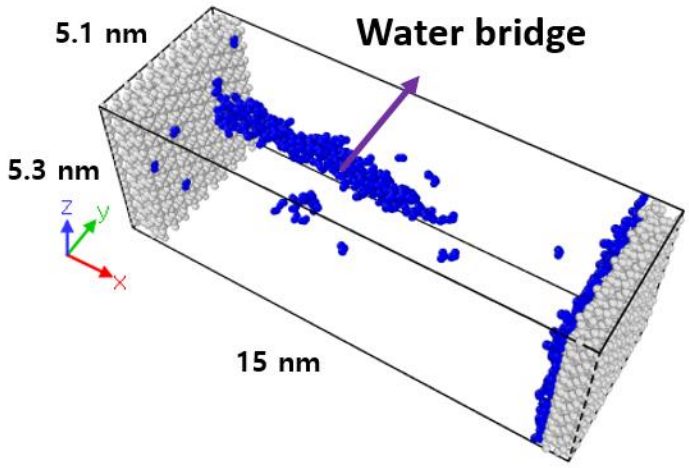

(b) Water molecules form water bridge from one end of the pore and thin water film from other side in the absence of water within kerogen.

Figure 2.15. Spatial distribution of water molecules showing water bridges in the simulation box with H-P clay surfaces at 20% of water concentration. Kerogen is not shown for clarity. Blue color denotes water molecules and gray color shows the atoms included in illite, respectively.

Figure 2.16 presents distribution of water molecules in the simulation box with P-P clay surfaces. Unlike the results in H-P clay surfaces, water is adsorbed to the clay surfaces and also forms water droplets in the pore spaces. Previous studies described that water films on clay surfaces favors hydrocarbon flow by the smooth hydrophilic surfaces while water bridges interrupt the oil flow (Xiong et al., 2020a; Xiong et al., 2020b, Zhan et al., 2020).

Formation of the water bridges and the water films normally occurs by hydrogen bonding, which is defined as an electrostatic interaction between highly electronegative atoms (oxygen, nitrogen, and sulfur) and electropositive atoms (hydrogen) (Desiraju and Steiner, 2001; Yaseen and Mansoori, 2018). Figure 2.15a shows that a sufficient number of water molecules create a water bridge from one end of the pore to the other side by hydrogen bonding. In Figure 2.15b, the bridge extends from one clay surface to kerogen, specifically to the electronegative atoms (nitrogen and sulfur) included in the kerogen monomers. These results indicate that the organic material might interact with water by hydrogen bonding and confirm observations made by Jagadisan and Heidari (2019) for water confined in kerogen.

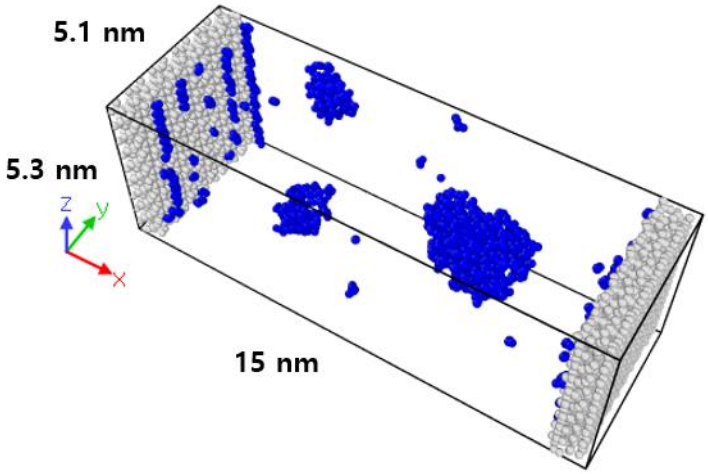

(a) Water molecules form water droplets in mixed wet pore regions and some of water molecules are adsorbed on clay surfaces in the presence of water within kerogen.

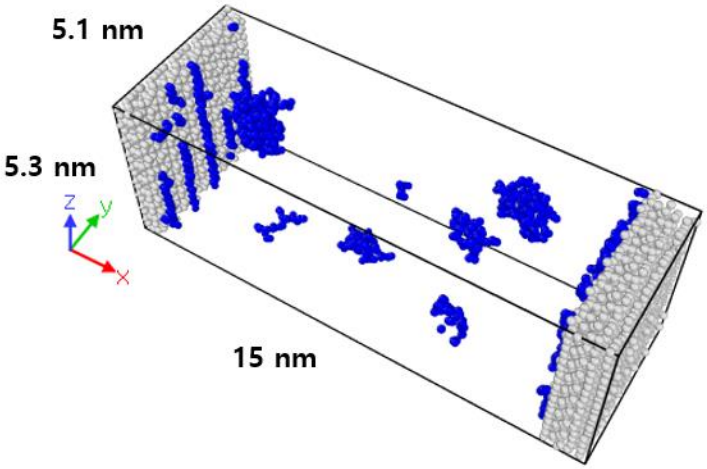

(b) Water molecules form smaller water droplets in mixed wet pore regions and some of water molecules are adsorbed on clay surfaces when water is absent within kerogen.

Figure 2.16. Spatial distribution of water molecules showing water bridges in the simulation box with P-P clay surfaces at 20% of water concentration. Kerogen is not shown for clarity. Blue color denotes water molecules and gray color shows the atoms included in illite, respectively.

Figure 2.17 shows distribution of water molecules in the simulation box with H-P clay surfaces at 40% of water concentration. The snapshots indicate that water bridges are observed as

previously seen with a concentration of water of 20%. The water bridge is however seen to be wider. However, the water bridge spans the entire width of the simulation box from one clay surface to the other irrespective of whether water is present in kerogen or not. Figure 2.18 shows the distribution of water in in the simulation box with P-P clay surfaces denoting an absence of the water bridge. Water is only seen to be adsorbed or form water droplets within the pore spaces. This result confirms similar observations by Xiong et al. (2020a and 2020b).

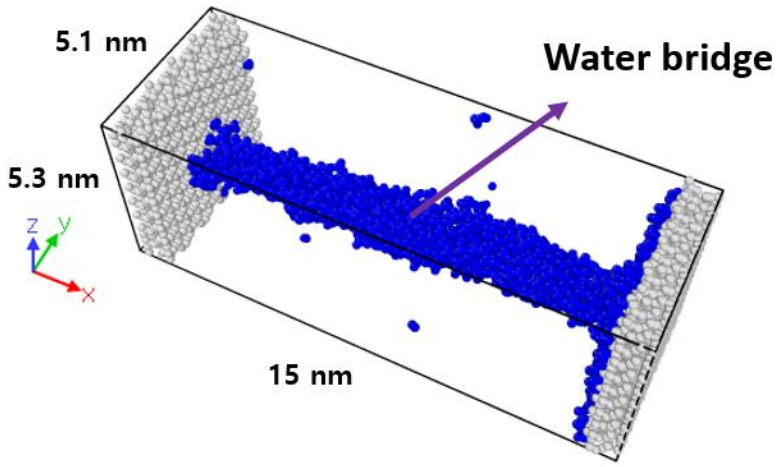

(a) Water molecules form water bridges connecting the two clay surfaces when water is within kerogen.

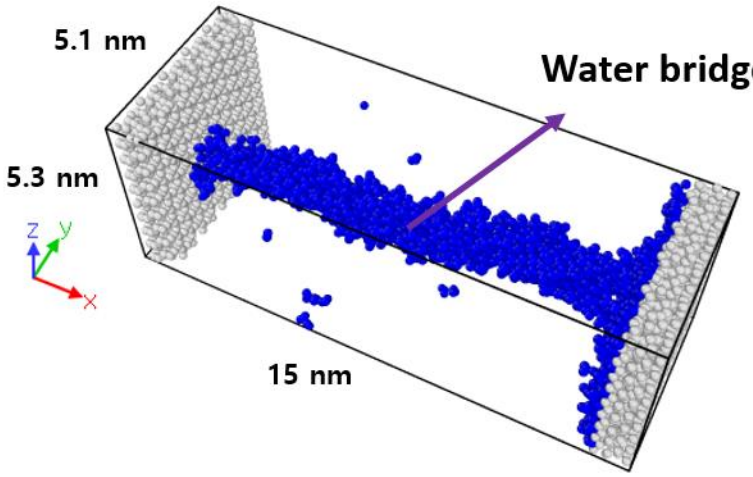

(b) Water molecules form water bridges from one side of the pore to the other side in the absence of water within kerogen.

Figure 2.17. Spatial distribution of water molecules in the simulation box with H-P clay surfaces at 40% of water concentration. Kerogen is not shown for clarity. Blue color denotes water molecules and gray color expresses atoms included in illite, respectively.

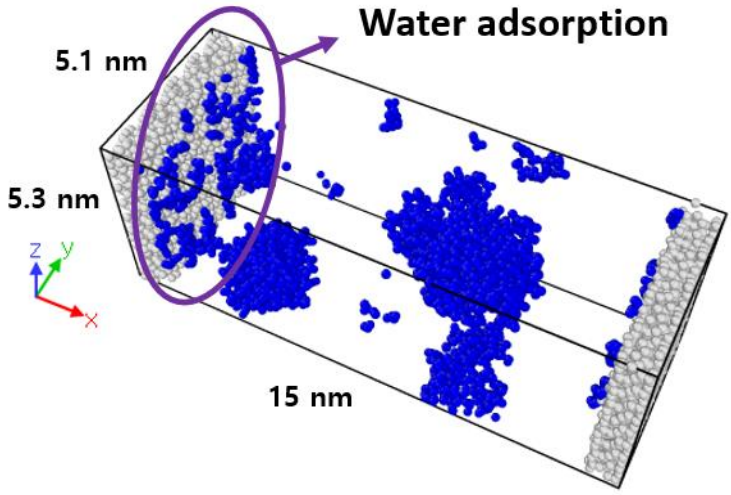

(a) Water molecules form water droplets in mixed wet pore regions and some of water molecules are adsorbed on clay surfaces when water exists within kerogen.

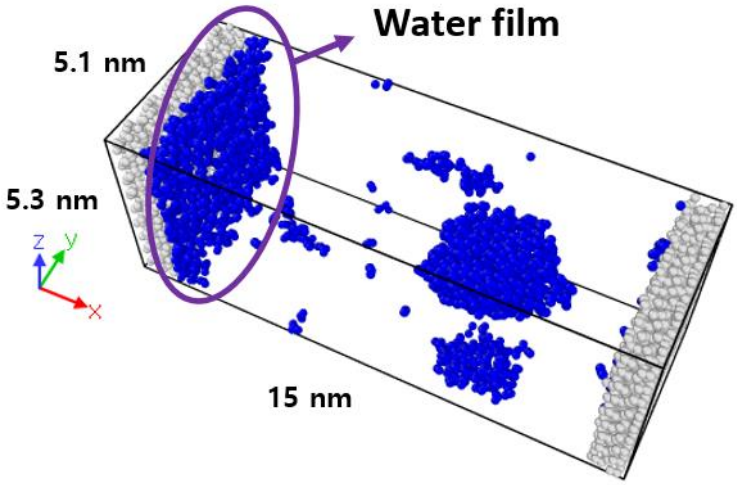

(b) Water molecules form water droplets in mixed wet pore regions and some of water molecules are adsorbed on clay surfaces when water is not within kerogen.

Figure 2.18. Spatial distribution of water molecules in the simulation box with P-P clay surfaces at 40% of water concentration. Kerogen is not shown for clarity. Blue color denotes water molecules and gray color expresses atoms included in illite, respectively.

Figure 2.19 displays snapshots of water distribution in the simulation box with H-P clay surfaces at 60% of water concentration. At the higher water concentration, we observe an even wider water bridge. Xiong et al. (2020a and 2020b) report that wider water bridges in clay pores can inhibit hydrocarbon flow in the pores. Figure 2.20 shows the spatial distribution of water in the simulation box with P-P clay surfaces. Water bridges are seen to be absent and water is largely adsorbed on to the positively charged clay surfaces.

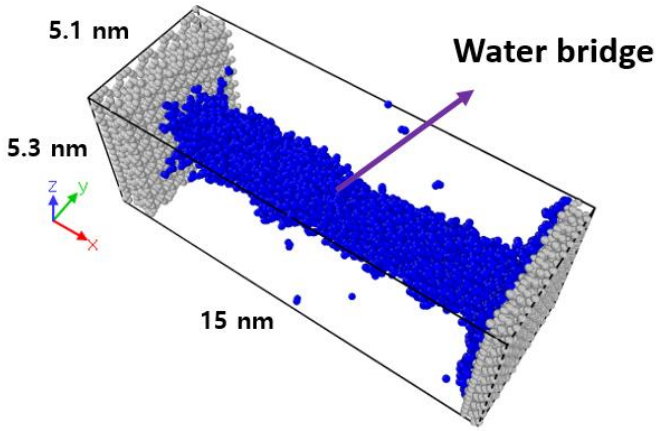

(a) Water molecules form water bridges connecting the two clay surfaces when water is within kerogen.

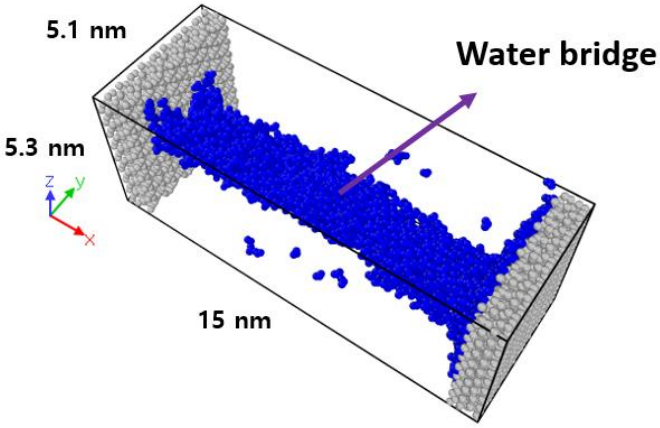

(b) Water molecules form water bridges from one side of the pore to the other side in the absence of water within kerogen.

Figure 2.19. Spatial distribution of water molecules in the simulation box with H-P clay surfaces at 60% of water concentration. Kerogen is not shown for clarity. Blue color denotes water molecules and gray color expresses atoms included in illite, respectively.

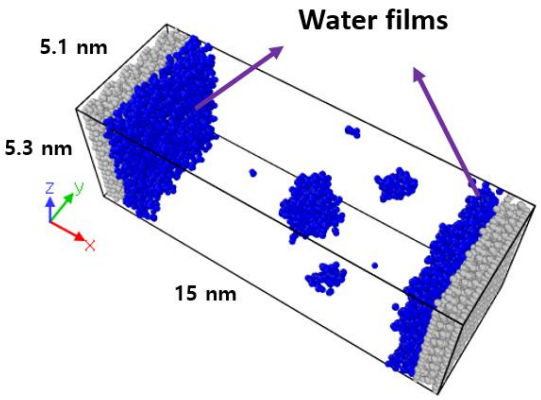

(a) Water molecules form water films on the clay surfaces when water exists within kerogen.

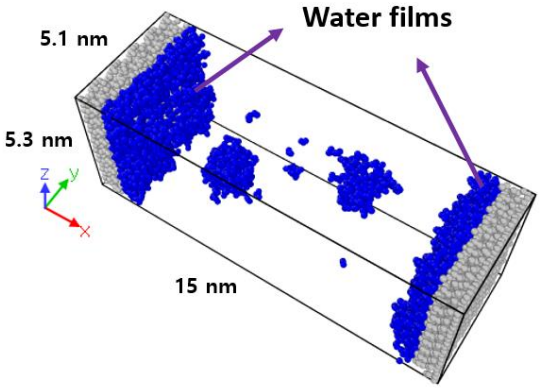

(b) Water molecules form water films on the clay surfaces when water is not within kerogen.

Figure 2.20. Spatial distribution of water molecules in the simulation box with P-P clay surfaces at 60% of water concentration. Kerogen is not shown for clarity. Blue color denotes water molecules and gray color expresses atoms included in illite, respectively.

Figure 2.21 shows water distribution in the simulation box with H-P clay surfaces at 80% of water concentration. As seen at 80% of water concentration, water bridge becomes wider as the water concentration is increased. In this case, end face of the water bridge covers almost of the

clay surfaces. Figure 2.22 present water distribution in the simulation box with P-P clay surfaces at the same water concentration as Figure 2.21. The higher water concentration formed thicker water films on clay surfaces. Xiong et al. (2020a) and Zhan et al. (2020) observed hydrocarbon molecules were clustered because thick water film could limit access of hydrocarbons to clay surfaces. From next section, I will describe how the formation of water bridge and film affect hydrocarbon distribution in mixed-wet nanopores.

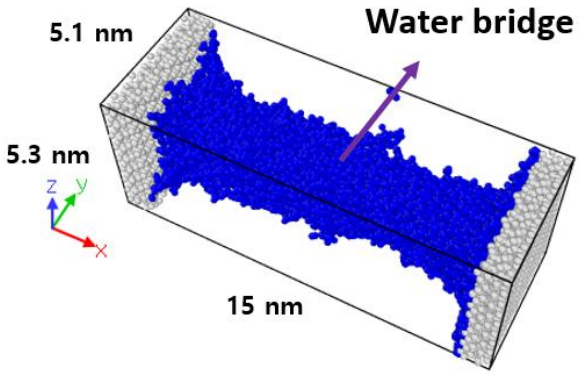

(a) Water molecules form water bridge from one end to the other of the clay surfaces when water exists within kerogen.

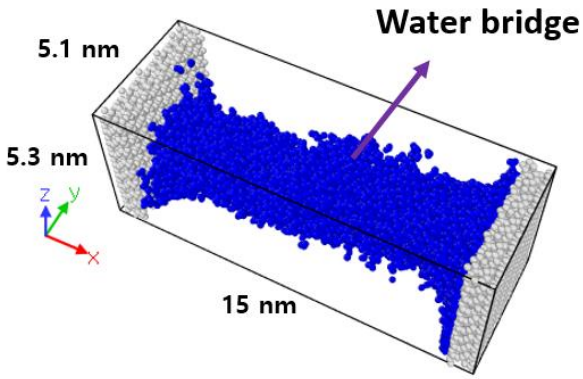

(b) Water molecules form water bridge connecting the two clay surfaces when water is not within kerogen.

Figure 2.21. Spatial distribution of water molecules in the simulation box with H-P clay surfaces at 80% of water concentration. Kerogen is not shown for clarity. Blue color denotes water molecules and gray color expresses atoms included in illite, respectively.

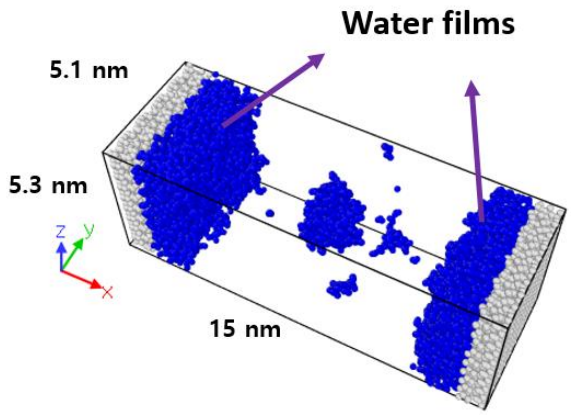

(a) Water molecules form water films on the clay surfaces when water exists within kerogen.

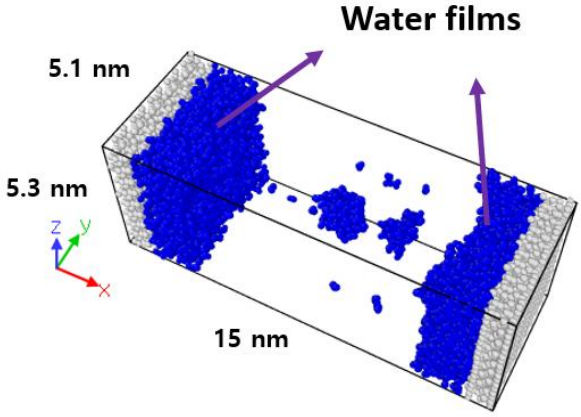

(b) Water molecules form water films on the clay surfaces when water is not within kerogen.

Figure 2.22. Spatial distribution of water molecules in the simulation box with P-P clay surfaces at 80% of water concentration. Kerogen is not shown for clarity. Blue color denotes water molecules and gray color expresses atoms included in illite, respectively.

2.4.2 Distribution of the Light (Methane and Ethane) and Intermediate (Propane and Butane) Components

Figure 2.23 presents snapshots of the light and intermediate hydrocarbons in the mixed-wet pore system with the H-P clay surface for different values of water saturation. It also shows the distribution of water within the simulation box. The light and intermediate components are spatially dispersed state irrespective of the value of water concentration. At over 20% water concentration, all the simulation cases show that the thickness of the water bridges increases with increases in water concentration.

Water concentration = 20%

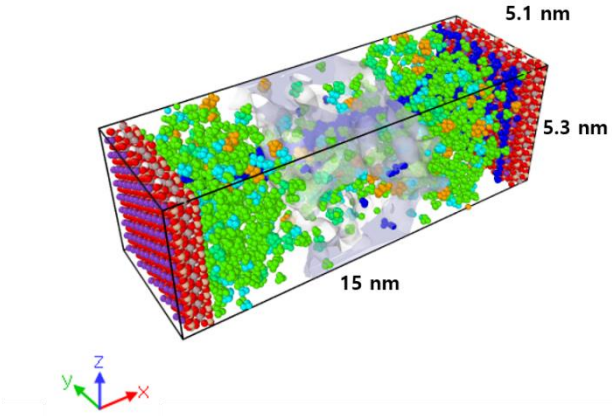

Water concentration = 40%

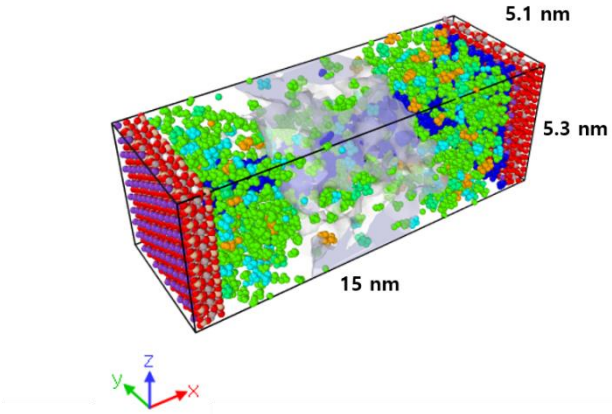

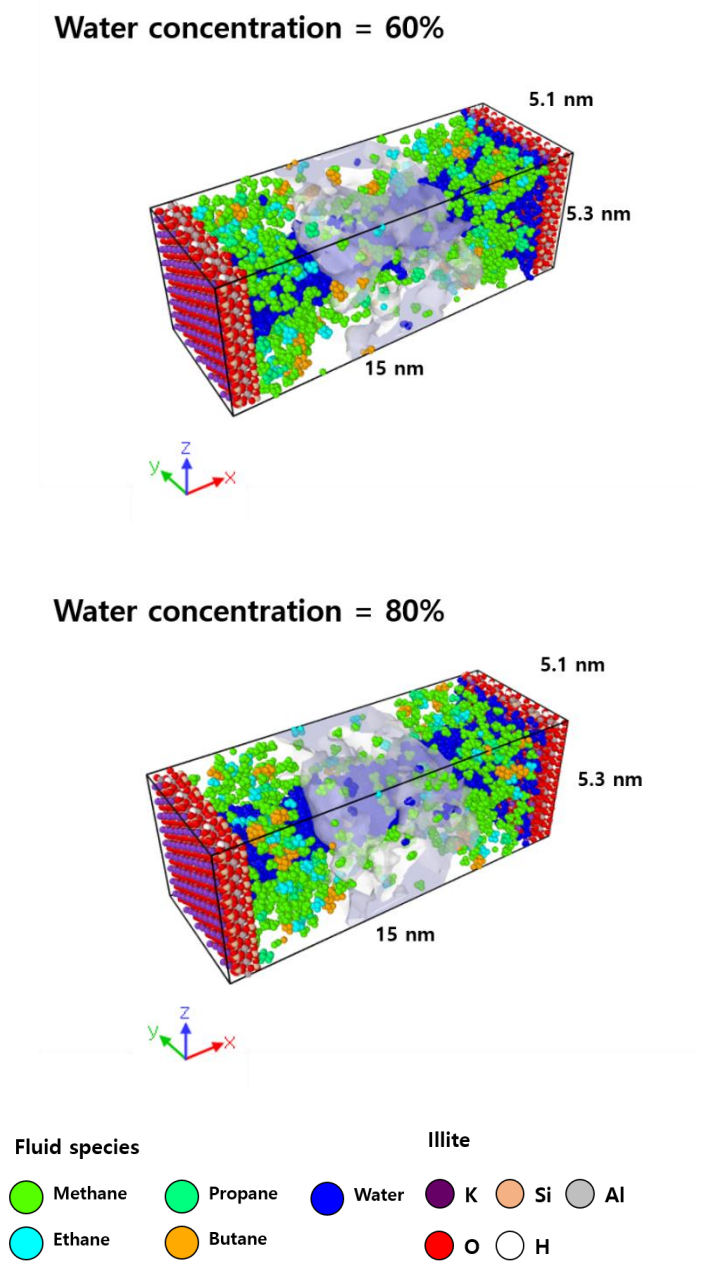

(a) Light and intermediate hydrocarbon species dispersed at different water concentrations in mixed-wet pores when water is within kerogen. The water bridge across kerogen occupies some portion of organic pore body which the hydrocarbon species can fill the pore space.

Water concentration = 20%

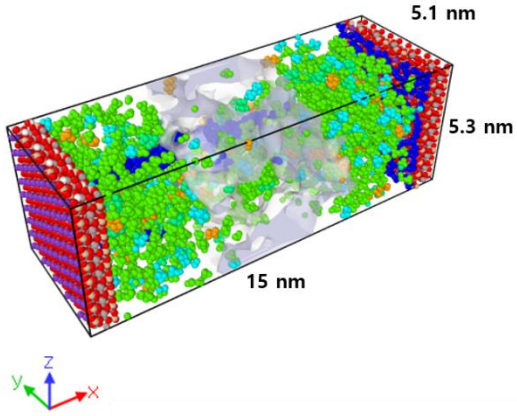

Water concentration = 40%

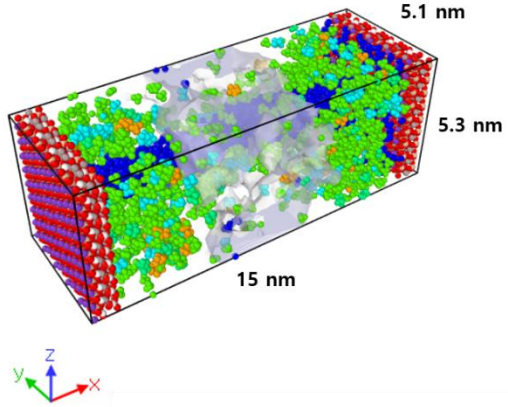

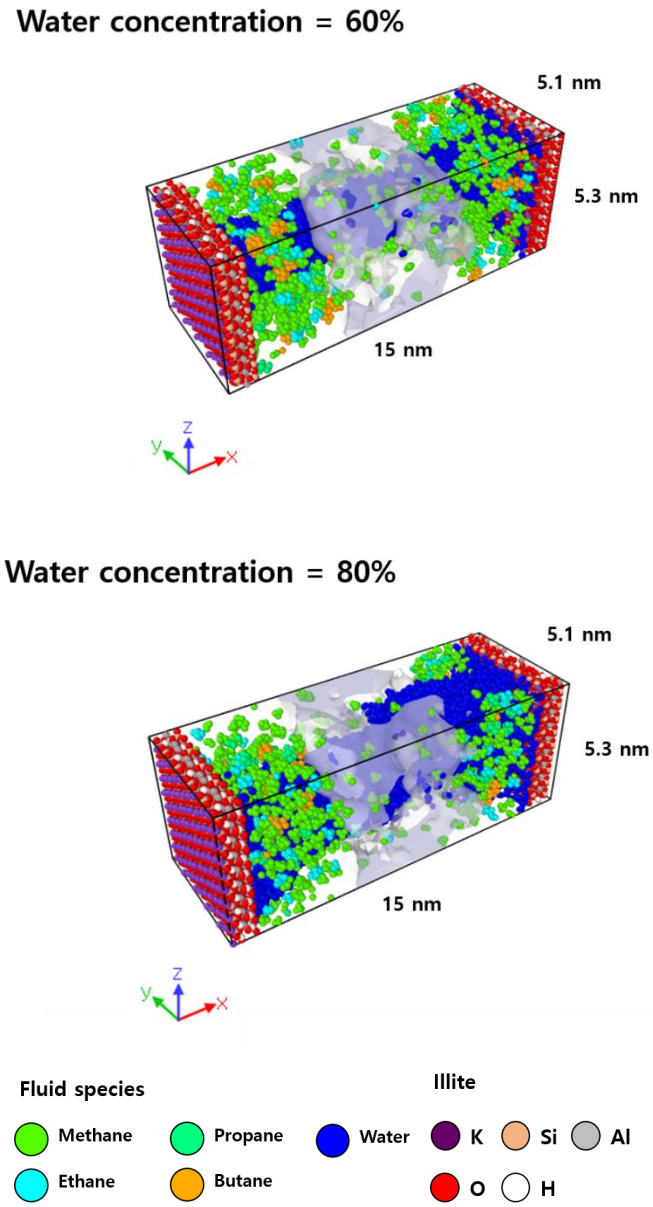

(b) Light and intermediate hydrocarbon species dispersed at different water concentrations in mixed-wet pores in the absence of water within kerogen. The water bridge across kerogen occupies some portion of organic pore body which the hydrocarbon species can fill the pore space.

Figure 2.23. Distribution of light and intermediate hydrocarbons in the simulation box with H-P clay surfaces. Kerogen is translucent for distinct visualization of fluid molecules.

Figure 2.24 presents the distributions of light and intermediate hydrocarbons when P-P clay surfaces are present for different values of water saturation. The overall distribution of water remains the same for all values of water concentration. At higher water concentration values, the thickness of the adsorbed water layer increases. Irrespective of the type of clay surface, the light and intermediate components mainly form the free fluid phase regardless of the water saturation. This implies that they can easily be produced relative to the adsorbed components as reported by Perez and Devegowda (2019 and 2020).

Water concentration = 20%

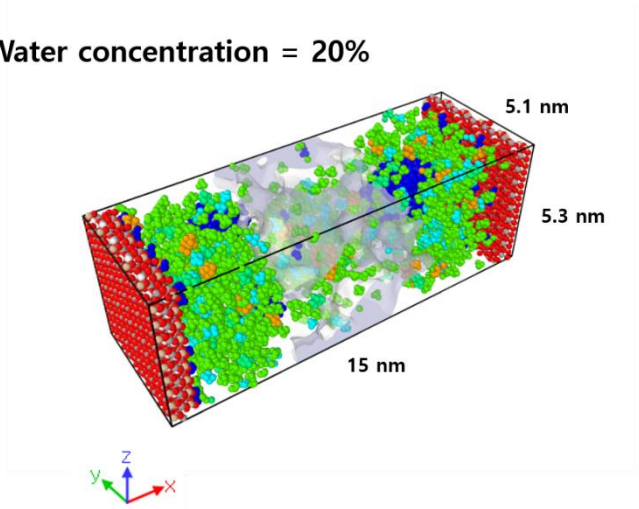

Water concentration = 40%

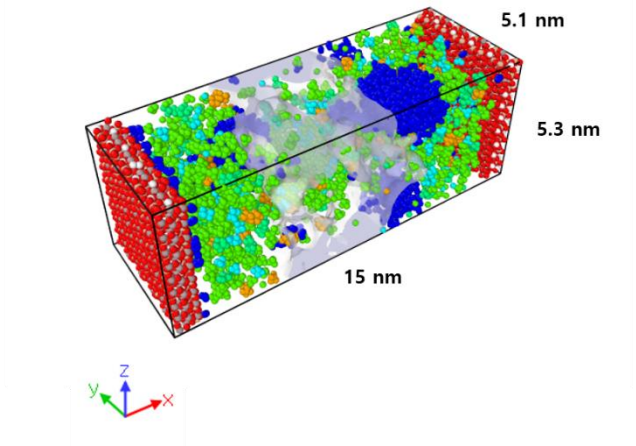

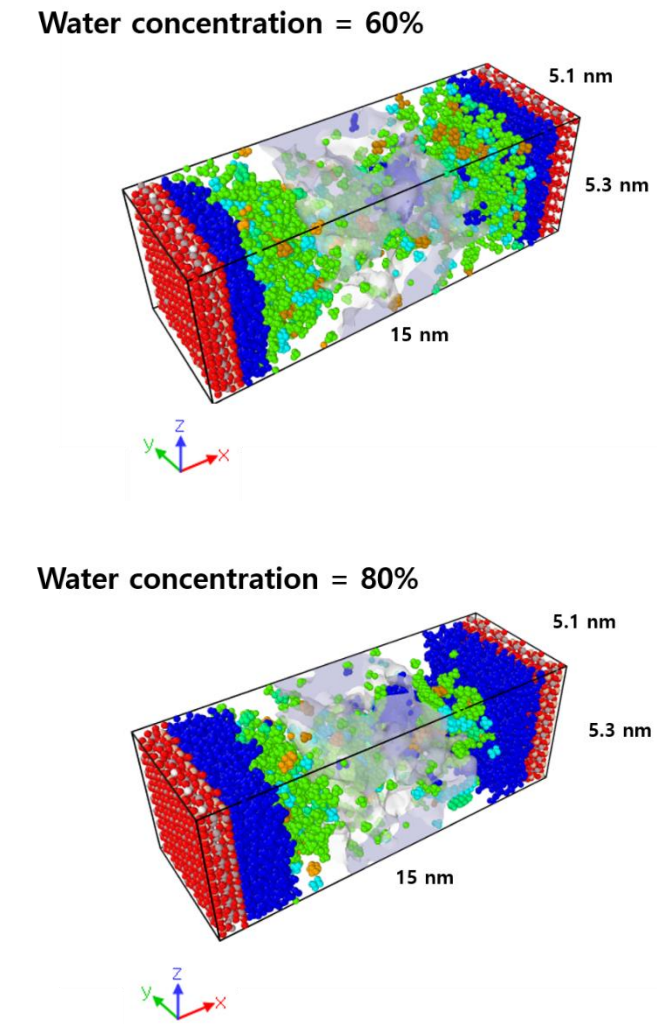

(a) Light and intermediate hydrocarbon species are dispersed at different water concentrations in mixed-wet pores when water is within kerogen. The water films limit access of the hydrocarbon species onto clay surfaces.

Water concentration = 20%

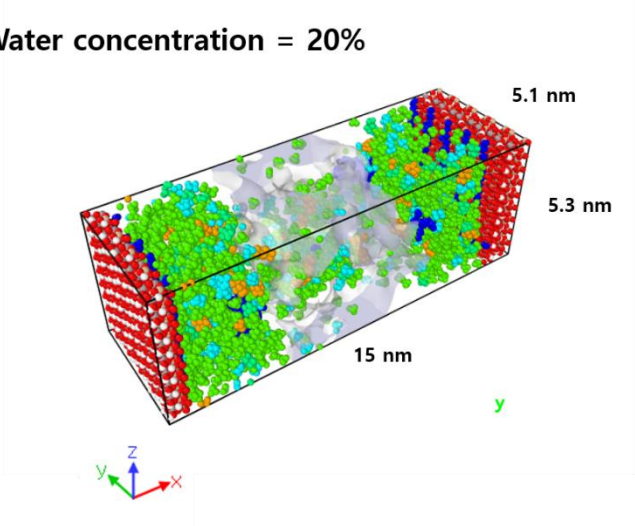

Water concentration = 40%

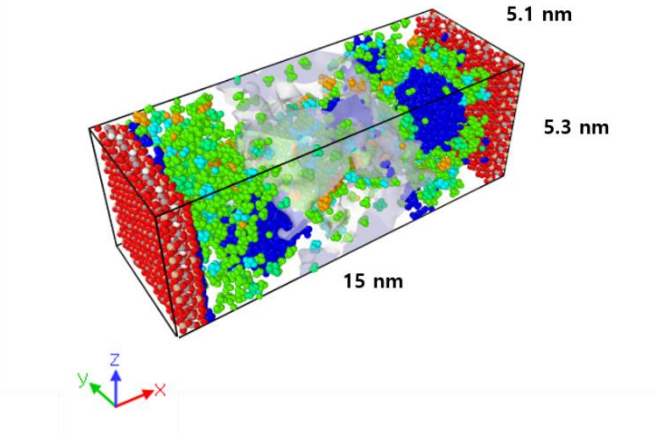

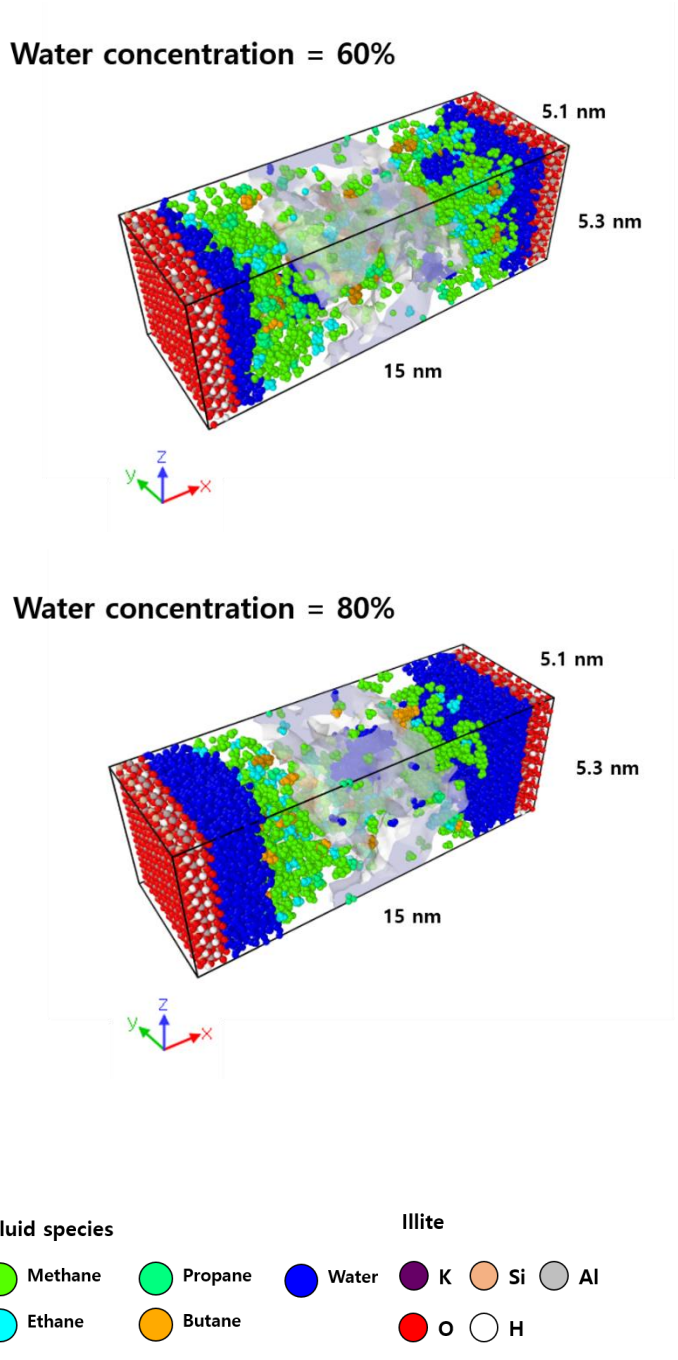

(b) Light and intermediate hydrocarbon species are also dispersed at different water concentrations in mixed-wet pores in the absence of water within kerogen. The water films also limit access of the hydrocarbon species onto clay surfaces.

Figure 2.24. Distribution of light and intermediate hydrocarbons in the simulation box with P-P clay surfaces. Kerogen is translucent for distinct visualization of fluid molecules.

2.4.3 Distribution of Heavy Components (Octane, Tetradecane, and Toluene)

Figure 2.25 displays the distribution of the heavy components (octane, tetradecane, and toluene) in the simulation box with H-P surfaces. Comparison between Figures 2.25a and 2.25b implies that the octane and tetradecane fraction are largely seen to be adsorbed on the kerogen surfaces. Additionally, because these molecules are entirely non-polar, they rarely interact with water. Toluene tends to be spatially dispersed compared to the other heavy components and can act as an organic solvent for the heavy ends. Figure 2.26 shows the distribution of the three heavy ends in the simulation box with P-P clay surfaces. Their distribution is also similar to the H-P surface, except that the existence of water films impedes approach of the heavy species onto clay surfaces. During primary production, interfacial behavior of the three heavy ends on water films may enhance their mobility by liquid-liquid slip (Zhan et al., 2020).

Water concentration = 20%

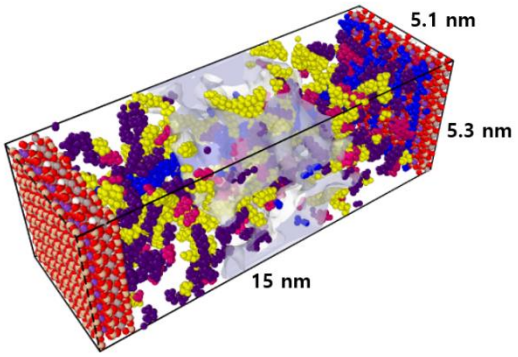

Water concentration = 40%

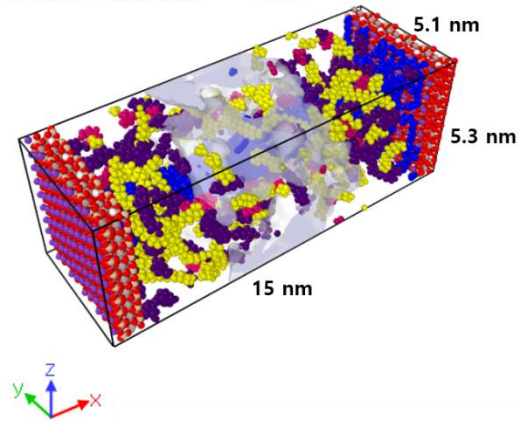

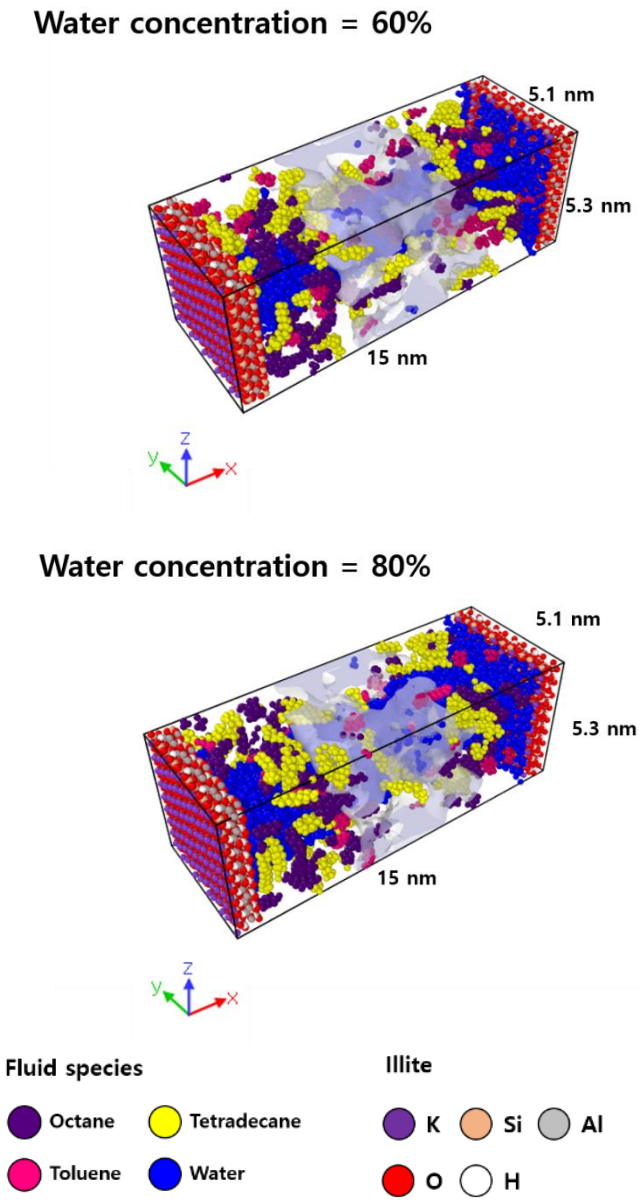

(a) Heavy hydrocarbon species (octane, tetradecane, and toluene) spaciously distributed at different water concentrations in mixed-wet pores when water is within kerogen. The water bridge across kerogen occupies the organic pore surfaces which the hydrocarbon species can be adsorbed.

Water concentration = 20%

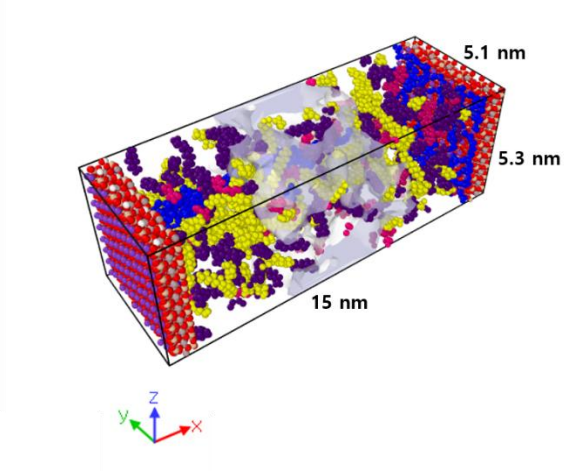

Water concentration = 40%

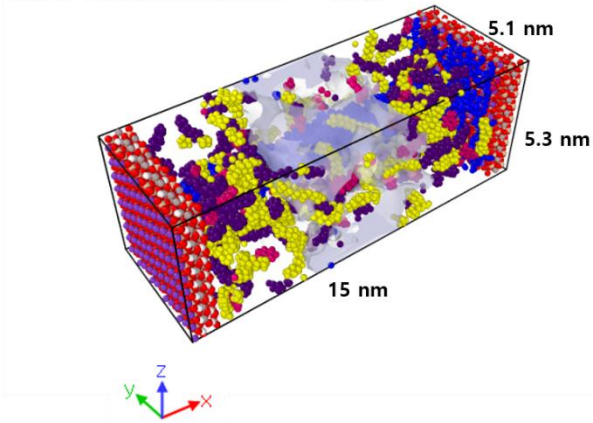

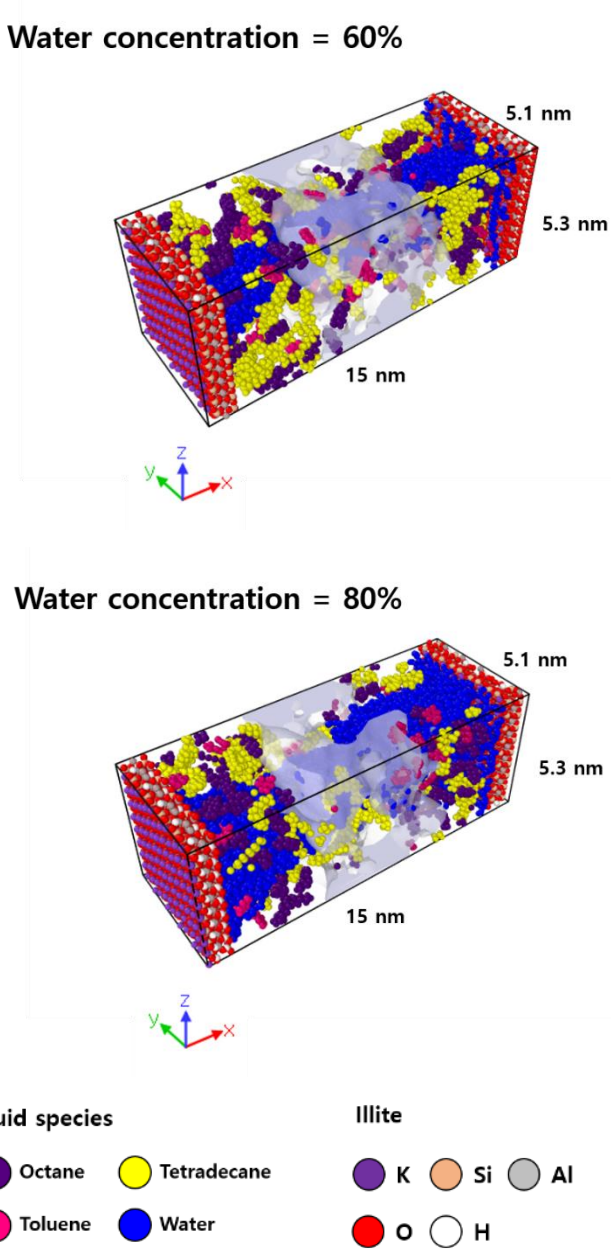

(b) Heavy ends (octane, tetradecane, and toluene) dispersed at different water concentrations in mixed-wet pores in the absence of water within kerogen. Moderate amounts of the heavy species are adsorbed onto kerogen surface and the water bridge across kerogen occupies the organic pore surfaces which the hydrocarbon species can be adsorbed.

Figure 2.25. Distribution of heavy hydrocarbons (octane, tetradecane, and toluene) in the simulation box with H-P clay surfaces. Kerogen is translucent for distinct visualization of fluid molecules.

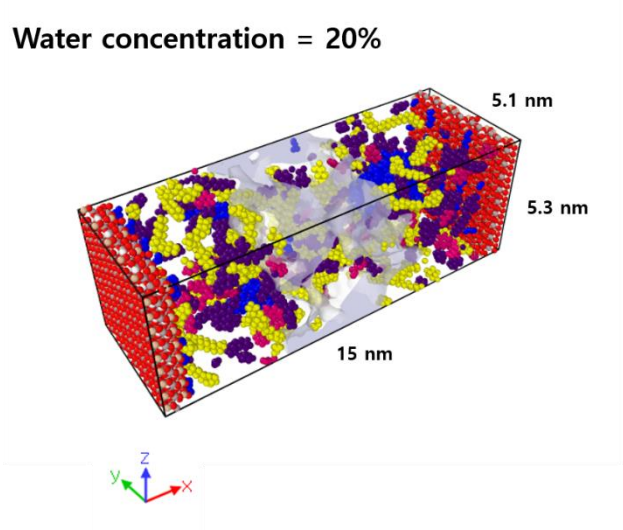
Water concentration = 20%
5.1 nm
5.3 nm
15 nm
z
y
x

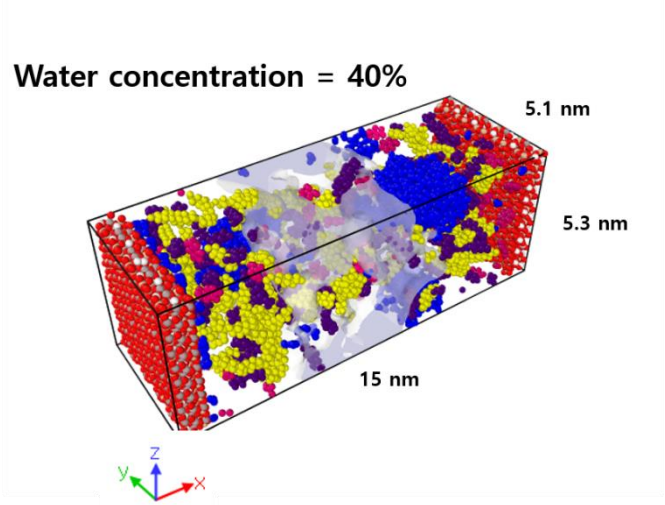
Water concentration = 40%
5.1 nm
5.3 nm
15 nm
z
y
x

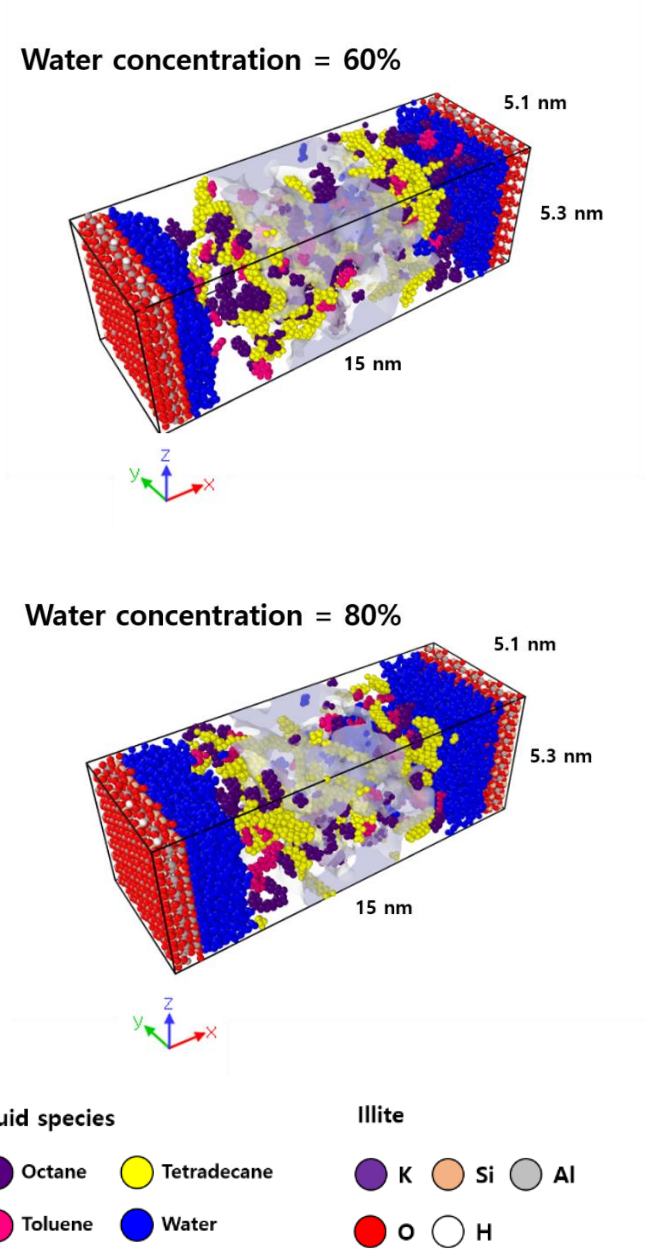

(a) Heavy hydrocarbon species (octane, tetradecane, and toluene) are distributed at different water concentrations in mixed-wet pores when water is within kerogen. Moderate amounts of the heavy species are adsorbed onto kerogen surface and the water bridge across kerogen occupies the organic pore surfaces which the hydrocarbon species can be adsorbed.

Water concentration = 20%

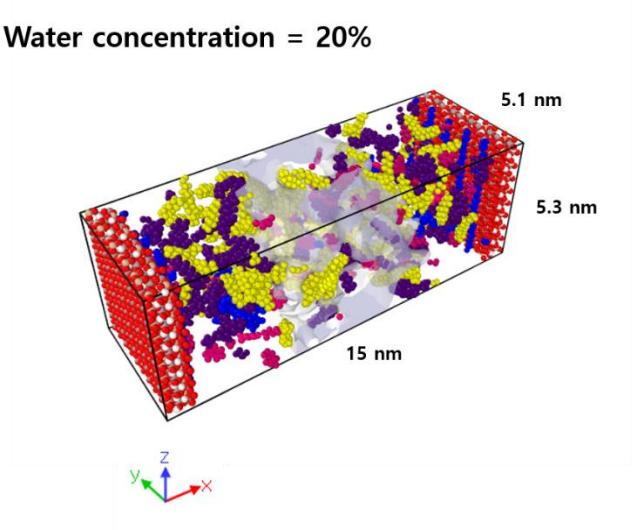

Water concentration = 40%

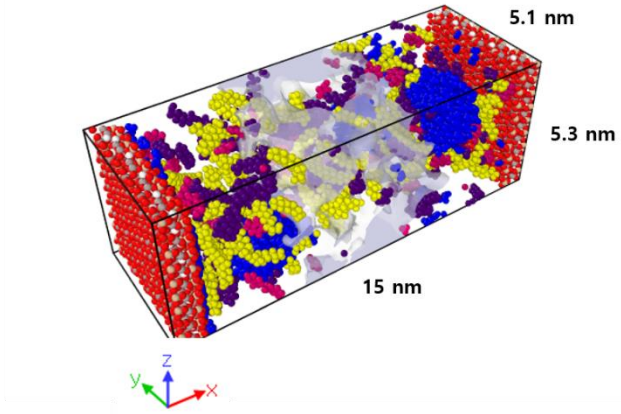

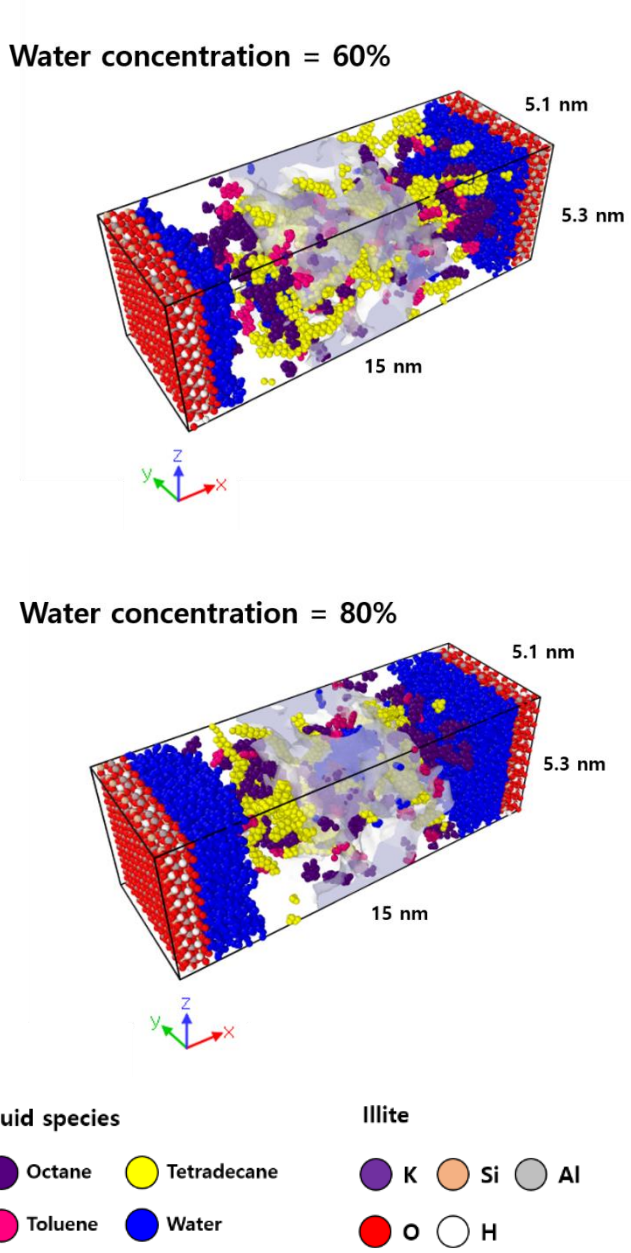

(b) Heavy ends (octane, tetradecane, and toluene) distributed at different water concentrations in mixed-wet pores in the absence of water within kerogen. Moderate amounts of the heavy species are adsorbed onto kerogen surface and the water bridge across kerogen occupies the organic pore surfaces which the hydrocarbon species can be adsorbed.

Figure 2.26. Distribution of heavy hydrocarbons (octane, tetradecane, and toluene) in the simulation box with P-P clay surfaces. Kerogen is translucent for distinct visualization of fluid molecules.

2.4.4 Distribution of the Heavy Components (Dimethylnaphtalene and Asphaltene/resin)

Figure 2.27 shows distribution of the dimethylnaphtalene and asphaltene/resin fractions in the simulation box with H-P clay surfaces. The methyl group of dimethylnaphtalene is linked with water by hydrogen bonding with the oxygen atoms in water, as shown in Figure 2.28. Another observation is that hydrogen bonding between water on the illite plane and asphaltene/resin fraction creates asphaltene films adjacent to the adsorbed water. This is an interesting observation because the surface of the clays become hydrophobic in contrast to the commonly accepted hydrophilic definition of clays. Increases in water concentration between the clay surface and kerogen also makes the water bridges wider. The heavier components are seen to be surrounding the water bridge through hydrogen bonding or adsorbed on the kerogen surface.

Water concentration = 20%

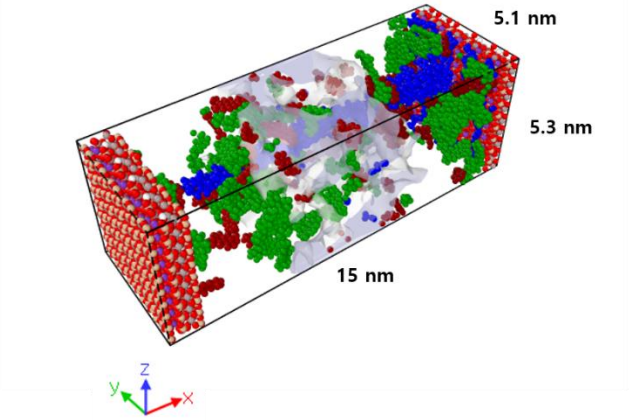

Water concentration = 40%

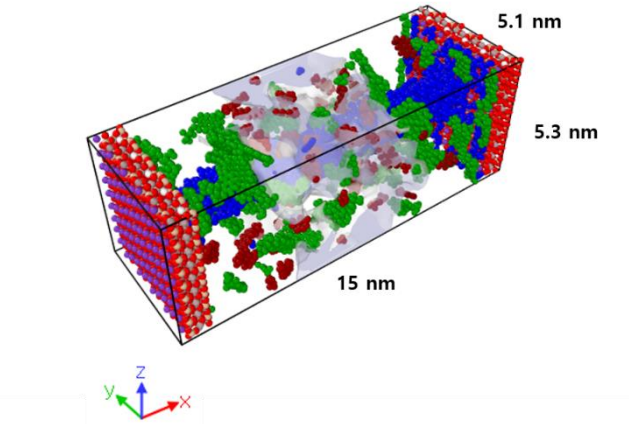

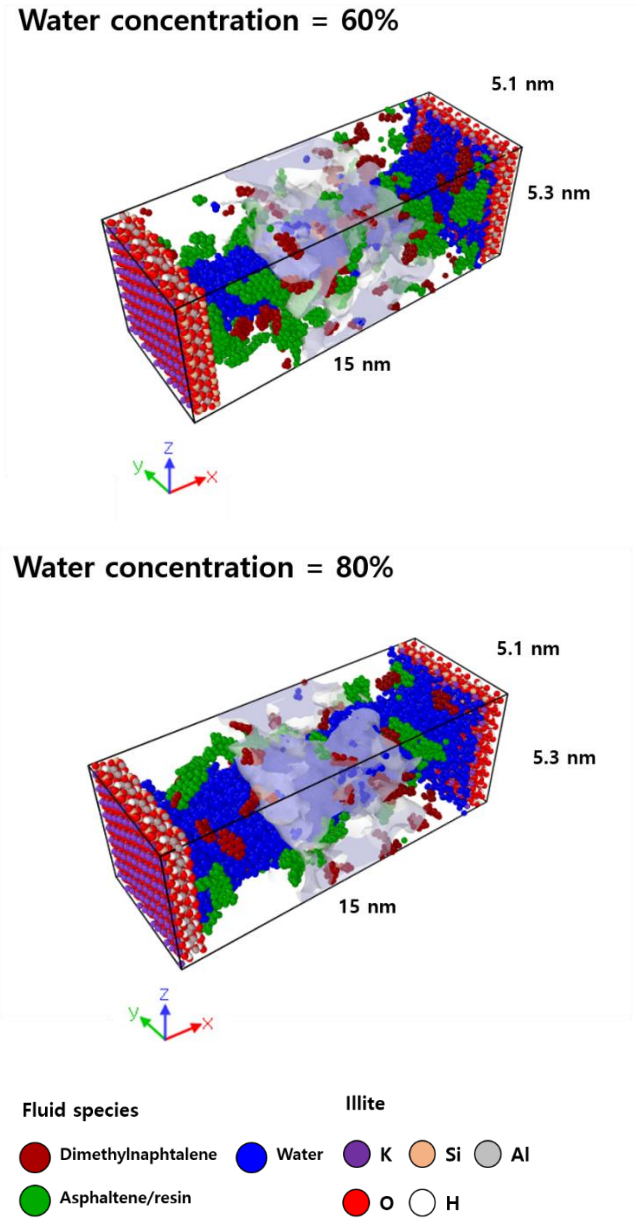

(a) Two heavy hydrocarbon species (dimethylnaphtalene and asphaltene/resin) distributed at different water concentrations in mixed-wet pores when water is within kerogen. Most of the heavy species are adsorbed onto kerogen surface. Some of them are attracted to adsorbed water layer on clay surfaces or dispersed around water bridges by hydrogen bond.

Water concentration = 20%

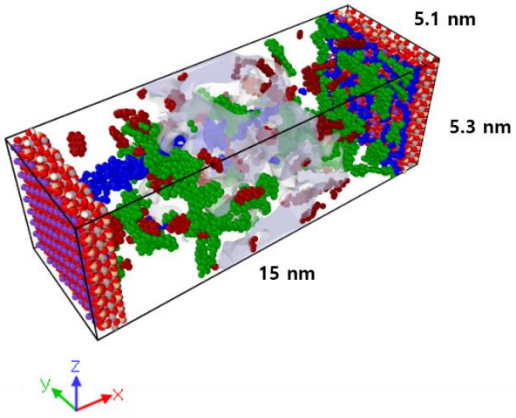

Water concentration = 40%

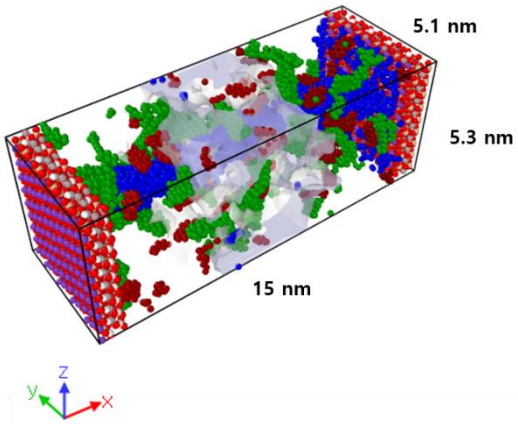

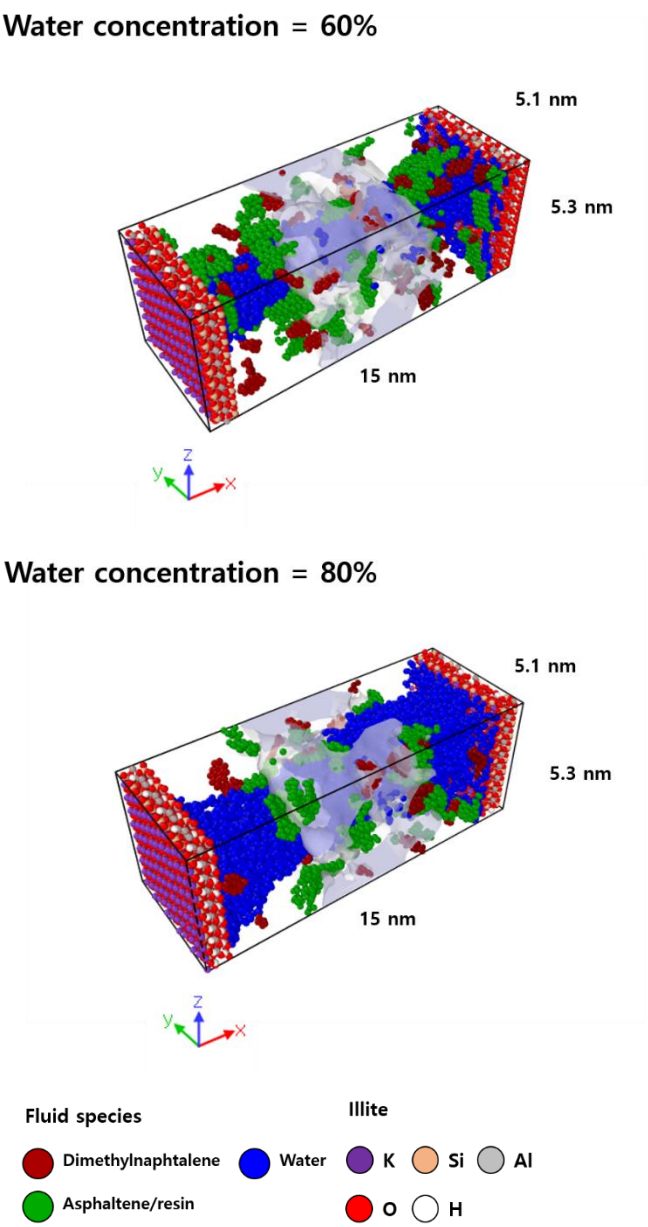

(b) Two heavy ends (dimethylnaphtalene and asphaltene/resin) distributed at different water concentrations in mixed-wet pores in the absence of water within kerogen. Most of the heavy species are adsorbed onto kerogen surface. Some of them are attracted to adsorbed water layer on clay surfaces or dispersed around water bridges by hydrogen bond.

Figure 2.27. Distribution of heavy hydrocarbons (dimethylnaphtalene and asphaltene/resin) in the simulation box with H-P clay surfaces. Kerogen is translucent for distinct visualization of fluid molecules.

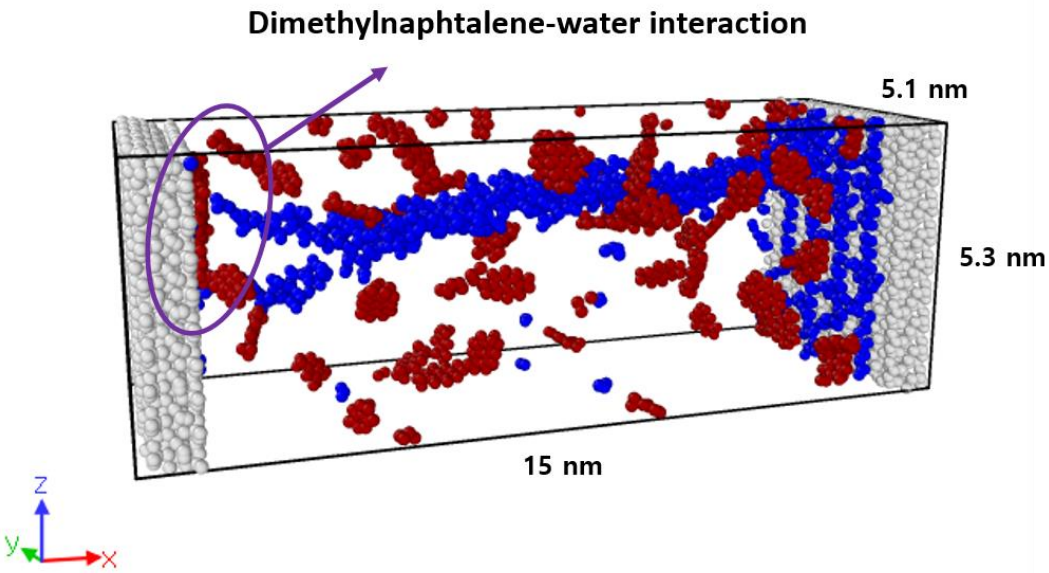

Figure 2.28. A snapshot showing dimethylnaphtalene-water interaction in the simulation box with H-P clay surface at 20% of water concentration. Dark red color denotes dimethylnaphtalene molecules, blue color for water molecules, and gray color express atoms included in illite. Kerogen is not shown for clarity.

With P-P clay surfaces (Figure 2.29), both dimethylnaphtalene and asphaltene/resin show similar spatial distribution to that in the H-P surface when the water concentration is below 50%. However, at higher than 50% water concentration, most of the two heavy ends are adsorbed on the organic surfaces, as strong hydration forces between water and the positively charged clay surfaces develop water films that obstruct contact of the heavy ends with the illite surfaces.

The distribution of fluids in mixed-wet pores is worthy of a very detailed discussion. However, because the details can be challenging to keep track of, I present a summary of all observations in Table 2.2. The table indicates that the opposite charge distribution of clay surfaces lead to formation of water bridges while the same charge distribution generated water films on the clay surfaces. Of hydrocarbon species higher fraction of asphaltene/resin molecules, including polar group, alters surface wettability of clay minerals to partially hydrophobic. The other heavy ends are mostly adsorbed to kerogen surfaces and light and intermediate hydrocarbons are dispersed as free fluid phase in the mixed-wet pores. Thus, this chapter suggest that we should take account for the effect of hydrocarbon species to surface wettability in mixed-wet shale nanopores.

Water concentration = 20%

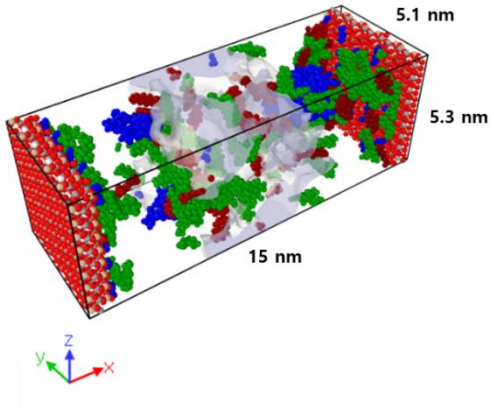

Water concentration = 40%

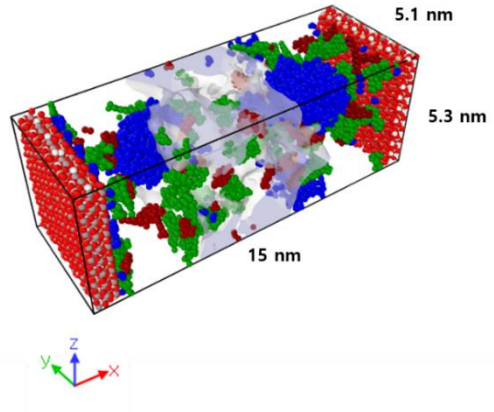

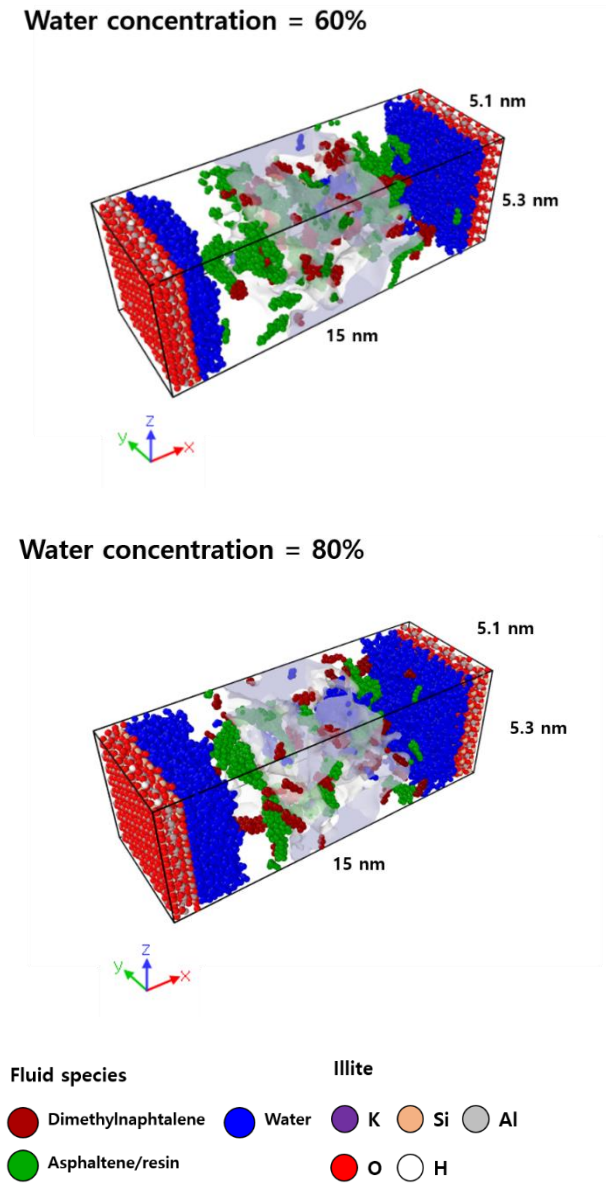

(a) Two heavy hydrocarbon species (dimethylnaphtalene and asphaltene/resin) dispersed at different water concentrations in mixed-wet pores when water is within kerogen. Most of the heavy species are adsorbed onto kerogen surface and some of them are attracted to adsorbed water layer on clay surfaces below 50% of water concentration. The heavy ends are mostly adsorbed onto kerogen surfaces because water films limit their access to clay surfaces.

Water concentration = 20%

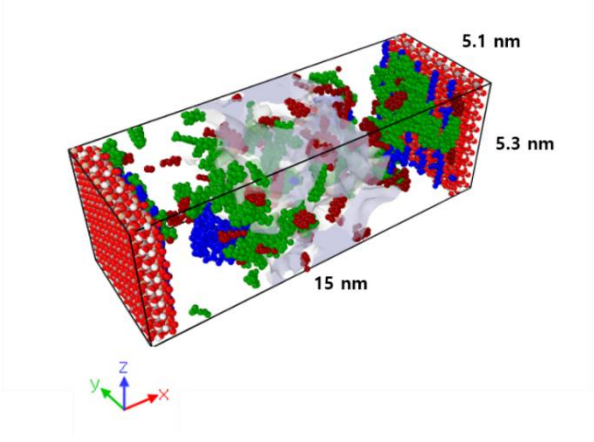

Water concentration = 40%

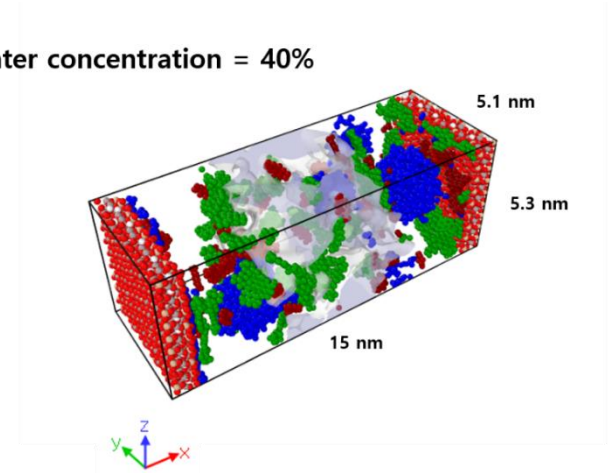

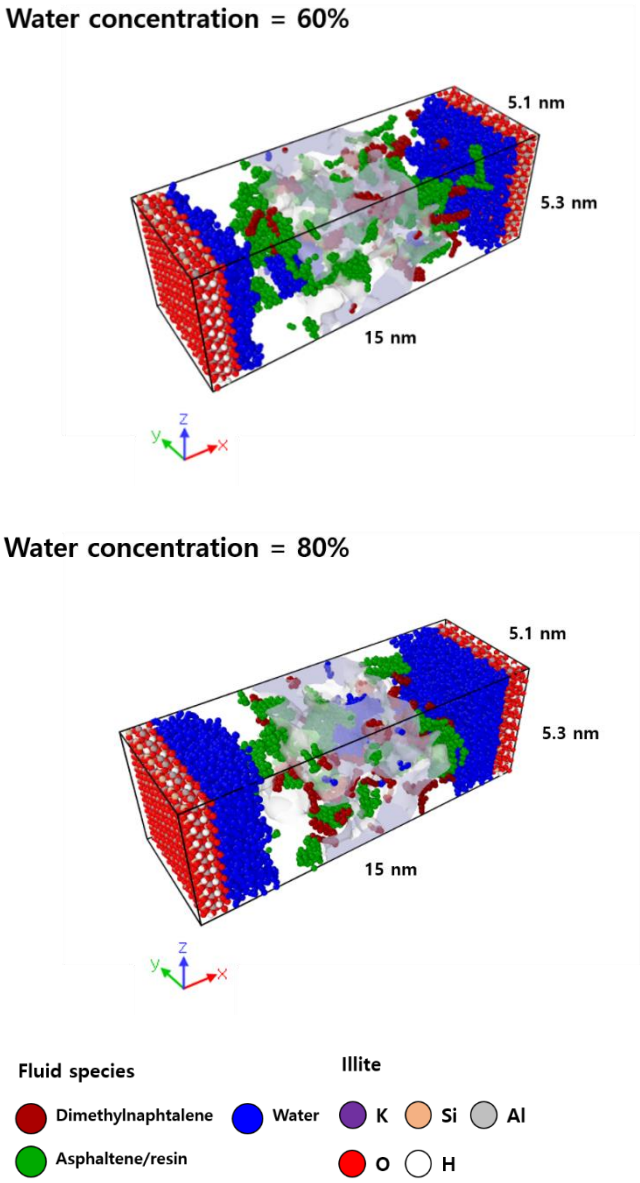

(b) Two heavy ends (dimethylnaphtalene and asphaltene/resin) distributed at different water concentrations in mixed-wet pores in the absence of water within kerogen. Most of the heavy species are adsorbed onto kerogen surface and some of them are attracted to adsorbed water layer on clay surfaces below 50% of water concentration. The heavy ends are mostly adsorbed onto kerogen surfaces because water films limit their access to clay surfaces.

Figure 2.29. Distribution of heavy hydrocarbons (dimethylnaphtalene and asphaltene/resin) in the simulation box with P-P clay surfaces. Kerogen is translucent for distinct visualization of fluid molecules.

Table 2.2. Spatial distribution of fluid molecules and wettability conditions in the simulation box with different surface chemistries of clay minerals.

Model #	Clay Surfaces	Water Concentration, %	Water Bridge/ Adsorbed/ Droplets	Asphaltene/ Resin fraction	Heavy Ends	Intermediate species	Light Ends	Wettability
1	H-P	20	A, B	A	A, F	F	F	Partially Hydrophobic
2	H-P	40	A, B	A	A, F	F	F	Partially Hydrophobic
3	H-P	60	A, B	A	A, F	F	F	Less Hydrophobic
4	H-P	80	A, B	A	A, F	F	F	Less Hydrophobic
5	P-P	20	A, D ,	A	A, F	F	F	Partially Hydrophobic
6	P-P	40	A, D	A	A, F	F	F	Partially Hydrophobic
7	P-P	60	A, D	A	A, F	F	F	Less Hydrophobic
8	P-P	80	A, D	A	A, F	F	F	Less Hydrophobic

Legend:
A: Adsorbed
B: Bridge
D: Droplets
F: Free-fluid phase

2.5 Self-Diffusion of Fluid Molecules in Mixed-Wet Shale Pores

2.5.1 Self-Diffusion Coefficients

In this section, I investigate the self-diffusion coefficients of all fluid components at the pressure and temperature conditions of the simulation. The self-diffusivity can be calculated by the following two methods:

1. Mean square displacement (MSD) related to the observation time (Frenkel and Smit, 2002; Liu et al., 2018)
2. Velocity autocorrelation based on a Green-Kubo relation (Allen and Tildesley, 2017).

The two methods provide identical results, but the velocity auto-correlation method can be very time-consuming. The MSD method is therefore generally recommended to estimate the self-diffusivity (Keffer, 2002). The definition of MSD is given in Eq. (4), where N is the number of particles to be averaged, $x_n(0)$ = 0 is the reference position of each particle, and $x_n(t)$ is the position of each particles at a specific time, t. Finally, the self-diffusion coefficient can be calculated by relating to the mean square displacement of a particle, as a function of observation time, as seen in Eq. (5). Where, D is the self-diffusion coefficient and d is the dimensionality of the system.

$$MSD = \langle (x - x_0)^2 \rangle = \frac{1}{N} \sum_{n=1}^{N} [x_n(t) - x_n(0)]^2 \quad (4)$$

$$D = \frac{1}{2d} \lim_{t \to \infty} \frac{\langle (x - x_0)^2 \rangle}{t} \quad (5)$$

In order to calculate the self-diffusion coefficient, MSD trends should approach the long-time limit. The validity is confirmed by plotting the MSD vs. elapsed time on either a Cartesian scale or a log-log scale (Keffer, 2002). Figure 2.30 shows typical trends of MSD vs. elapsed time on the

two scales. As shown in Figure 2.30b, the plots have three distinct regions: 1) short observation time (collision free motion); 2) intermediate time; and 3) long-time behavior. The diffusion coefficient is calculated using the MSD obtained in the long-time limit.

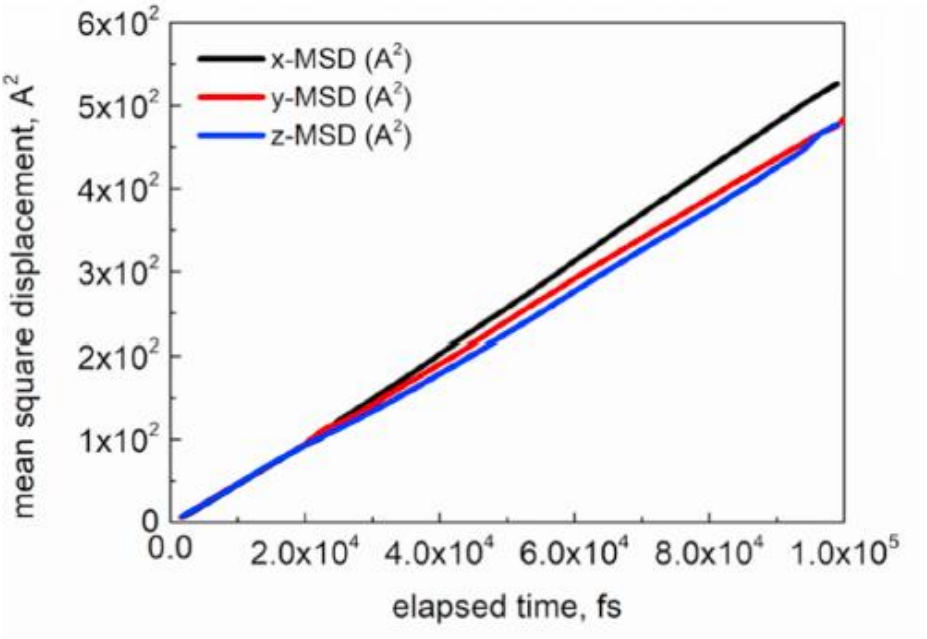

(a) Cartesian scale

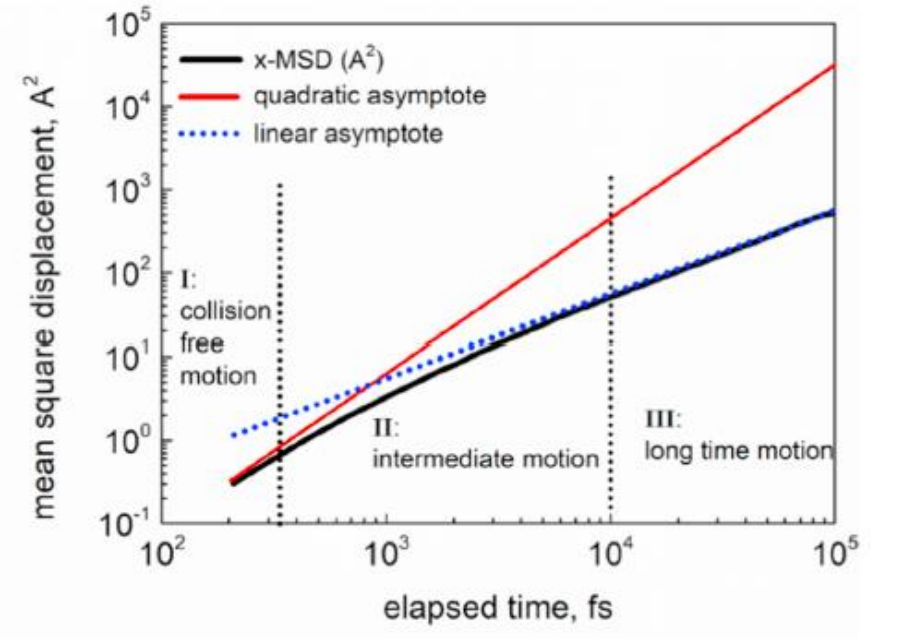

(b) Log-log scale

Figure 2.30. Mean square displacement over observation time (Keffer, 2002).

Figure 2.31 indicates observed MSD for one of the fluid molecules in the mixed-wet nanopore models. To capture valid diffusion behavior of all the fluid species, the models were simulated for an additional 4ns after equilibrium. As shown in Figure 2.31, we observe linear behavior of MSD on both the Cartesian and log-log scale. Based on the slope on the log-log plot, the self-diffusion coefficient of methane is estimated as 1.23×10^{-10} m^2/s.

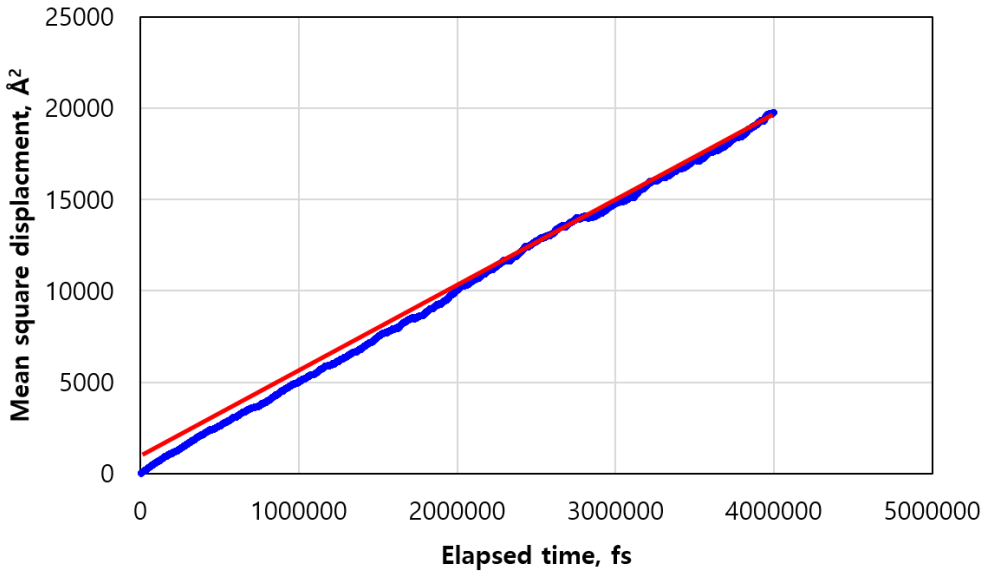

(a) Cartesian scale

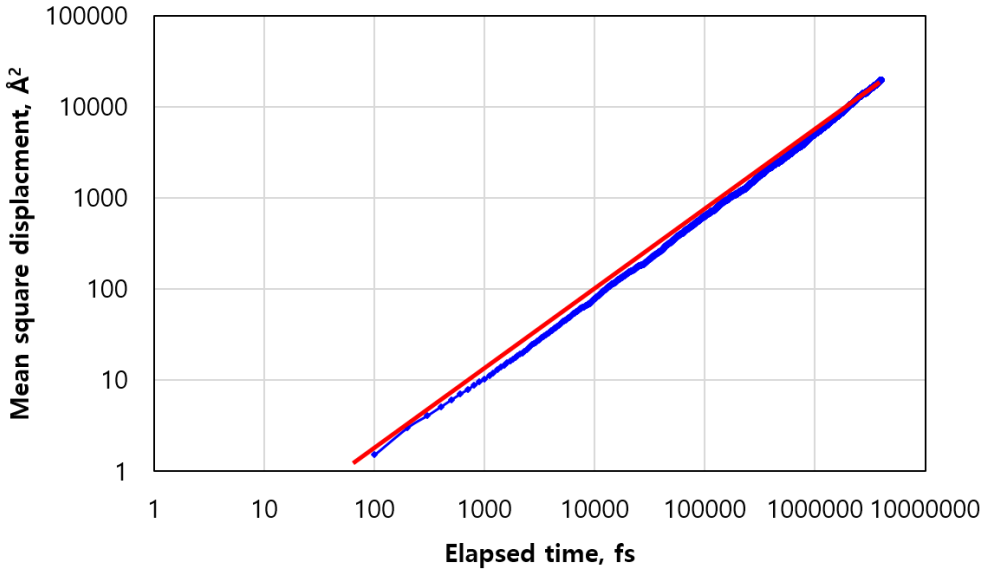

(b) Log-log scale

Figure 2.31. Estimated mean square displacement (methane). Blue scatter plots are the computed MSD from simulation results and red solid lines is fitted line for long-term behavior region. (a) is Cartesian scale and (b) is log-log scale, respectively.

2.5.2 Self-Diffusion Coefficients of Fluid Molecules in Mixed-Wet Pores

The same workflow described in the previous section was applied all fluid molecules to estimate the self-diffusivity of fluid components confined in the simulation box. Figure 2.32a shows the self-diffusion coefficients of all fluid components obtained from the computed MSD. The values obtained correlate very well with the previous analysis of molecular interactions in Section 2.5.1. For instance, the light and intermediate components have smaller interaction energies with the organic/inorganic surfaces than the heavy components and consequently have a higher mobility. Carbon dioxide also has comparably high values of the self-diffusion coefficient.

Water, on the other hand, shows a small diffusion coefficient because of the formation of water bridges or adsorption which restricts the mobility of water. In general, as water bridges form at high water saturations, we see a decrease in the self-diffusion coefficients for all hydrocarbon components indicating that the bridges are restricting fluid transport. The heavier components, however, have very limited mobility in all cases compared to the lighter and intermediate components. The asphaltene/resin fraction shows the smallest self-diffusion coefficient because of adsorption on kerogen surfaces, asphaltene aggregation with other heavy ends, and hydrogen bonding with water molecules.

Figure 2.32b presents the self-diffusion coefficients of the fluids for the simulation box with P-P clay surfaces. There are a few interesting observations showing higher diffusion coefficients for several species at higher concentrations of water. Remarkably, intermediate (propane and butane) and heavy (octane and tetradecane) components have a higher diffusion coefficient above 50% water concentration. In addition, octane and tetradecane show the highest diffusion coefficient at 60% water concentration.

These results have also been reported by Zhan et al (2020) who used MD simulation to analyze water-octane two phase flow in shale inorganic nanopores. They describe the occurrence of a stable interface between oil and water adsorbed on the inorganic surface as the water concentration is increased. This stable interface is shown to enhance the non-wetting phase flow by liquid-liquid slip. It is likely that the results in this thesis are similar to those reported by Zhan et al. (2020) and that the water-oil interface in the simulation box with P-P clay surface contributes to enhance the self-diffusivity of the intermediate components and the two heavy ends (octane and tetradecane).

Additionally, the values of self-diffusion coefficients from this study were compared with results from previous studies. Dang (2019) conducted experimental work to investigate the importance of hydrocarbon diffusion during cyclic gas injection EOR in shale reservoirs. The confinement in small pores was reported to impact the diffusion coefficients of methane and nitrogen and the coefficients varied from 100×10^{-10} m^2/s to $100{,}000 \times 10^{-10}$ m^2/s. Yang et al. (2018) analyzed diffusion of methane in quartz slit pores under various pressure and temperature conditions based on the interaction of methane with the inorganic material. Their observation showed that self-diffusion coefficients of the methane were approximately 2.6×10^{-8} (260×10^{-10}) m^2/s (4,350 psi and 140F) and 8.5×10^{-8} (850×10^{-10}) m^2/s (3,045 psia and 176F), respectively. The values from this study are 1.23×10^{-10} m^2/s (H-P clay surface) and 1.32×10^{-10} m^2/s (P-P clay surface) for methane, which corresponds to the values seen in prior studies. Perez and Devegowda (2020) also computed self-diffusion coefficients of volatile oil components and reports methane self-diffusion as 6.68×10^{-10} m^2/s which is very close to the results reported in this work. Thus, the computed self-diffusion coefficients are validated by the comparison. In this chapter, variation of self-diffusion coefficients were discussed. The observation in this thesis provide that surface

chemistry of clay minerals and water concentration could be driving mechanisms for hydrocarbon storage and flow in mixed-wet shale nanopores.

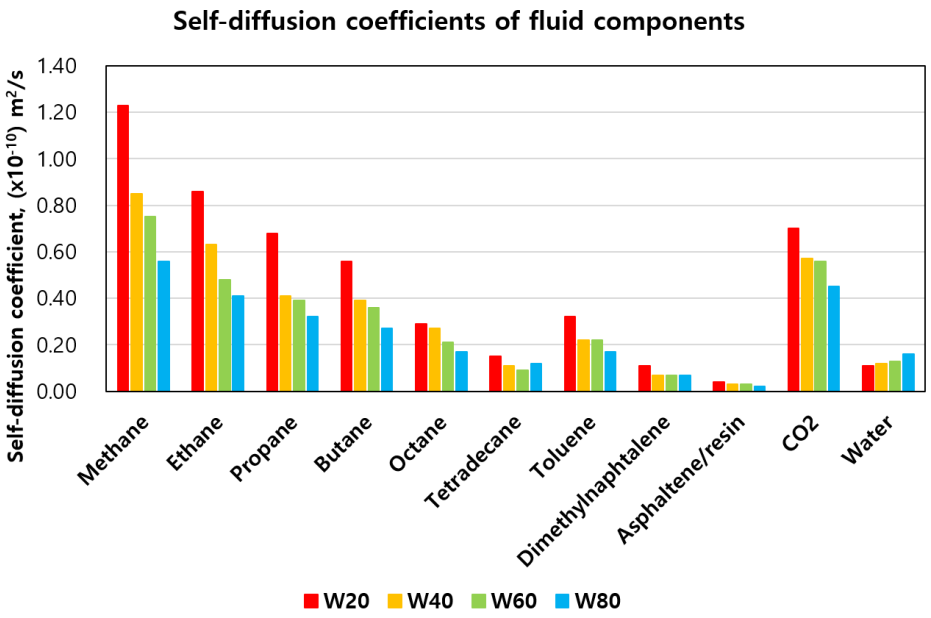

(a) Bar chart displaying self-diffusion coefficients of fluid species in the simulation box with H-P clay surfaces.

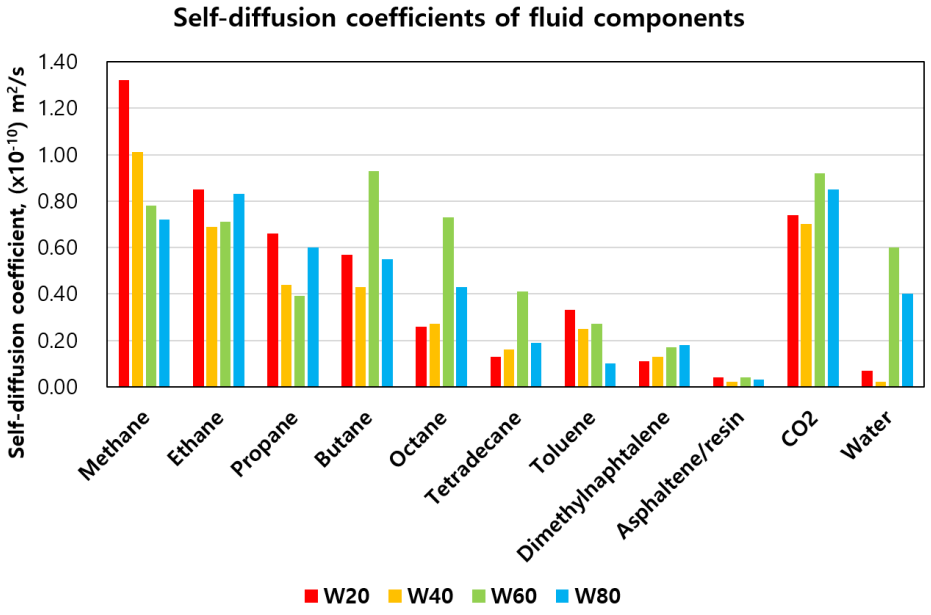

(b) Bar chart of self-diffusion coefficients for fluid species in the simulation box with P-P clay surfaces.

Figure 2.32. Self-diffusion coefficients of fluid molecules at different water concentration.

CHAPTER 3. RELATIONSHIP BETWEEN HYDRATED COMPLEXES AND FLUID DISTRIBUTION

In this chapter, I discuss the interactions of water and the asphaltene/resin fraction with clay surfaces in greater detail. The results from previous chapters demonstrate that water is typically adsorbed on to the clay surfaces but under the right conditions, can form a bridge from one surface to another. In this chapter, I will discuss the consequences of adsorption and water bridging on the distribution of other fluids.

3.1 Hydration Behavior in H-P Clay Surfaces

This section describes hydration behaviors in the simulation box with H-P clay surfaces. Hydration is a process behind the adsorption of water on clay surfaces. The hydration behavior occurs when water molecules are placed in the interlayer space of clay minerals possessing charged surfaces (Goudie, 2004; Shroder, 2013). The surface charge leads to hydrated complexes that are structures of water formed by hydrogen bonding with charged surfaces (Donaldson and Alam, 2008).

In this study, two different hydrated complexes are observed in the mixed-wet pores under study. Water is seen to form a water bridge, either from one clay surface to the other or from one clay surface to the kerogen surface. Alternatively, water exists as adsorbed layers adjacent to the clay surface. Water bridges and water adsorption occur via a specific form of intermolecular bonding, called hydrogen bonds (HB), between highly electronegative atoms and electropositive atoms (Yaseen and Mansoori, 2018).

The degree of water bridging, or adsorption largely depends on the water saturation as well as the type of the clay surface. Figures 3.1 shows the results from our simulation runs (at 0 ps, 50 ps, 250 ps and after 2 ns) with a water concentration of 20% in the simulation box with an H-P clay

surface. All the snapshots are rendered using OVITO (Stukowski 2010). There are 2 cases shown: One where all water is initially outside kerogen (Figures 3.1a and 3.1b) and one with water present within kerogen (Figures 3.1c and 3.1d). In Figures 3.1a and 3.1b, at the initial time of 0 ps, water and hydrocarbons are randomly distributed in the pores. At 50 ps, the water molecules begin to organize themselves in Figure 3.1a, forming strands that subsequently merge to form a bridge at 2ns. The bridge originates on one clay surface and ends on the kerogen surfaces. The figures also show a portion of water adsorbed on to the clay surfaces.

Figure 3.1b plots the asphaltene/resin fraction and water evolving over 2ns from an initially random configuration. At the end of the simulation, several asphaltene/resin molecules are seen to be adsorbed on the kerogen surface. More importantly, a large fraction of the asphaltene molecules form an adsorbed layer adjacent to the adsorbed water on the clay surface to the right.

With even moderate amounts of water within kerogen, the results are similar as seen in Figures 3.1c and d. However, the presence of water in kerogen promotes the growth of the water bridge from one clay surface across the simulation box to the other clay surface as seen in Figure 3.1c. The asphaltene fraction also shows affinity towards kerogen and the adsorbed water layer (Figure 3.1d) as seen previously in Figure 3.1b.

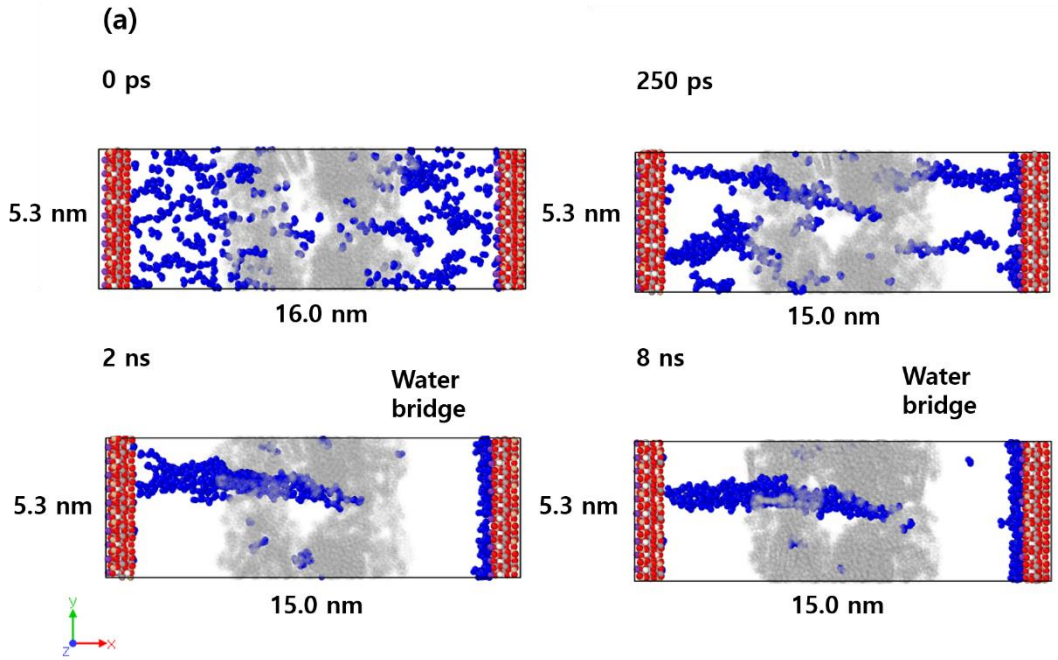
(a)
0 ps
250 ps
5.3 nm
5.3 nm
16.0 nm
15.0 nm
2 ns
8 ns
Water bridge
Water bridge
5.3 nm
5.3 nm
15.0 nm
15.0 nm

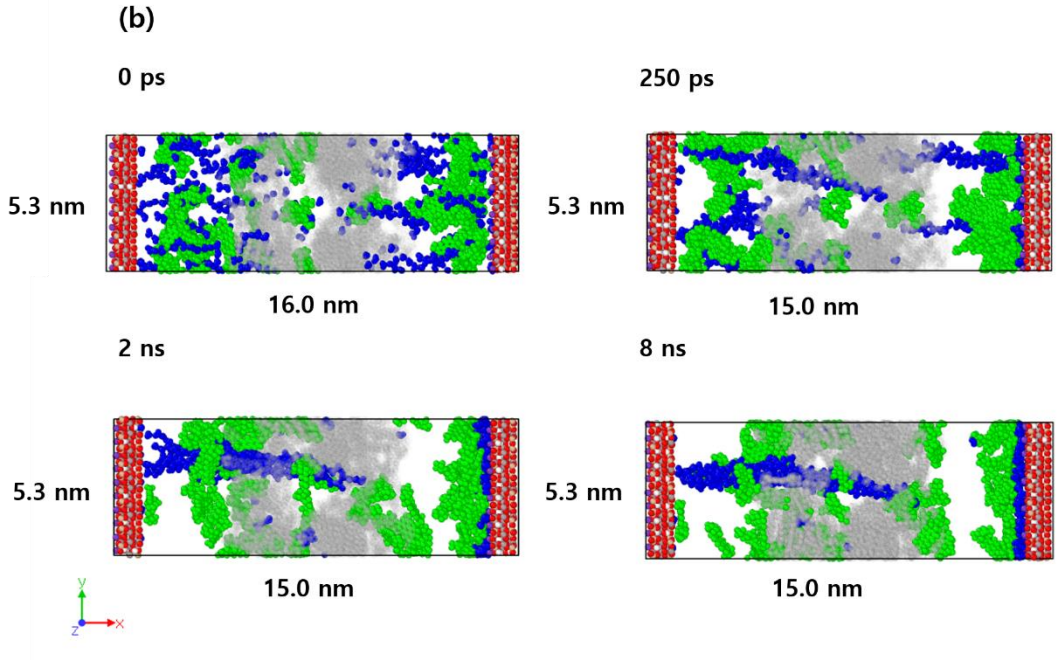
(b)
0 ps
250 ps
5.3 nm
5.3 nm
16.0 nm
15.0 nm
2 ns
8 ns
5.3 nm
5.3 nm
15.0 nm
15.0 nm

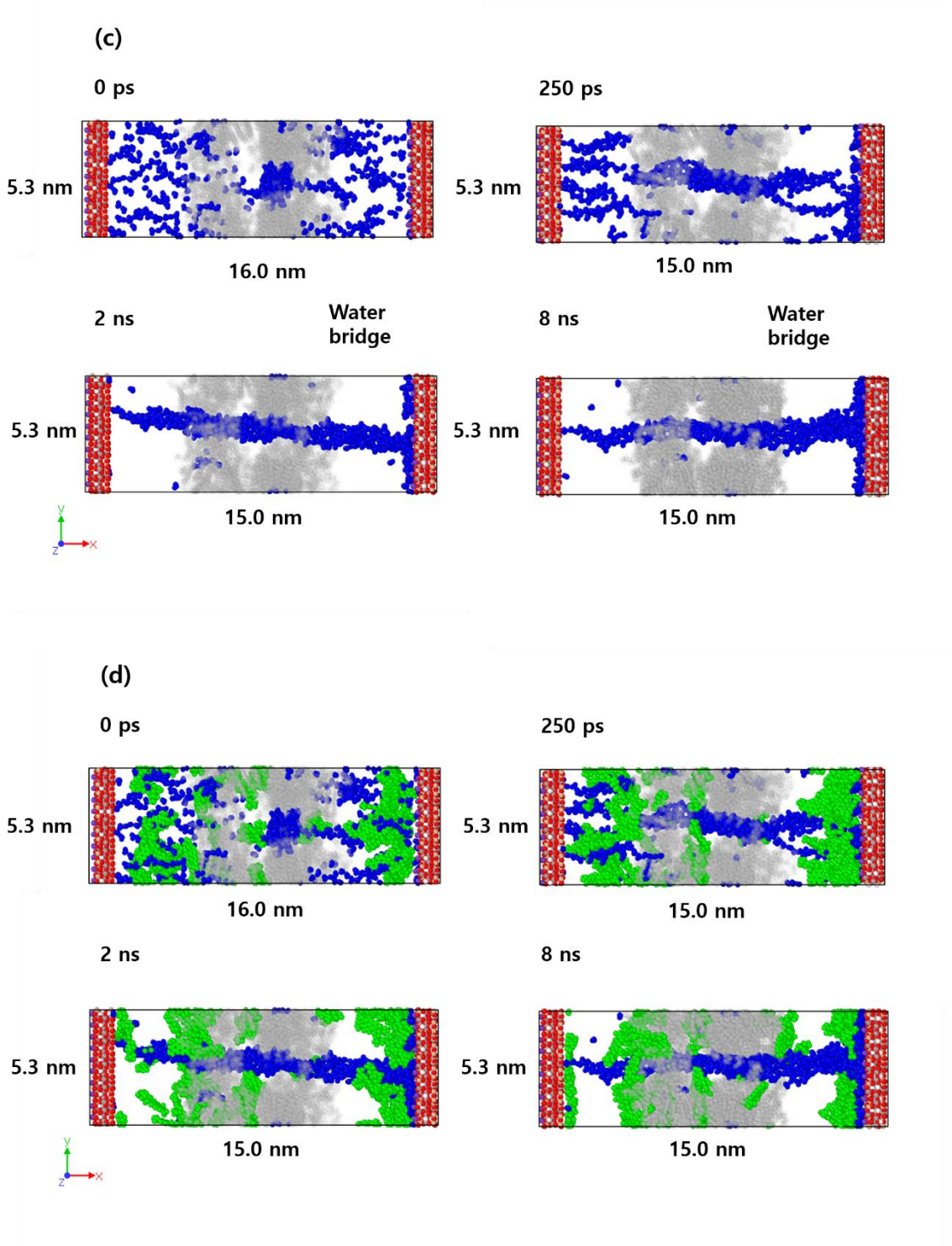

Figure 3.1. Distribution of asphaltene/resin and water molecules in the simulation box with H-P pores at 20% of water concentration. (a) shows the formation of a water bridge over time in the case where no water is present in kerogen. (b) displays both water and asphaltene/resin fraction

with some adsorption of asphaltene/resin on kerogen and a few asphaltene/resin molecules adjacent to the adsorbed water film on clay surface. (c) shows the formation of a water bridge in the presence of water in kerogen. (d) indicates both water and asphaltene/resin distribution with asphaltene/resin adsorption on kerogen and a few asphaltene/resin molecules attracted to the adsorbed water film. The color code is assigned as follows: water (blue), asphaltene/resins (green), kerogen (gray), and illite (other colors).

An interesting observation in these results is the affinity of the asphaltene/resin fraction towards water (Figures 3.1b and d). This is because of the physical bonds that develop between the relatively polar constituents in the asphaltene/resin fraction molecules and water molecules. This is also shown in enlarged detail in Figure 3.2. This was also reported in Chapter 2 in Figure 2.9.

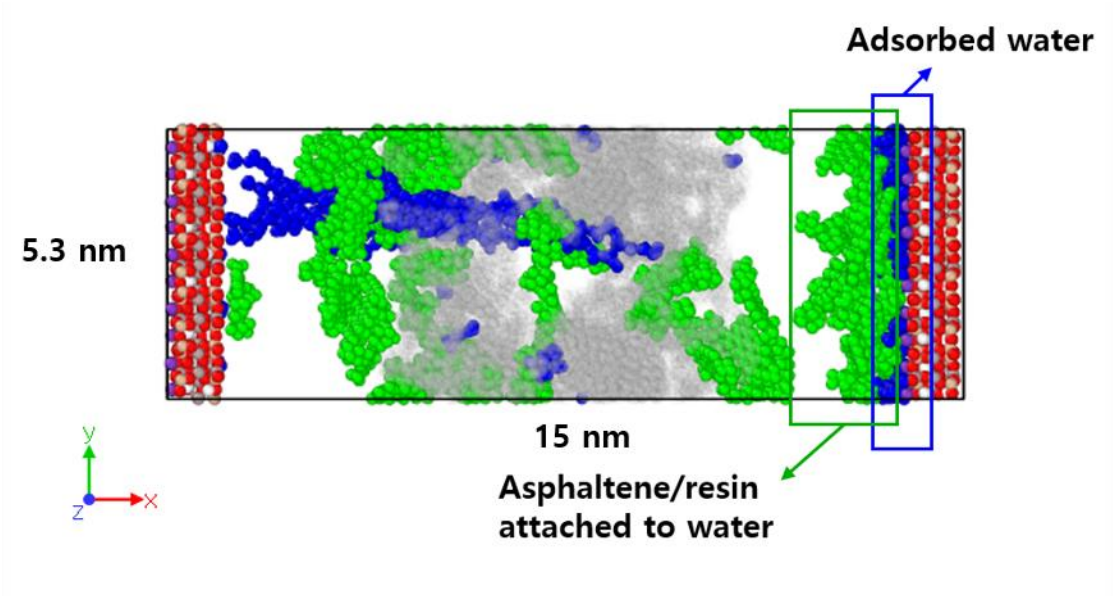

Figure 3.2. Attraction of asphaltene/resin molecules to adsorbed water layer (20% of water concentration in the H-P pores). The color code is assigned as follows: water (blue), asphaltene/resins (green), kerogen (gray), and illite (other colors).

This is a very significant observation in this thesis. The prevalent notion of pores with organic and inorganic surfaces is that the organic surface is largely hydrophobic while the inorganic surface is water-wetting. With the results presented here, I show that if there is an appreciable asphaltene fraction, we may have asphaltenes adjacent to the adsorbed water. Revisiting Figure 3.2, the final results show a pore with kerogen and the adsorbed asphaltene on one side and asphaltene on the

adsorbed water attached to the clay surface on the other side. This implies that the pore space between the clay and kerogen surfaces may have a higher degree of hydrophobicity (more oil-wet) than what the pore surface chemistry indicates. Although this affinity of asphaltene molecules towards water is surprising, there have been a few other studies documenting this effect (Yaseen and Mansoori, 2017 and 2018; Joonaki et al., 2019). However, my study is the first to show this in a comprehensive model that include realistic hydrocarbon mixtures and hydrophobic/hydrophilic pore surfaces analogous to those present in shales.

Figures 3.3 shows formation of water bridges at 40% of water concentrations. As seen in Figures 3.3a and b, the water molecules are arranged randomly at the start of the simulation. As the simulation proceeds, we observe the formation of small water droplets or water chains. Eventually, the water chains come together to form a water bridge from one end to the other side of pore. This is different from the result shown for 20% water concentration and a possible reason might be the stronger water-water interactions at high concentrations compared to the water-asphaltene/resin interaction (Mani et al., 2015). The higher water concentrations result in wider water bridges across the organic pore body as seen in Figure 3.3a and c. We still observe the adsorption of the asphaltene/resin fraction on to kerogen in Figures 3.3b and d and this effect was previously seen in the case of 20% water concentration. A smaller portion of the asphaltene/resin fraction is also either dispersed around the water bridge or attracted to the adsorbed water layer.

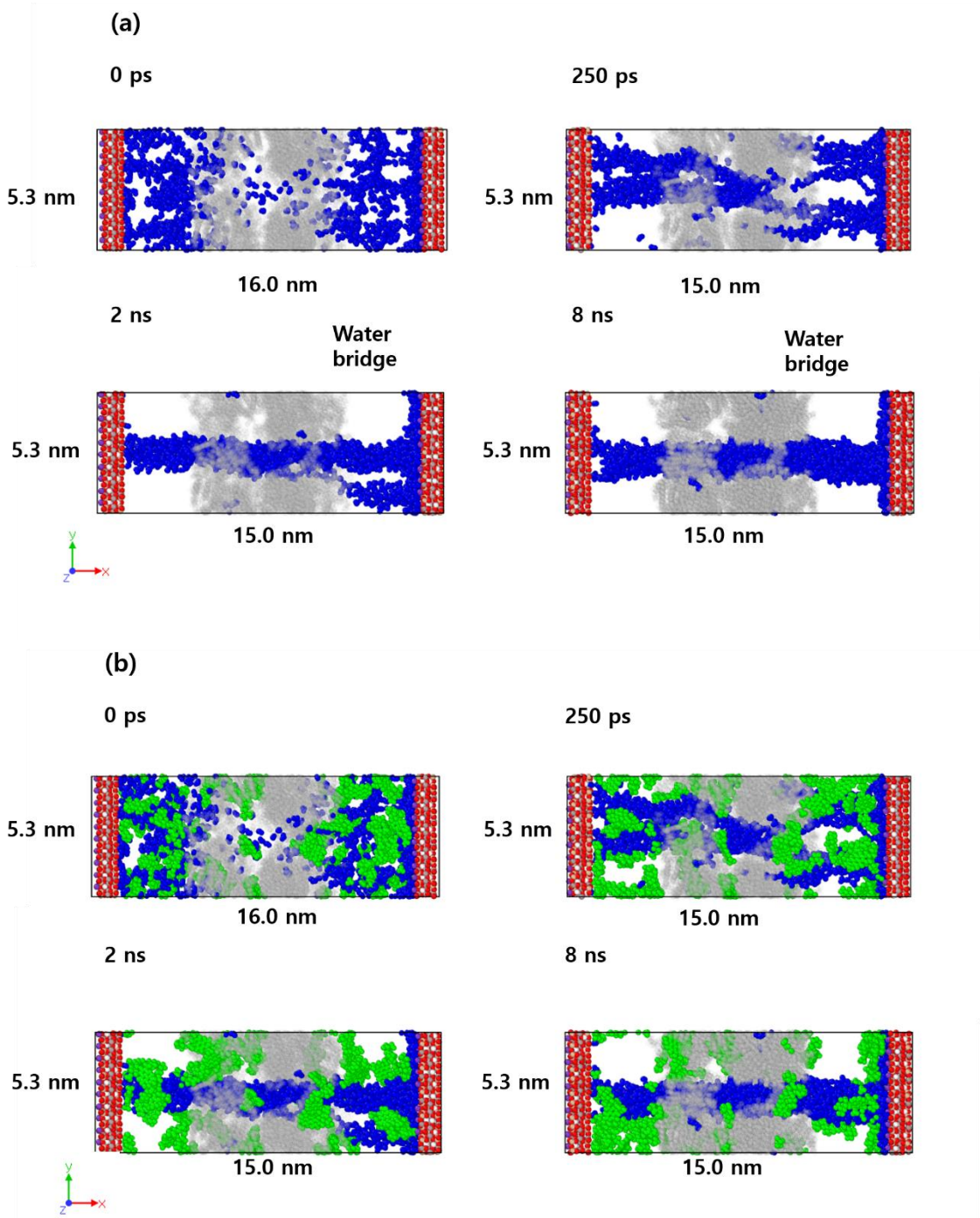
(a)
0 ps
250 ps
5.3 nm
5.3 nm
16.0 nm
15.0 nm
2 ns
8 ns
Water bridge
Water bridge
5.3 nm
5.3 nm
15.0 nm
15.0 nm
(b)
0 ps
250 ps
5.3 nm
5.3 nm
16.0 nm
15.0 nm
2 ns
8 ns
5.3 nm
5.3 nm
15.0 nm
15.0 nm

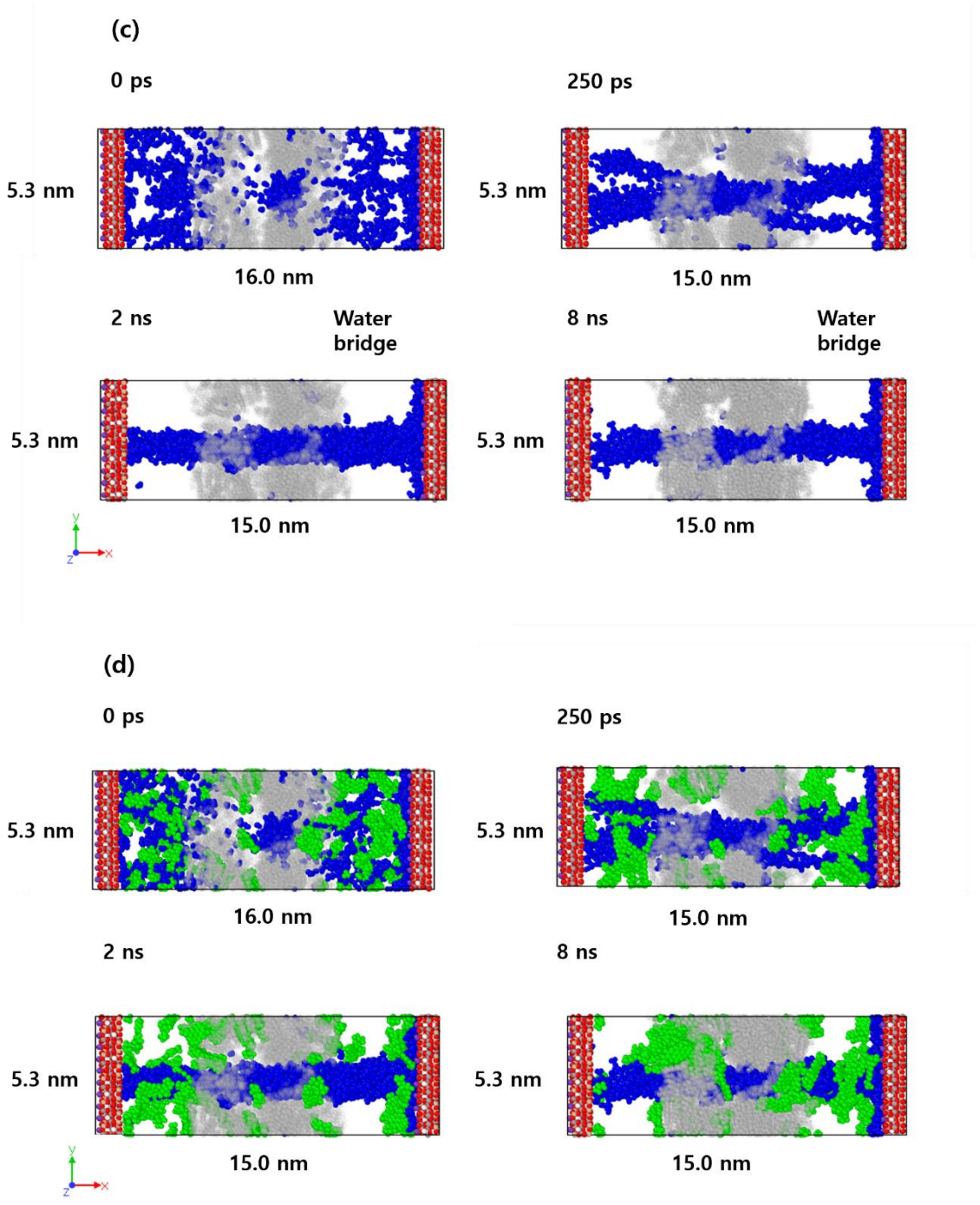

Figure 3.3. Distribution of asphaltene/resin and water molecules in the simulation box with H-P pores at 40% of water concentration. (a) shows the formation of a water bridge over time in the case where no water is present in kerogen. (b) displays both water and asphaltene/resin fraction with some adsorption of asphaltene/resin on kerogen and a few asphaltene/resin molecules

adjacent to the adsorbed water film on clay surface. (c) shows the formation of a water bridge in the presence of water in kerogen. (d) indicates both water and asphaltene/resin distribution with asphaltene/resin adsorption on kerogen and a few asphaltene/resin molecules attracted to the adsorbed water film. The color code is assigned as follows: water (blue), asphaltene/resins (green), kerogen (gray), and illite (other colors).

At 60% water concentration, the snapshots as shown in Figure 3.4 present a zone dominated by water in between kerogen and the clay surfaces. In Figure 3.4a, we observe the formation of a water bridge again wider than those observed at lower water concentrations. Figure 3.4b displays that asphaltene/resin-water interaction is limited. This is simply because of the reduction in the number of hydrocarbon molecules as the concentration of water increases.

The simulation results with some initial water in kerogen (Figures 3.4a and b) are similar to those with the absence of water in kerogen pores (Figures 3.4c and d) because the water concentration is sufficiently high to generate a water bridge connecting the two clay surfaces. Figure 3.5 presents spatial distribution of water and asphaltene/resin molecules at 80% of water concentration. The result is very similar to the snapshots at 60% water concentration. This study therefore underscores the importance of hydrogen bonding mechanisms (water-water and asphaltene/resin-water interactions) in mixed-wet pores and its relation to water concentrations.

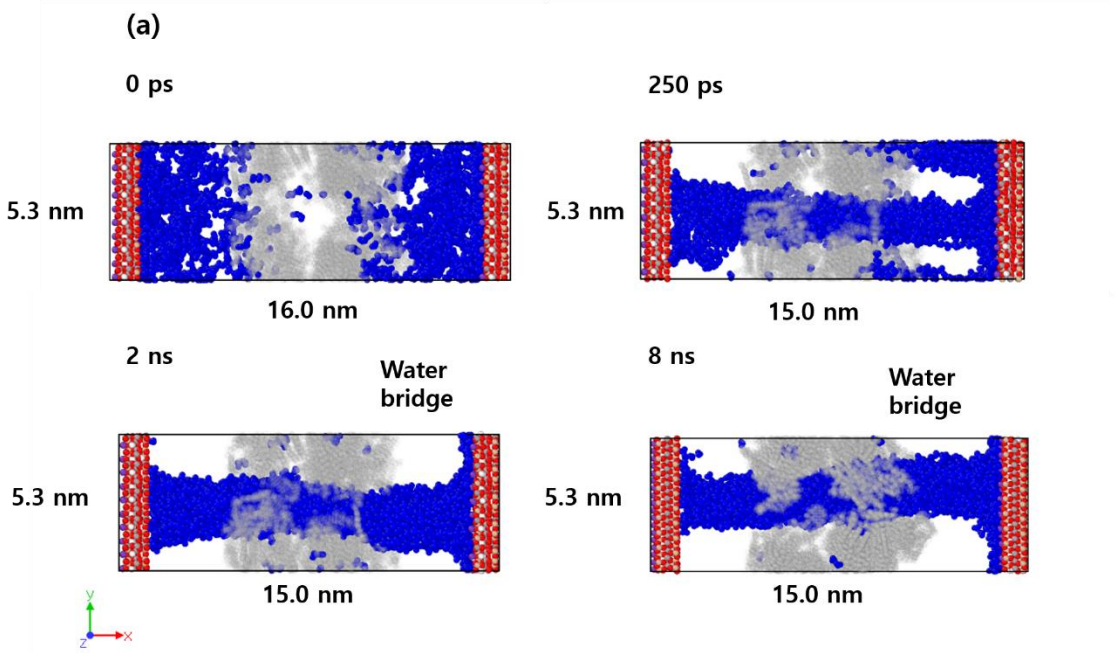
(a)
0 ps
250 ps
5.3 nm
16.0 nm
5.3 nm
15.0 nm
2 ns
Water bridge
8 ns
Water bridge
5.3 nm
15.0 nm
5.3 nm
15.0 nm

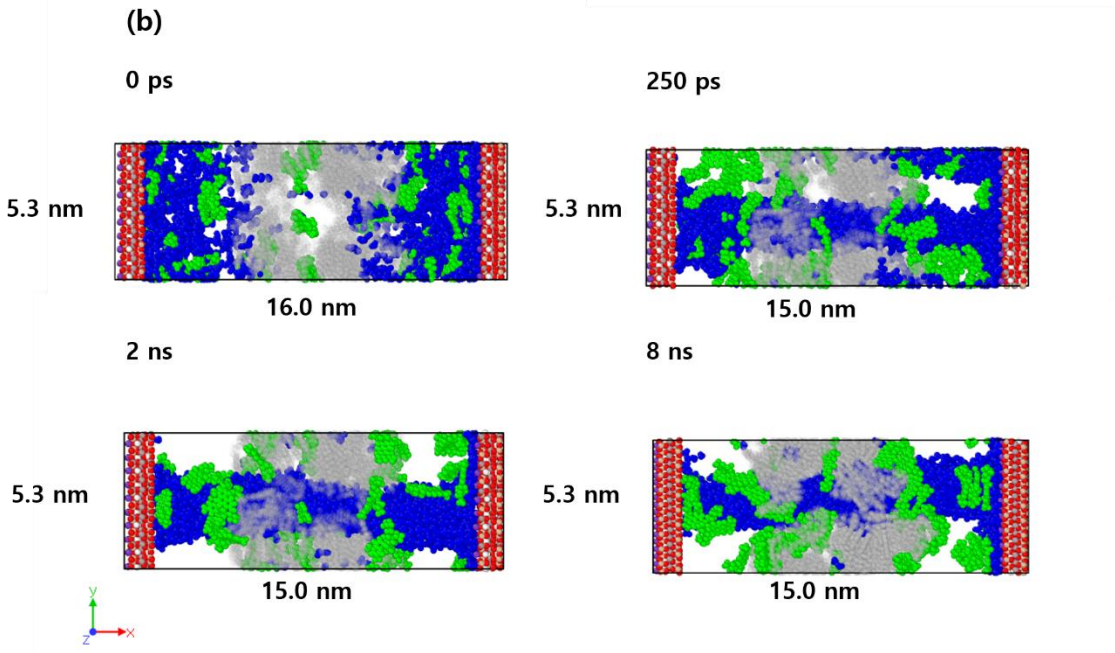
(b)
0 ps
250 ps
5.3 nm
16.0 nm
5.3 nm
15.0 nm
2 ns
8 ns
5.3 nm
15.0 nm
5.3 nm
15.0 nm

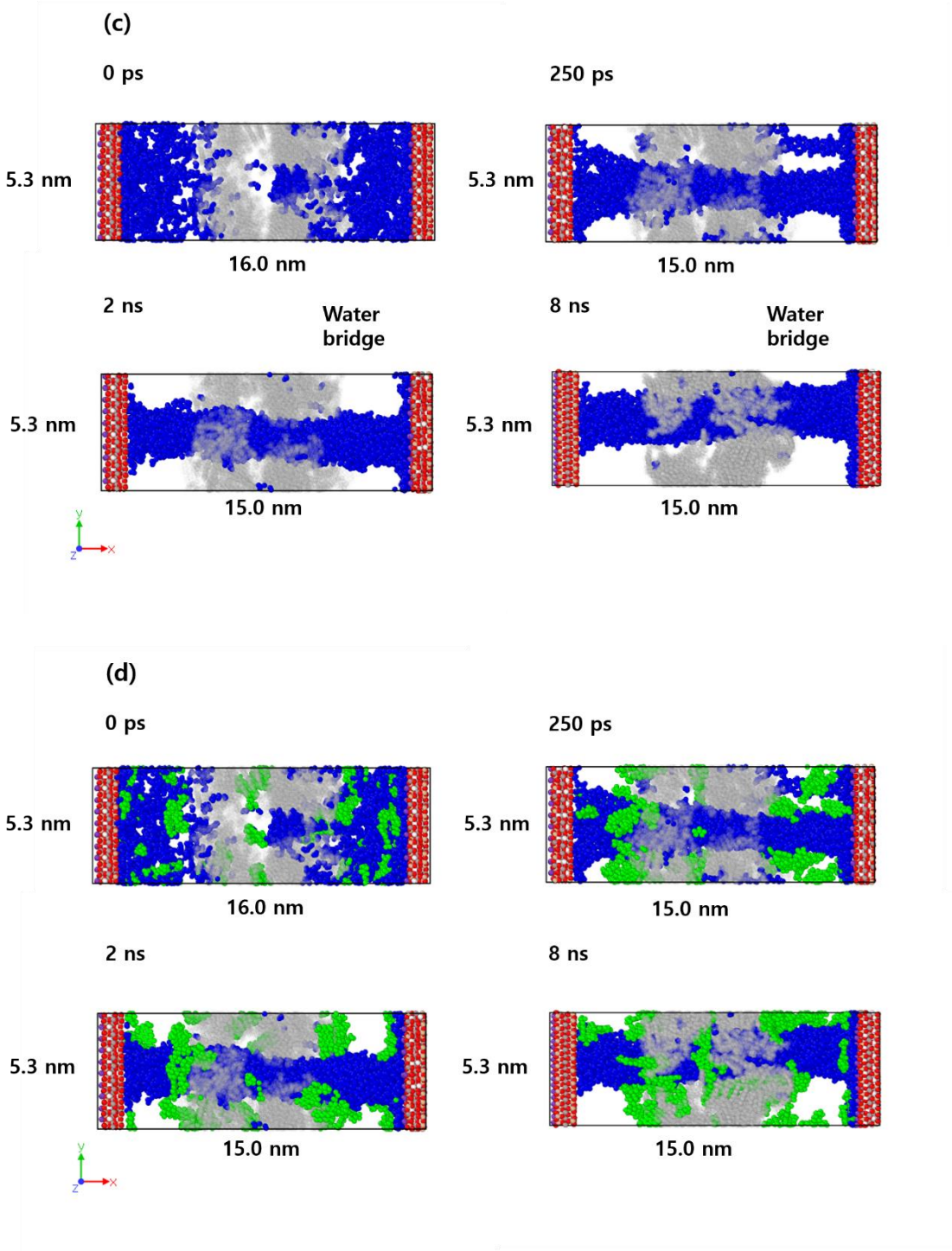

Figure 3.4. Distribution of asphaltene/resin and water molecules in the simulation box with H-P pores at 60% of water concentration. (a) shows the formation of a water bridge over time in the case where no water is present in kerogen. (b) shows the asphaltene/resin fraction predominantly

adsorbed on kerogen with no initial water in kerogen. (c) shows the formation of a water bridge in the presence of water in kerogen. (d) shows the asphaltene/resin fraction predominantly adsorbed on kerogen with some initial water in kerogen. The color code is assigned as follows: water (blue), asphaltene/resins (green), kerogen (gray), and illite (other colors).

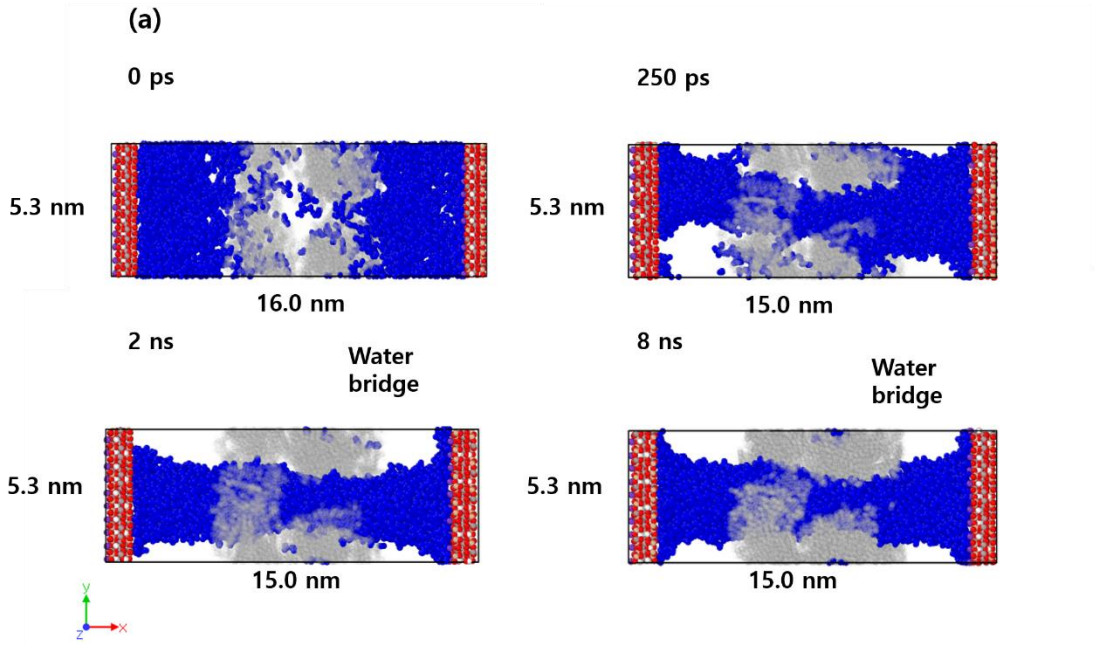
(a)
0 ps
250 ps
5.3 nm
5.3 nm
16.0 nm
15.0 nm
2 ns
8 ns
Water bridge
Water bridge
5.3 nm
5.3 nm
15.0 nm
15.0 nm

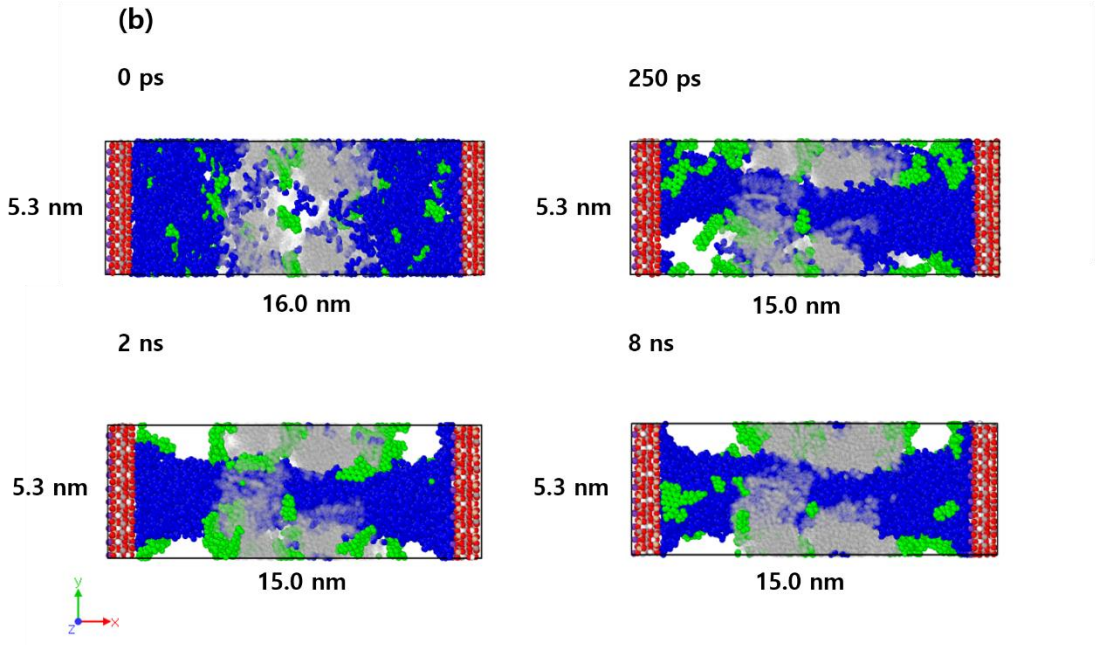
(b)
0 ps
250 ps
5.3 nm
5.3 nm
16.0 nm
15.0 nm
2 ns
8 ns
5.3 nm
5.3 nm
15.0 nm
15.0 nm

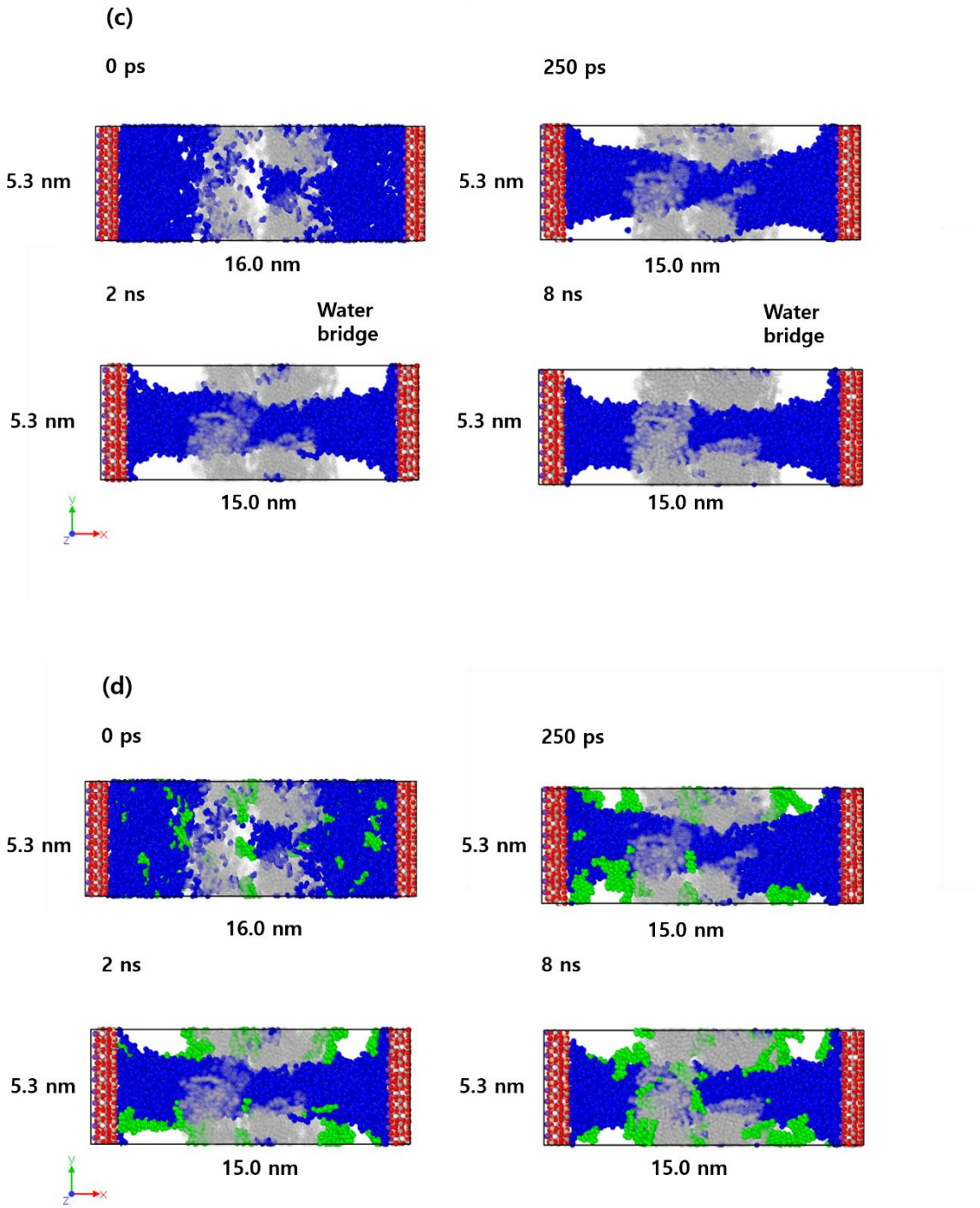

Figure 3.5. Distribution of asphaltene/resin and water molecules in the simulation box with H-P pores at 80% of water concentration. (a) shows the formation of a water bridge over time in the case where no water is present in kerogen. (b) shows the asphaltene/resin fraction predominantly

adsorbed on kerogen with no initial water in kerogen. (c) shows the formation of a water bridge in the presence of water in kerogen. (d) shows the asphaltene/resin fraction predominantly adsorbed on kerogen with some initial water in kerogen. The color code is assigned as follows: water (blue), asphaltene/resins (green), kerogen (gray), and illite (other colors).

3.2 Hydration Behavior in P-P Clay Surfaces

I also investigate the hydration behavior in the simulation box with P-P clay surfaces Figures 3.6 to 3.9 displays the simulation results with different water concentrations of 20%, 40%, 60% and 80% at different time steps (0 ps, 50 ps, 250 ps and after 2 ns) and for 2 different cases: for no initial water within kerogen and for some initial water present within kerogen.

As shown in Figure 3.6 for 20% water concentration, hydrogen bonding drives the interactions between asphaltene/resin fraction and water with the asphaltene/resin fraction residing adjacent to the water film adsorbed on to the clay surfaces. This behavior is similar to what was observed for the H-P surfaces in the previous section. However, in comparison to the water-bridging seen with H-P surfaces, interaction between the water molecules leads to the formation of water droplets around the organic pore surfaces.

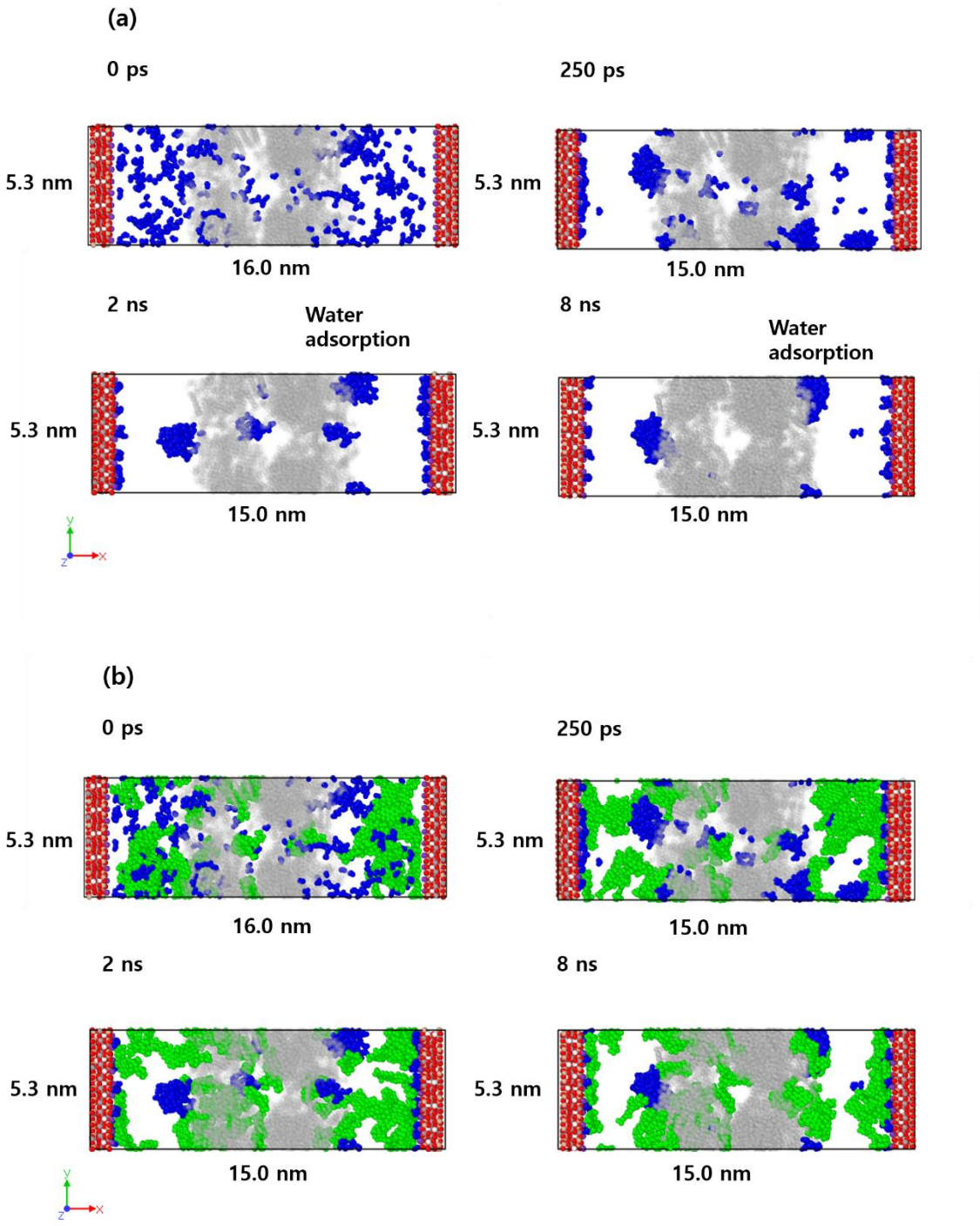
(a)
0 ps
250 ps
5.3 nm
16.0 nm
5.3 nm
15.0 nm
2 ns
Water adsorption
8 ns
Water adsorption
5.3 nm
15.0 nm
5.3 nm
15.0 nm
(b)
0 ps
250 ps
5.3 nm
16.0 nm
5.3 nm
15.0 nm
2 ns
8 ns
5.3 nm
15.0 nm
5.3 nm
15.0 nm

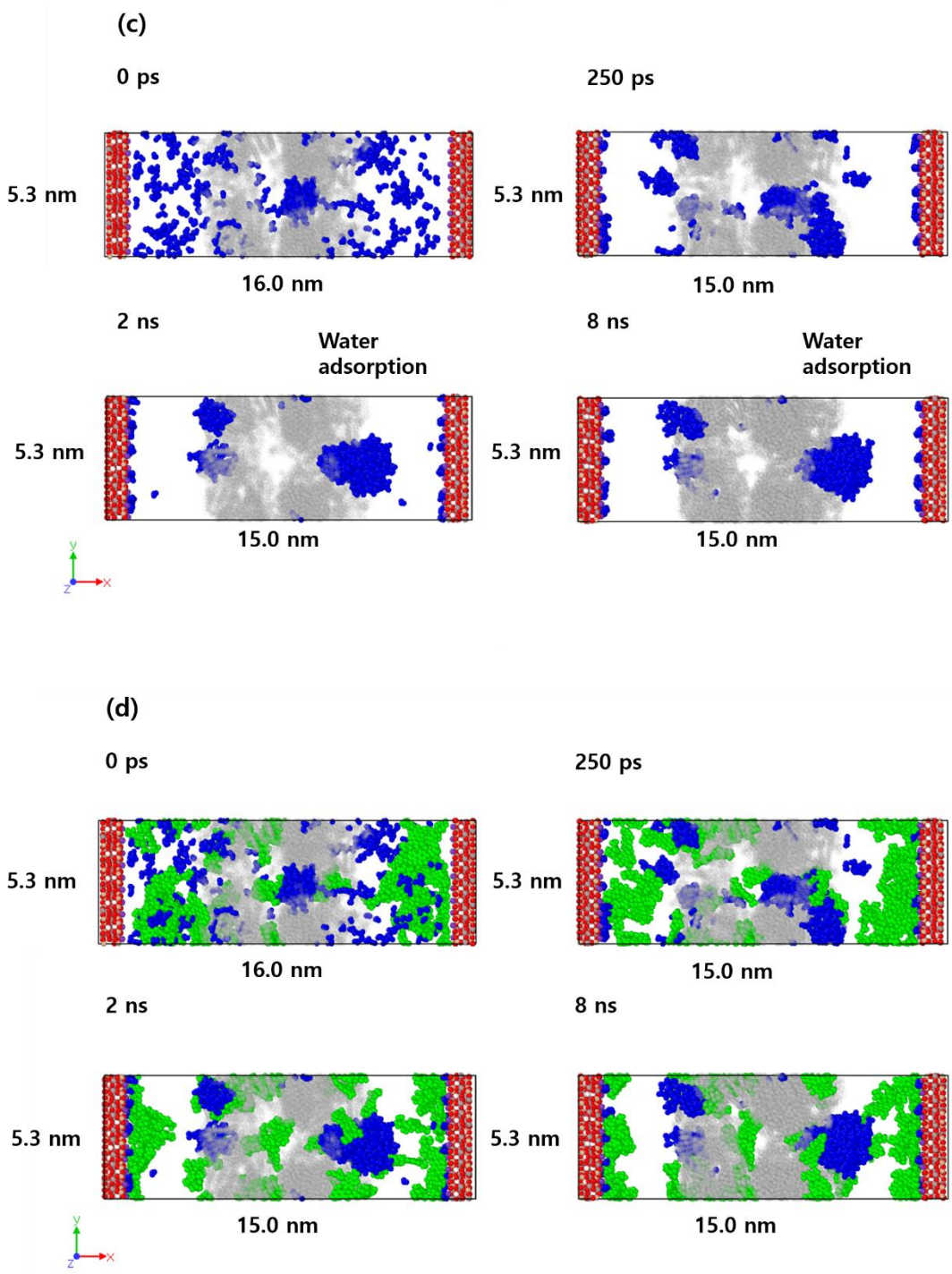

Figure 3.6. Distribution of asphaltene/resin and water molecules in the simulation box with P-P pores at 20% of water concentration. (a) shows the formation of layers of adsorbed water over time in the case where no water is present in kerogen. (b) shows some adsorption of the

asphaltene/resin fraction on kerogen and a few asphaltene/resin molecules adjacent to the water adsorbed on clay surface with no initial water in kerogen. (c) shows the adsorption of water where water is initially present in kerogen. (d) displays adsorption of the asphaltene/resin adsorption on kerogen and a few asphaltene/resin molecules adjacent to the adsorbed water when water is initially present in kerogen. The color code is assigned as follows: water (blue), asphaltene/resins (green), kerogen (gray), and illite (other colors).

The results for 40% water concentration in the simulation box with P-P clay surfaces (Figure 3.7), show similar behavior as that for 20% water concentration. Figures 3.4a shows formation of a water film on the left clay surface and moderate adsorption on the right with a few water droplets in the simulation box. As shown in Figure 3.4b, asphaltene-water molecular interaction leads to attraction of the asphaltene/resin molecules to the adsorbed water layer on clay surfaces by hydrogen bonding. In the presence of water within kerogen (Figures 3.4c and d), water is seen to be adsorbed only with a few water droplets. The asphaltene/resin fraction behave similarly between Figures 3.4b and 3.4d.

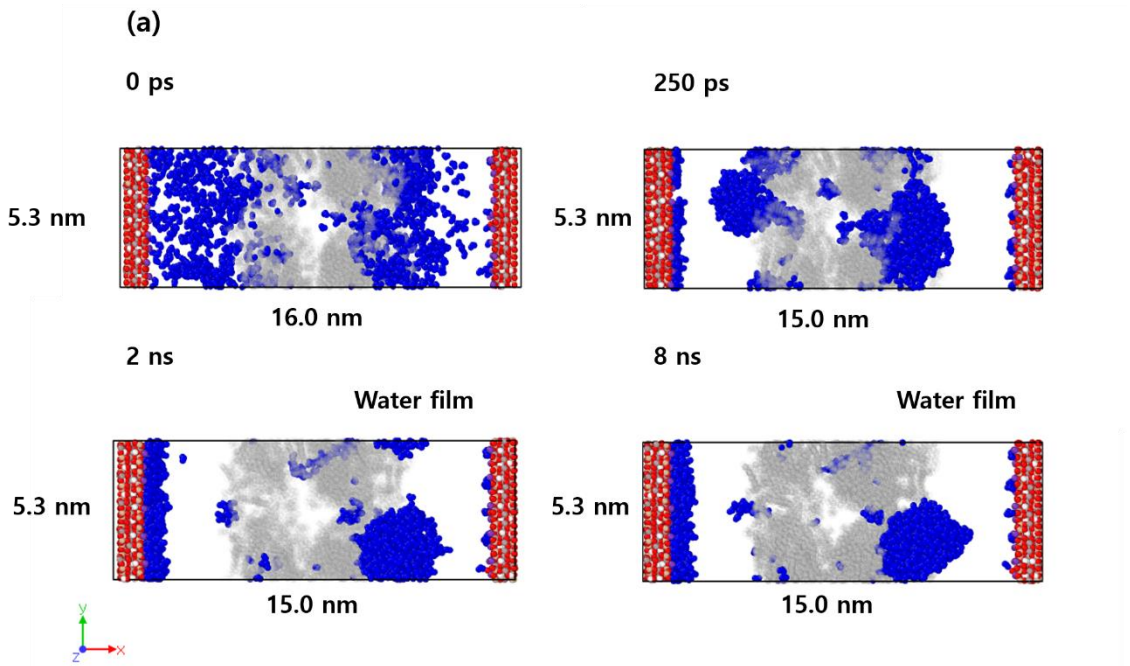
(a)
0 ps
250 ps
5.3 nm
16.0 nm
5.3 nm
15.0 nm
2 ns
8 ns
Water film
Water film
5.3 nm
15.0 nm
5.3 nm
15.0 nm
y
z
x

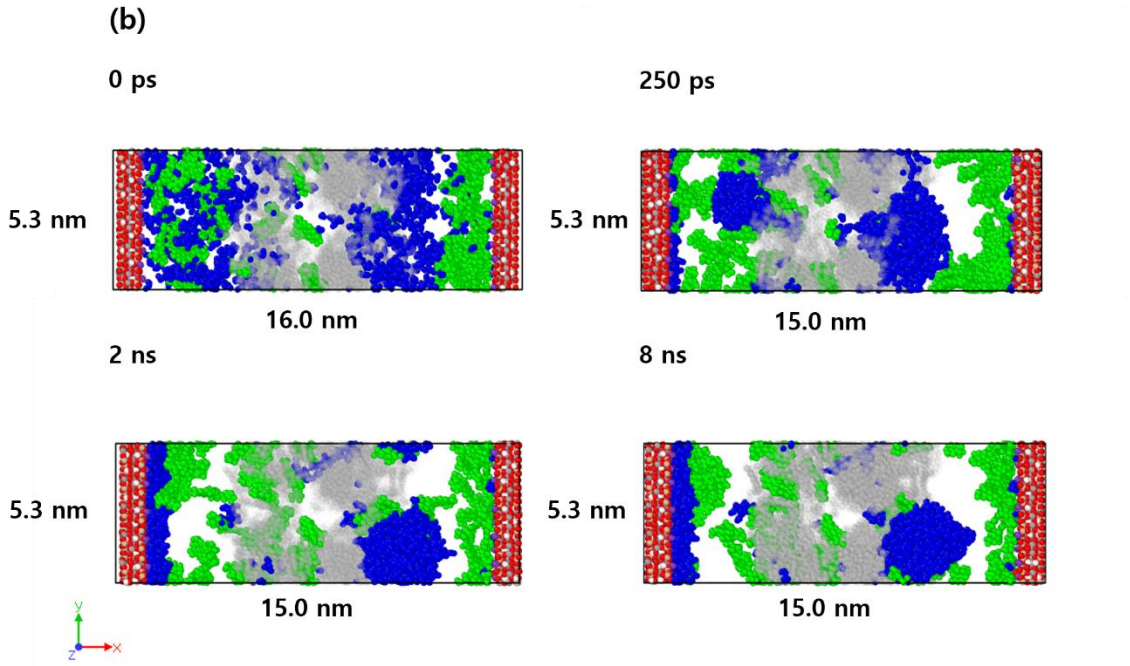
(b)
0 ps
250 ps
5.3 nm
16.0 nm
5.3 nm
15.0 nm
2 ns
8 ns
5.3 nm
15.0 nm
5.3 nm
15.0 nm
y
z
x

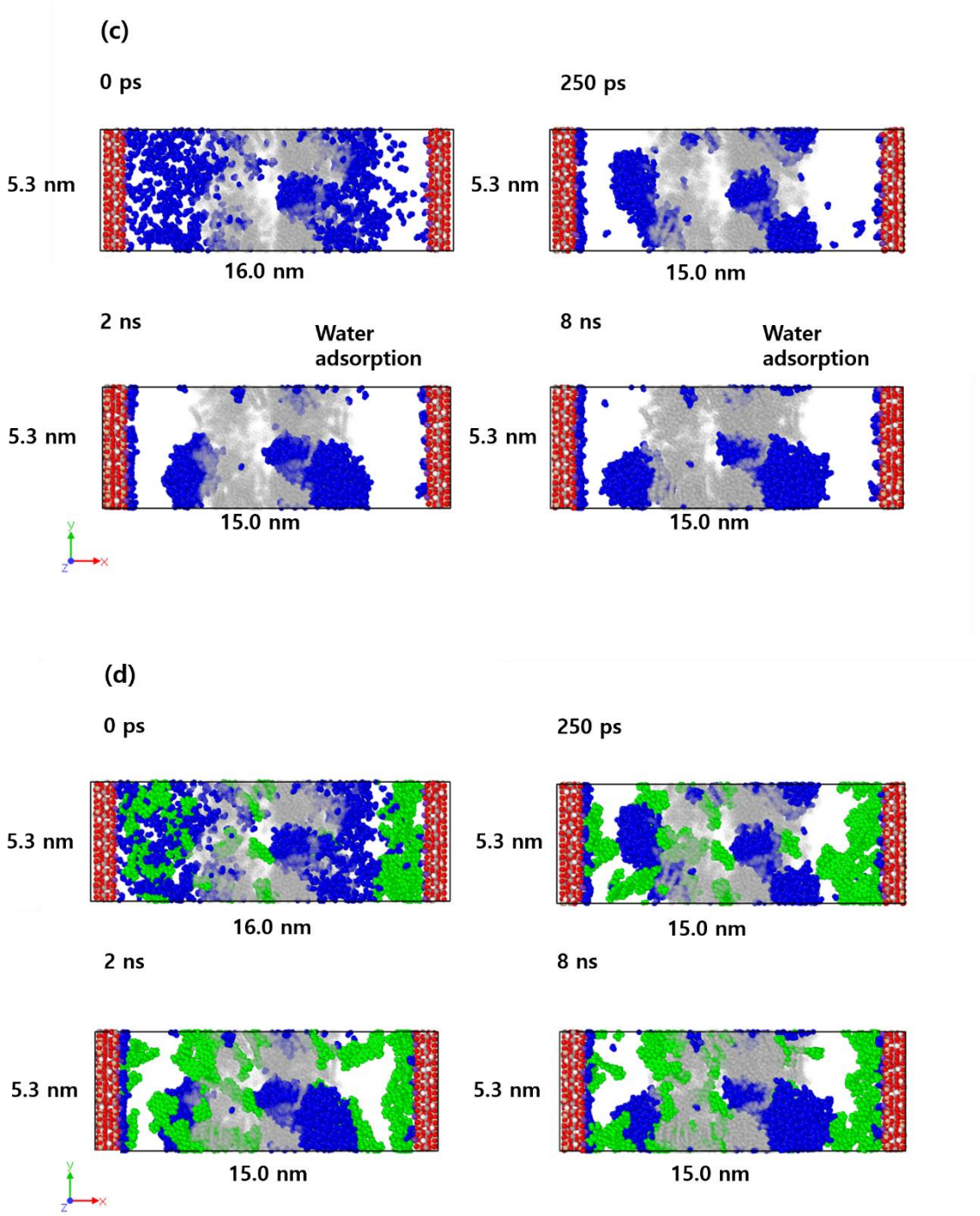

Figure 3.7. Distribution of asphaltene/resin and water molecules in the simulation box with P-P pores at 40% of water concentration. (a) shows the formation of adsorbed water layers over time in the case where no water is present in kerogen. (b) shows some adsorption of the

asphaltene/resin fraction on kerogen and a few asphaltene/resin molecules adjacent to the water adsorbed on clay surface with no initial water in kerogen. (c) shows the adsorption of water where water is initially present in kerogen. (d) displays adsorption of the asphaltene/resin adsorption on kerogen and a few asphaltene/resin molecules adjacent to the adsorbed water when water is initially present in kerogen. The color code is assigned as follows: water (blue), asphaltene/resins (green), kerogen (gray), and illite (other colors).

At above 50% water concentration (Figures 3.8 and 3.9), strong hydration results in the formation of thicker water films on both clay surfaces. In the P-P clay surface, the hydrophilicity of clay surfaces is enhanced by the strong hydration of the water molecules. The highly water-wet surfaces also limit access of asphaltene/resin molecules to the clay surfaces and eventually most of the asphaltene/resin molecules are adsorbed onto an organic surface. I observe a similar result with H-P clay surfaces (as seen in Figures 3.4 and 3.5). When the concentration of water goes beyond 50-60%, water shows a strong affinity to the clay surfaces and to each other. The asphaltene fraction resides entirely on the kerogen surface. Consequently, at high water saturations, I see a higher degree of pure mixed-wet behavior. At lower water saturations (<50%), the degree of mixed-wet characteristics is reduced.

Through the observation of water and the asphaltene/resin fraction in the simulation box with different surface chemistries of clay minerals, I propose that hydrogen bonding can be driving force to wettability alteration in mixed-wet shale pores. The charge distribution of clay minerals influences formation of hydrated complexes and accordingly heavy hydrocarbons can be adsorbed onto clay surfaces or dispersed in mixed-wet nanopores. Therefore, the results in this chapter show that the distribution of polar hydrocarbons is significantly impacted when in mixed-wet pores in the presence of an aqueous phase. In the next chapter, I will extend these studies by considering brine at various salinity levels.

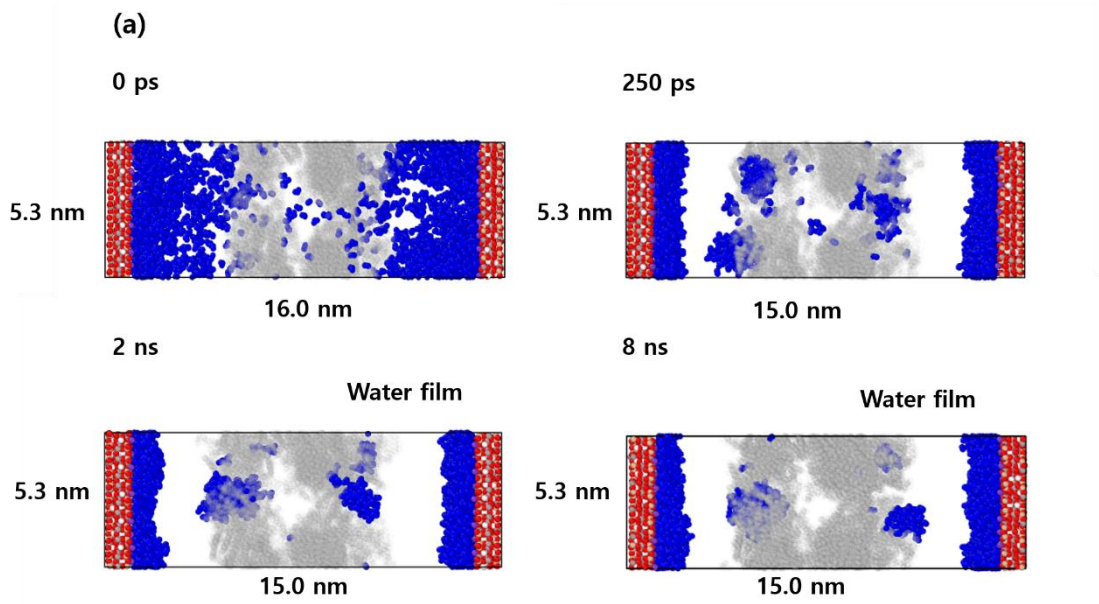
(a)
0 ps
250 ps
5.3 nm
16.0 nm
5.3 nm
15.0 nm
2 ps
8 ps
Water film
Water film
5.3 nm
15.0 nm
5.3 nm
15.0 nm

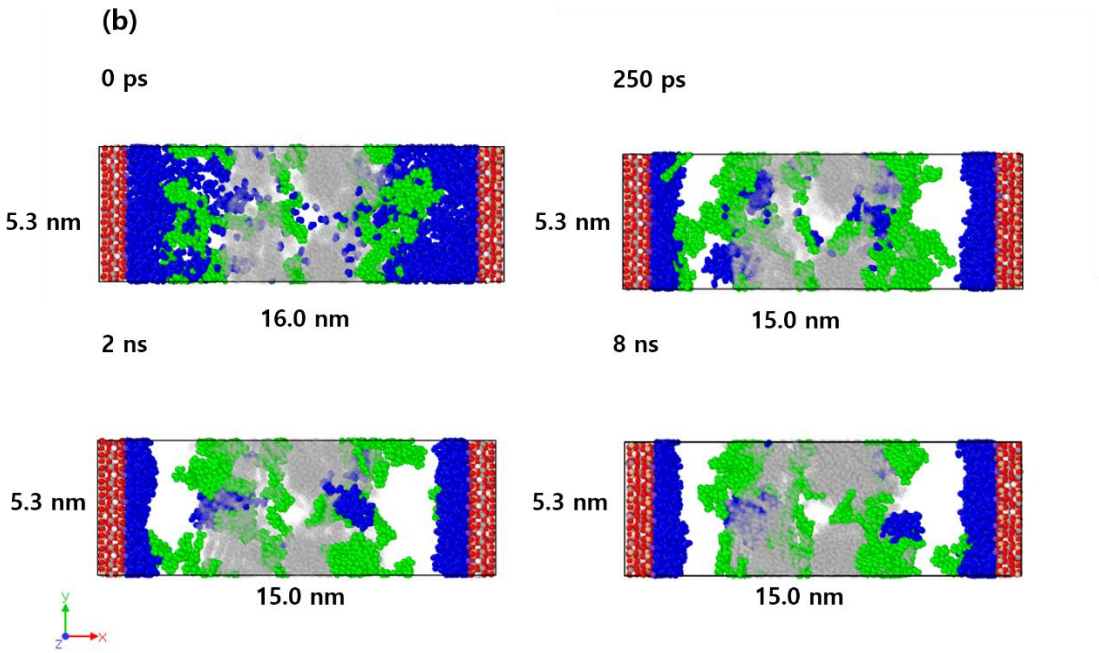
(b)
0 ps
250 ps
5.3 nm
16.0 nm
5.3 nm
15.0 nm
2 ps
8 ps
5.3 nm
15.0 nm
5.3 nm
15.0 nm
y
z
x

\

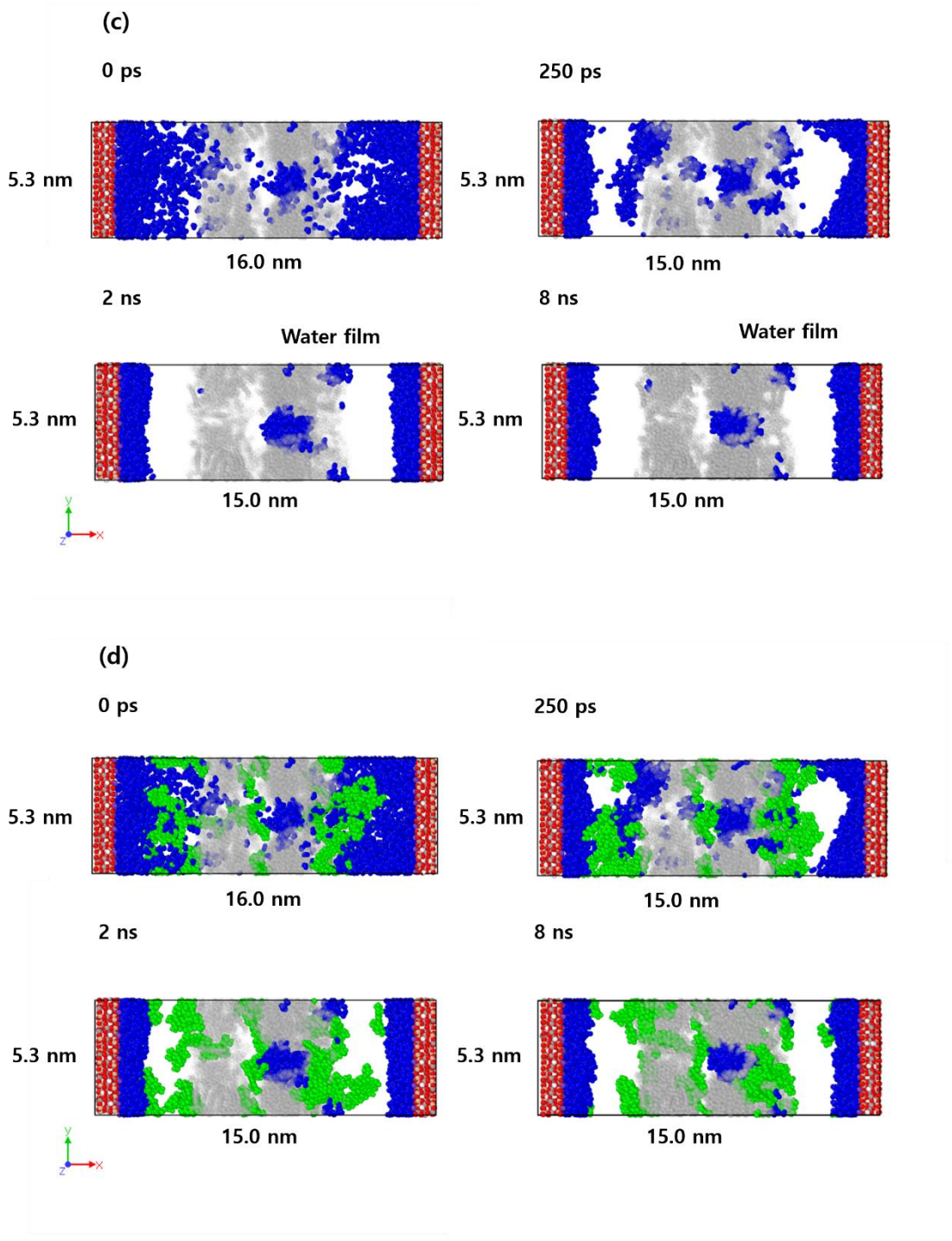

Figure 3.8. Distribution of asphaltene/resin and water molecules in the simulation box with P-P pores at 60% of water concentration. (a) shows the formation of water films over time in the case where no water is present in kerogen. (b) shows the asphaltene/resin fraction predominantly

adsorbed on kerogen with no initial water in kerogen. (c) shows the formation of water films in the presence of water in kerogen. (d) shows the asphaltene/resin fraction predominantly adsorbed on kerogen with some initial water in kerogen. The color code is assigned as follows: water (blue), asphaltene/resins (green), kerogen (gray), and illite (other colors).

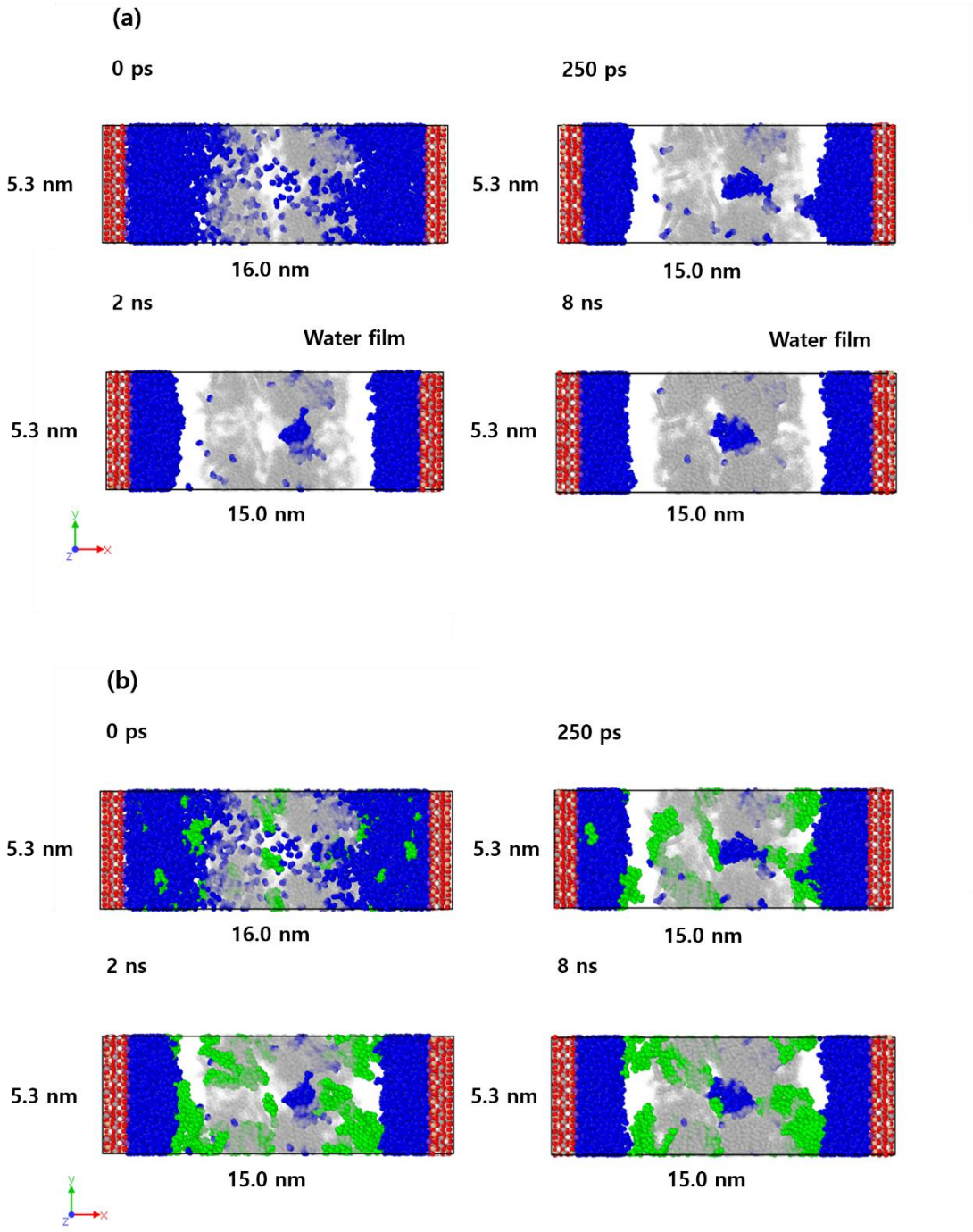
(a)
0 ps
250 ps
5.3 nm
5.3 nm
16.0 nm
15.0 nm
2 ns
8 ns
Water film
Water film
5.3 nm
5.3 nm
15.0 nm
15.0 nm
(b)
0 ps
250 ps
5.3 nm
5.3 nm
16.0 nm
15.0 nm
2 ns
8 ns
5.3 nm
5.3 nm
15.0 nm
15.0 nm

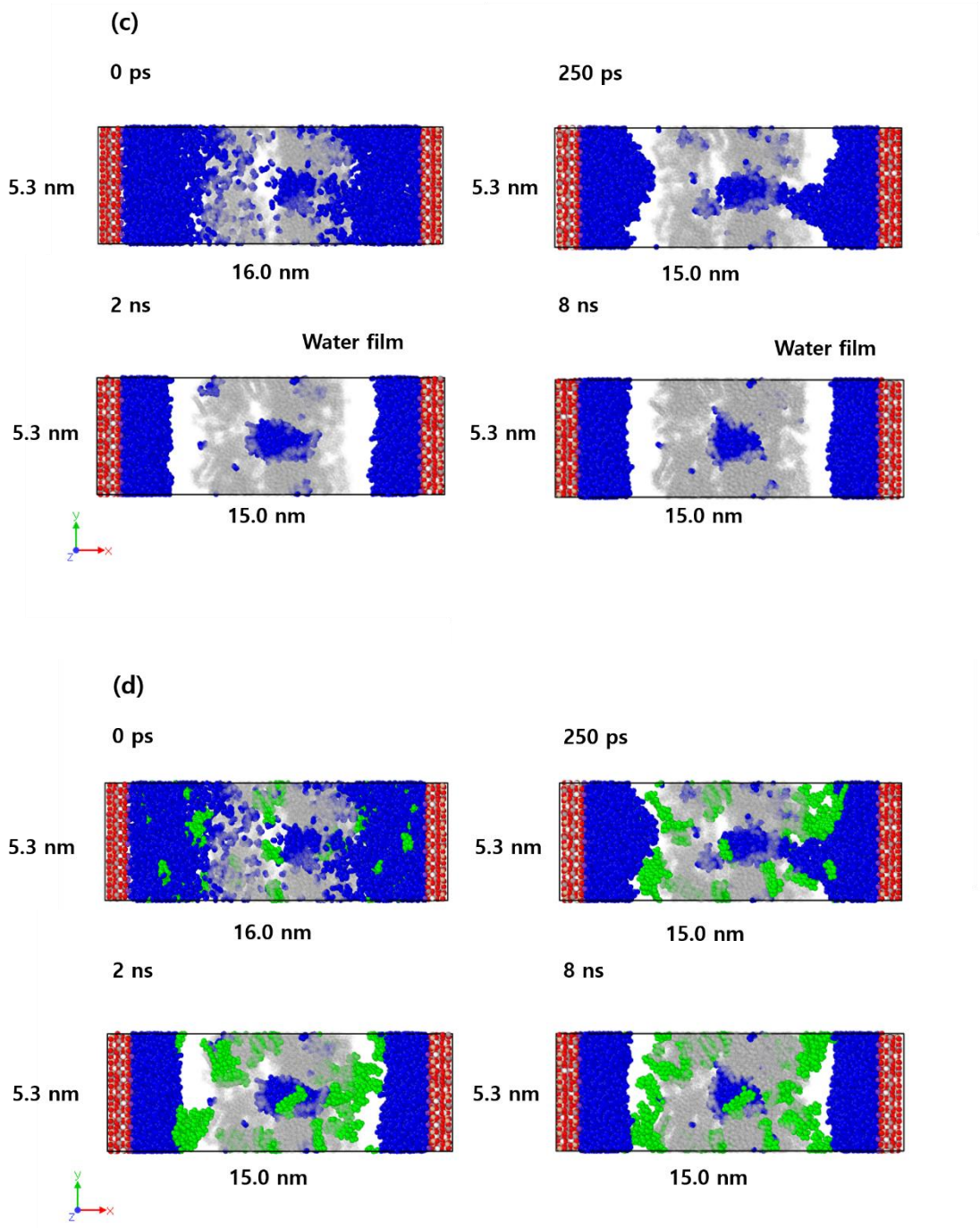

Figure 3.9. Distribution of asphaltene/resin and water molecules in the simulation box with P-P pores at 80% of water concentration. (a) shows the formation of water films over time in the case where no water is present in kerogen. (b) shows the asphaltene/resin fraction predominantly

adsorbed on kerogen with no initial water in kerogen. (c) shows the formation of water films in the presence of water in kerogen. (d) shows the asphaltene/resin fraction predominantly adsorbed on kerogen with some initial water in kerogen. The color code is assigned as follows: water (blue), asphaltene/resins (green), kerogen (gray), and illite (other colors).

CHAPTER 4. EFFECT OF SALINITY ON HYDROCARBON DISTRIBUTION IN MIXED-WET PORES

In previous sections, I discussed the distribution of pure water and hydrocarbons in a system with kerogen and clay surfaces. I demonstrated the sensitivity of fluid distribution to the clay surface chemistry as well as the concentration of water. The key observations were the formation of a water bridge under certain conditions from one clay surface to the other or from one clay surface to the polar constituents in kerogen. The other interesting observation is related to the affinity of the asphaltene/resin fraction to water/clay surface because of hydrogen bonding. This affinity reduces the hydrophilicity of the clay surface and the region between the clay and kerogen surfaces becomes more hydrophobic than mixed-wet.

However pure water is a rare occurrence in nature necessitating modification of the work documented in previous chapters to account for salinity. Salinity has been shown to influence the interactions between water and rock, as well as water and hydrocarbon in the subsurface. Figure 4.1 shows an example showing the effect of salinity, called electric double layer (EDL). In the figure, cations are highly attracted to the negatively charged clay surface while anions are gradually repelled by the surface charge of the clay mineral. The water film formed by the ions adjacent to the clay surface interrupts interaction between oil and clay minerals. The formation of the EDL thus improves hydrocarbon recovery by generating the hydrophilic surface. (Lee et al., 2010; Brady et al., 2015; Underwood et al., 2015; Chen et al., 2018).

In this work, I consider the effect of salinity on water and hydrocarbon fluid distribution in mixed-wet pore systems with different clay surfaces. The base model has 50% water concentration. I consider four different salinities (10,000 ppm, 20,000 ppm, 40,000 ppm, and 100,000 ppm). Several studies consider salinities in the range of 100,000 ppm when characterizing formation

brine (Brady et al., 2016; Jahediesfanjania et al., 2019; Sun et al., 2019) and this is the upper limit of salinity considered in this study. While other lower values (~10000 ppm) are not very common, it is instructive to assess the impact of moderate salinity values on the behavior of water and hydrocarbon in mixed-wet pore systems.

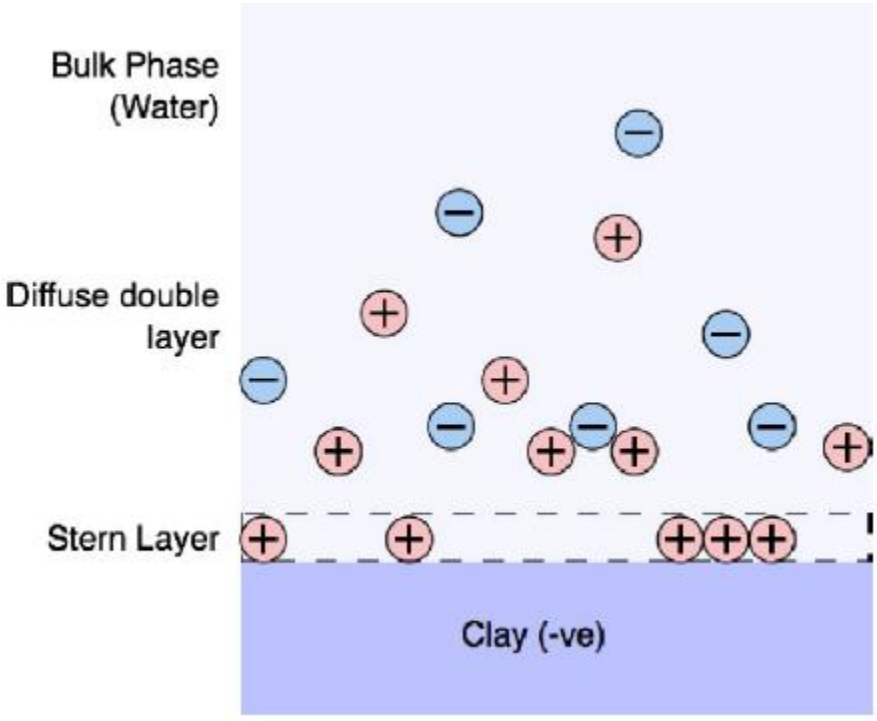

Figure 4.1. Gouy−Chapman−Stern model representing electric double layer on clay surface (Underwood et al., 2015).

4.1 Distribution of Na^+ and Cl^- Ions, Water and Hydrocarbons in Mixed-Wet Pores with H-P Clay Surfaces.

In this section, I describe the equilibrium distribution of salt ions, water and hydrocarbon in the simulation box at various salinities. Figure 4.2a shows the distribution of Na^+ and Cl^- at various salinity levels for the simulation box with H-P clay surfaces. As mentioned earlier, the water concentration is 50% and the figure does not show any water or hydrocarbons for clarity. Figure 4.2b shows the density of the Na^+ and Cl^- ions from the left to the right of the pore with prominent peaks adjacent to the clay surfaces indicating strong adsorption. There are additional peaks in the center of the pore and an examination of Figure 4.2c shows that these occur where water droplets are present.

At low salinity levels (10,000 and 20,000 ppm), Na^+ is predominantly adsorbed to the hydroxyl surface while Cl^- shows an affinity to the potassium surface. A few counterions are also present adjacent to the Na^+ and Cl^- layers. At higher salinity levels (40,000 and 100,000 ppm), in addition to the counterions adsorbed to the clay surfaces, the number of the ions screening the counterions adjacent to the clay surfaces increases dramatically as seen in Figure 4.2a.

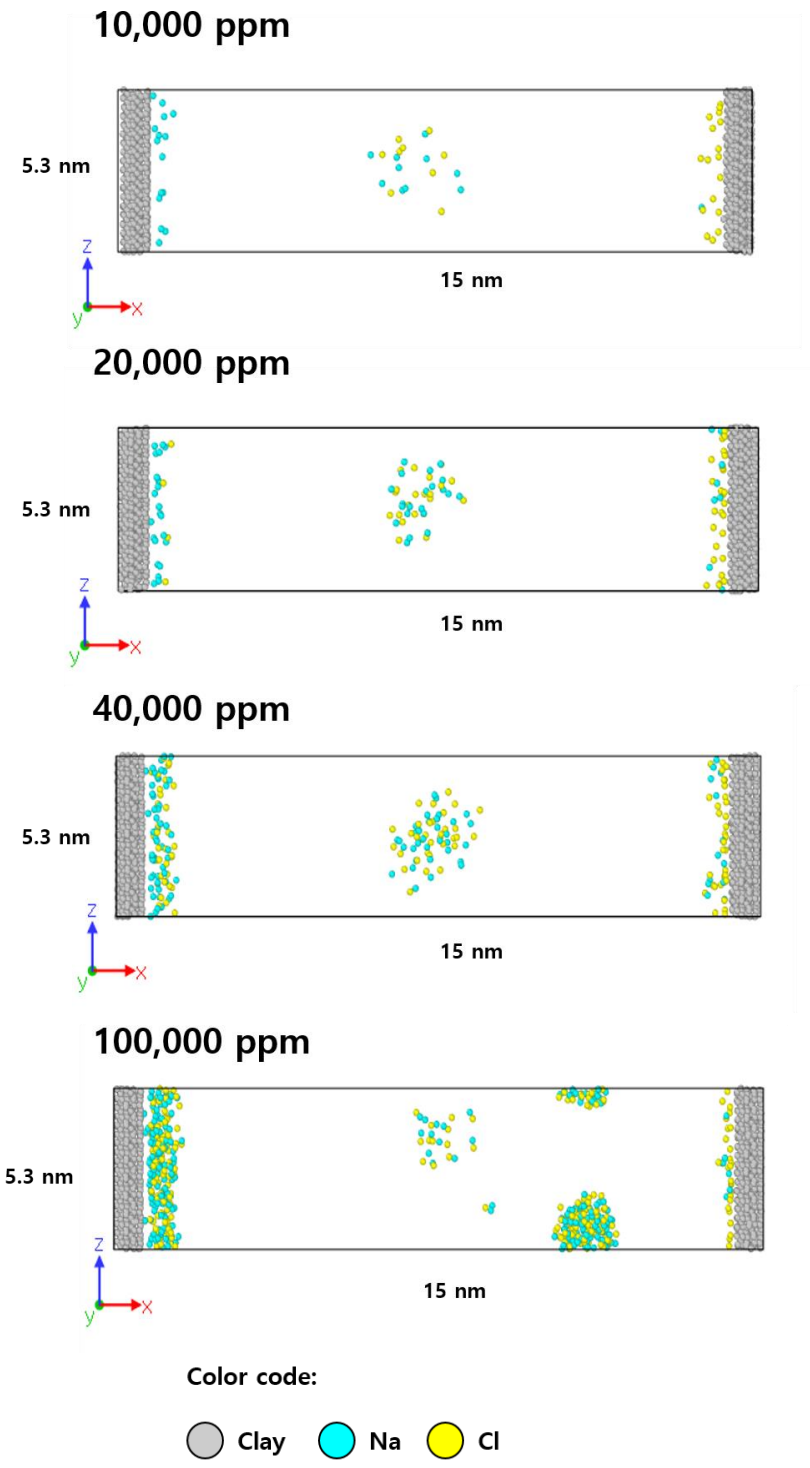

(a) Spatial distribution of ions at various salinity levels. Kerogen, water and hydrocarbon molecules are not shown for clarity.

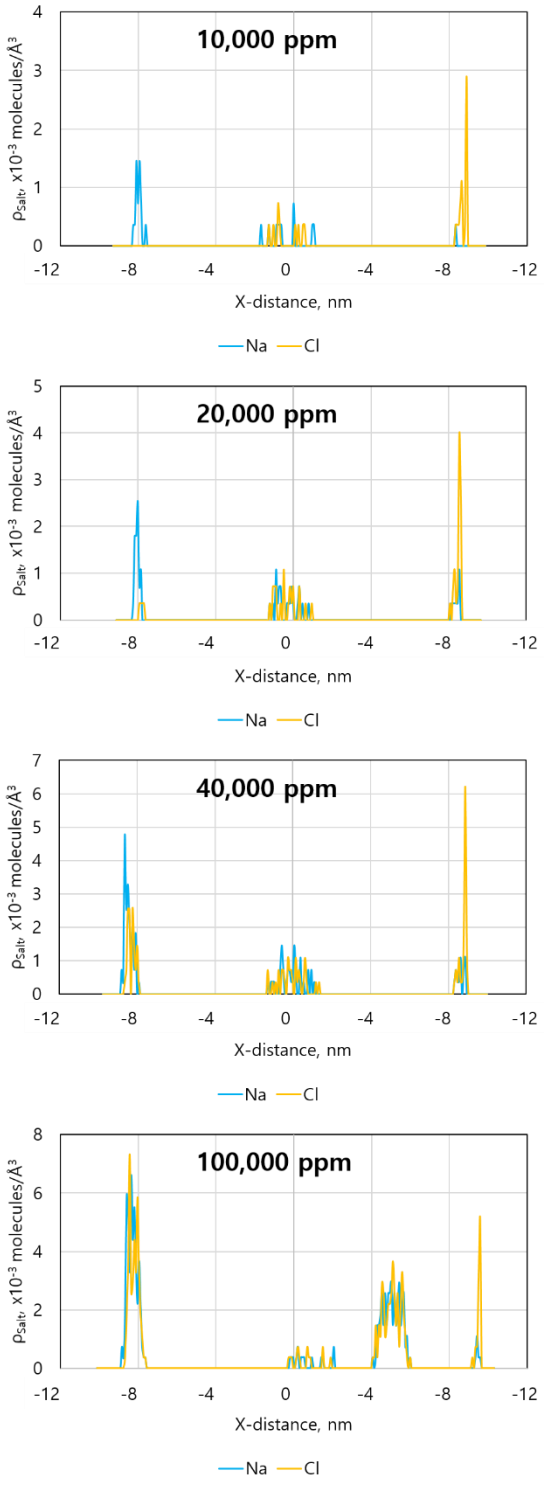

(b) Number density profiles of ions at various salinity levels.

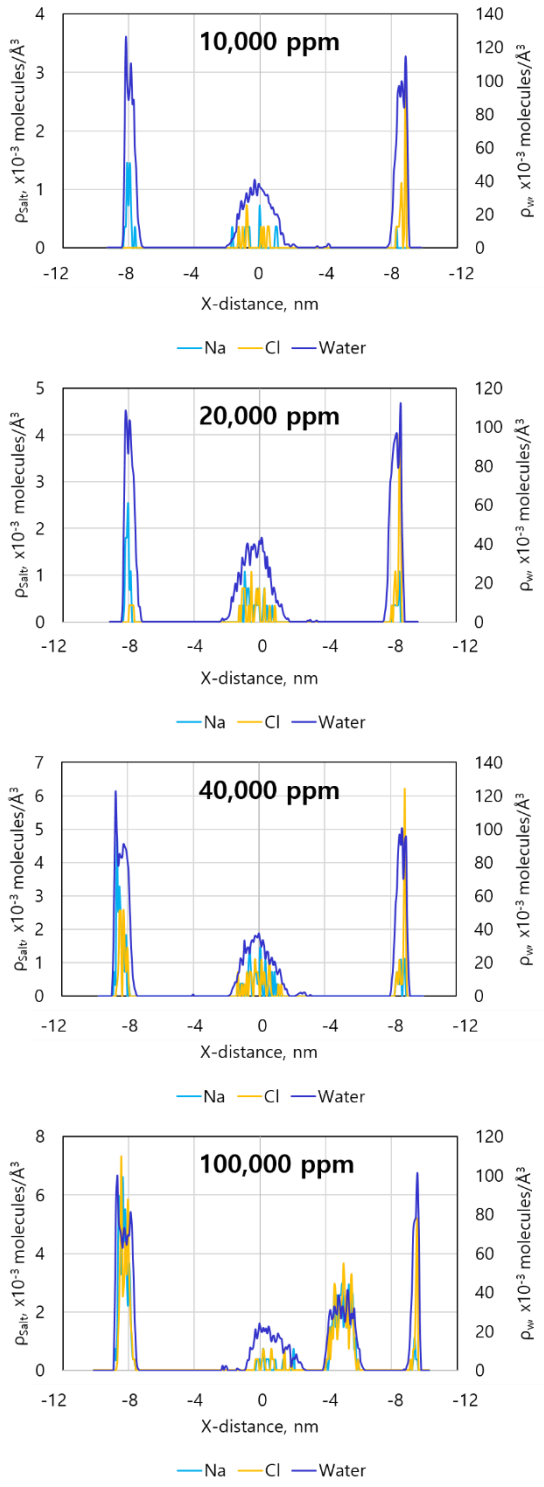

(c) Number density profiles of ions and water at various salinity levels

Figure 4.2. Distribution analysis of ions and water molecules at various salinity levels in the simulation box with H-P clay surfaces.

Figure 4.3 shows the distribution of water in the simulation box with H-P clay surfaces for different salinity levels. An important point to mention here is that with pure water, I observe the formation of a water bridge as seen in previous chapters in Figures 3.1, 3.3, 3.4, and 3.5. In Figure 4.3, it is quite apparent that under similar conditions, there is no water bridge. The presence of salt has been shown to dissipate the water bridge because dissolved salt ions diminish the strength of the local, intra-pore electric field caused by the oppositely charged clay surfaces (Xiong et al. 2020b). Water is largely seen to be adsorbed or present as droplets within the pore spaces.

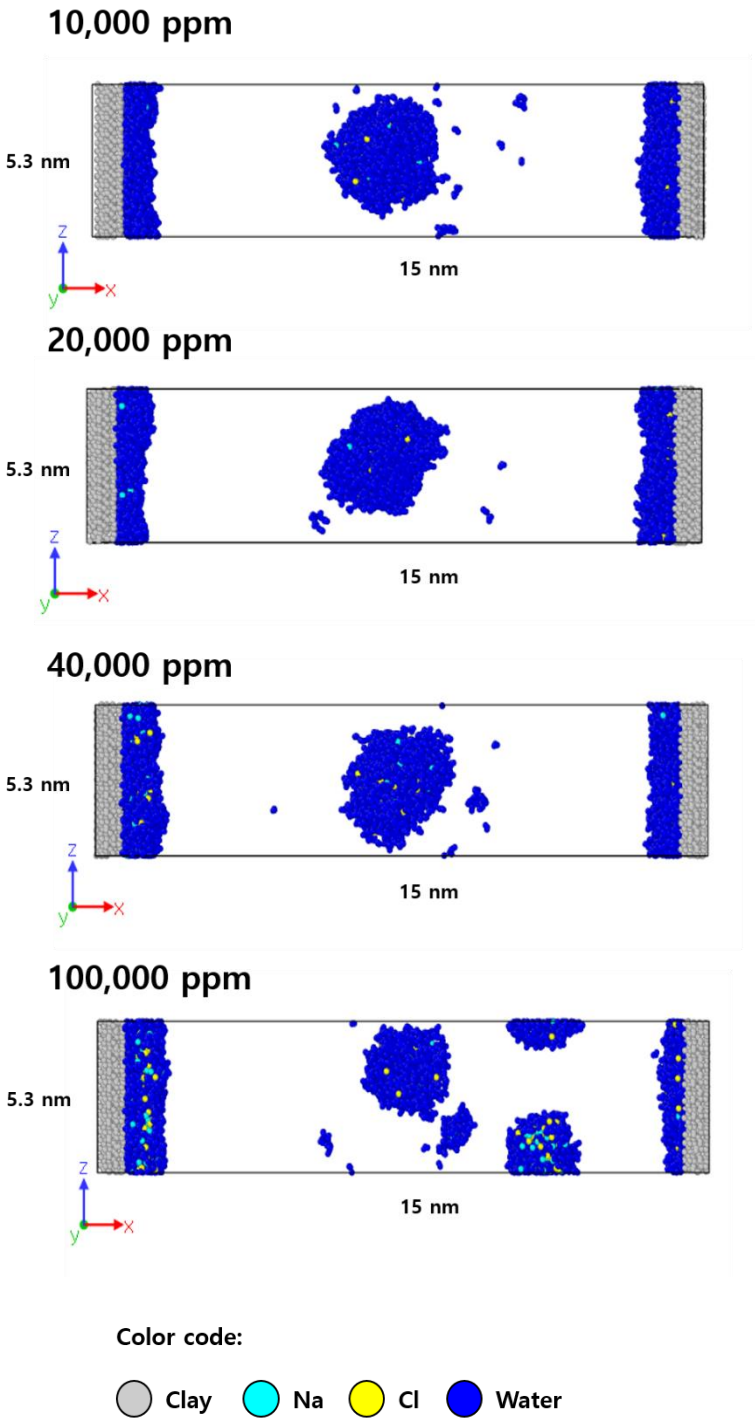

Figure 4.3. Spatial distribution of ions and water molecules at various salinity levels in the simulation box with H-P clay surfaces. Kerogen and hydrocarbon molecules are not shown for clarity.

Figure 4.4 shows the distribution of the asphaltene/resin fraction in the system with H-P clay surfaces, along with water and the ions. Regardless of the different salinity levels, the snapshots indicate that some of the asphaltene/resin fraction is attracted to the water film adsorbed to the clay surfaces by hydrogen bonding between water and polar resin part while a significant number are also adsorbed to kerogen surfaces. I observe here that irrespective of the salinity, the attraction of the heavier hydrocarbon species to the clay surfaces reduces the hydrophilicity of clay minerals. This also has the effect of reducing the degree of mixed wettability in these pores. This phenomenon should not be overlooked in analyzing hydrocarbon storage and flow in spatially heterogeneous shale reservoirs.

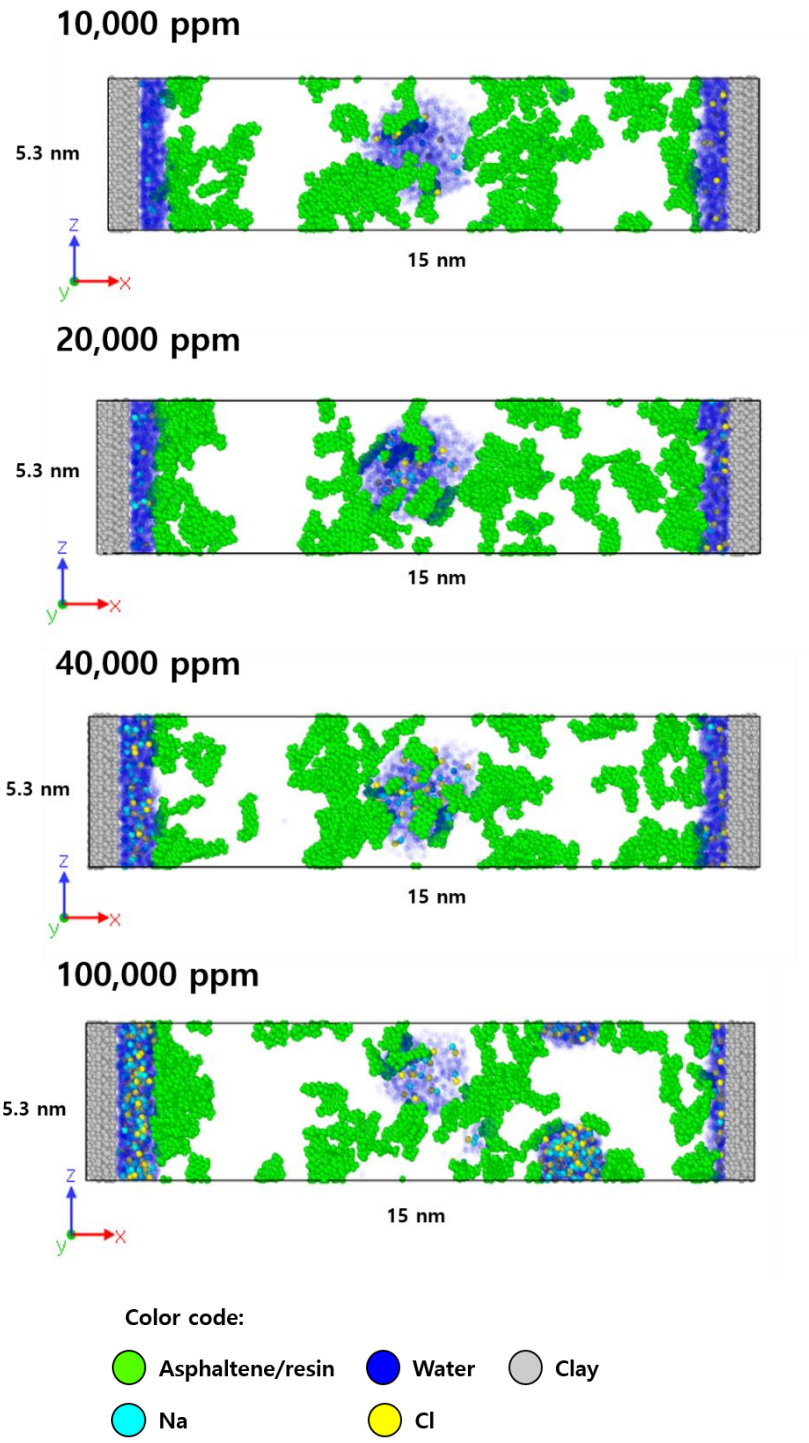

Figure 4.4. Spatial distribution of water and asphaltene/resin molecules in the simulation box with H-P clay surfaces. Kerogen and other hydrocarbon molecules are not shown for clarity.

For a few of the simulation studies (at 10,000 and 100,000 ppm in Figure 4.2a), we observe the salt ions distributed vertically across the height of the simulation box. This is because of the formation of a cylindrical water pillar that results when the periodic boundary condition cause water droplets across the boundary to merge. Figure 4.5 displays the formation procedure of cylindrical water pillar I describe. This is only an artefact of the simulation and unlikely to occur in nature.

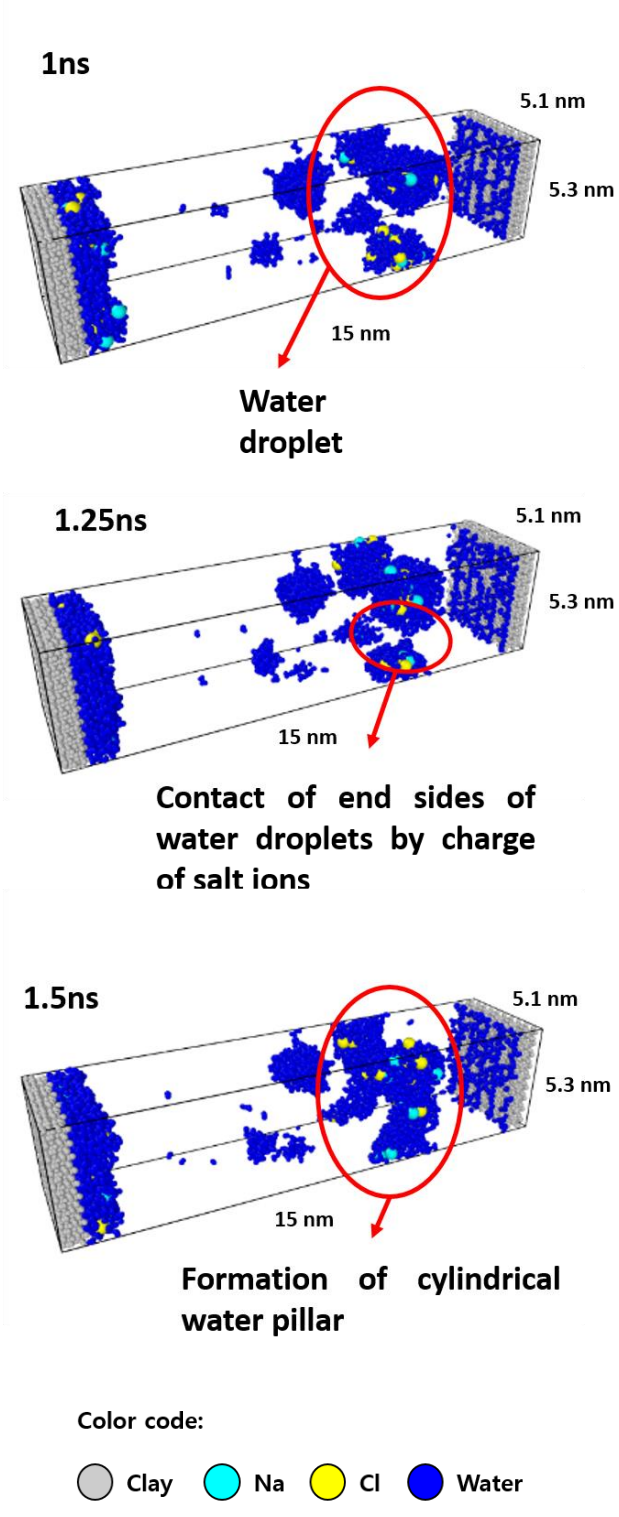

Figure 4.5. Formation of cylindrical water pillar at 10,000 ppm brine over several simulation snapshots. Kerogen and hydrocarbons molecules are not shown for clarity.

4.2 Distribution of Na^+ and Cl^- Ions, Water and Hydrocarbons in Mixed-Wet Pores with P-P Clay Surfaces.

Figure 4.6 shows water and ions distribution in the simulation box with P-P clay surfaces. At low brine salinities (10,000 and 20,000 ppm) with P-P clay surfaces, we observe similar behavior as in the H-P clay surfaces. A few of the salt ions are attracted to either face of the clay surfaces. At higher salinity levels (40,000 and 100,000 ppm), the ions mostly reside within the water droplets as seen in Figure 4.6a. Very little adsorption of the ions is observed.

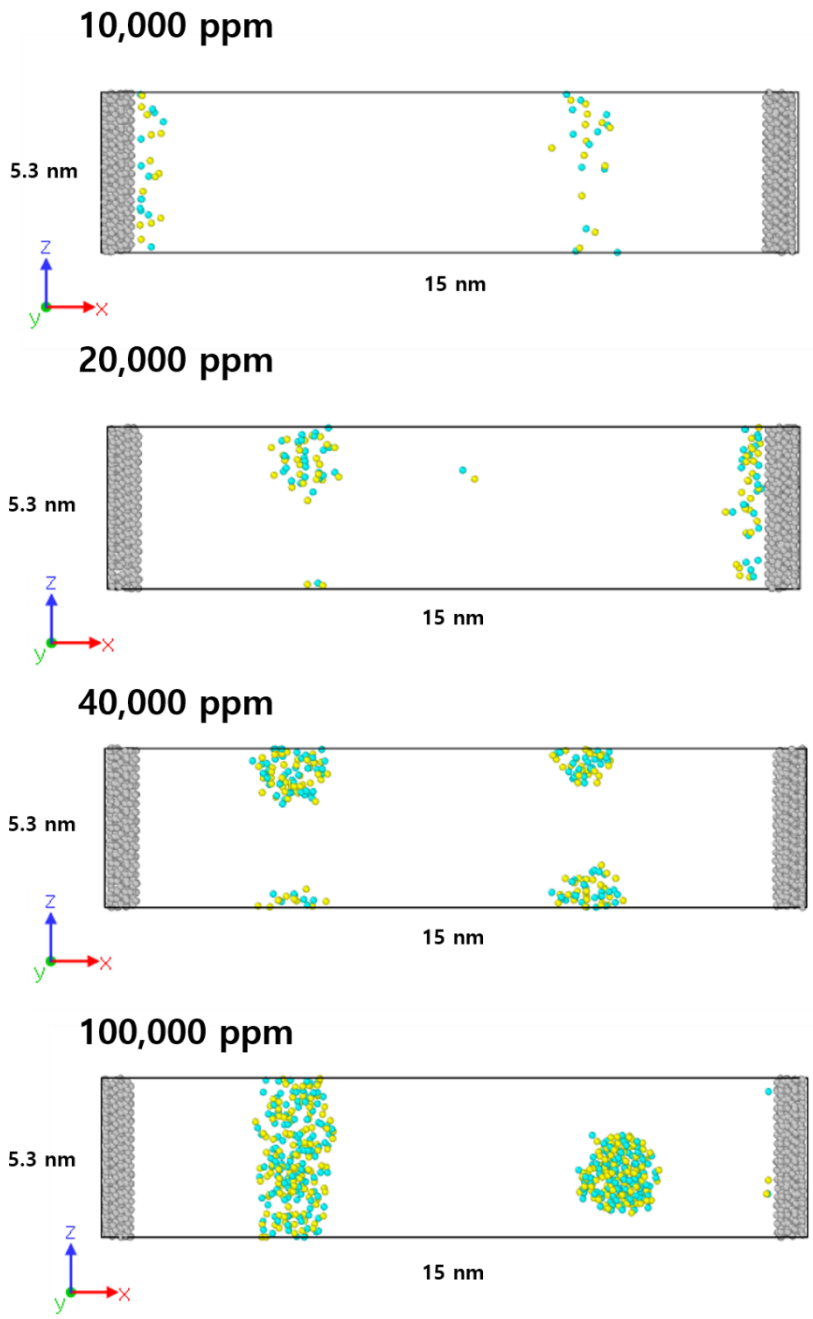

(a) Spatial distribution of ions at various salinity levels. Kerogen, water and hydrocarbon molecules are not shown for clarity.

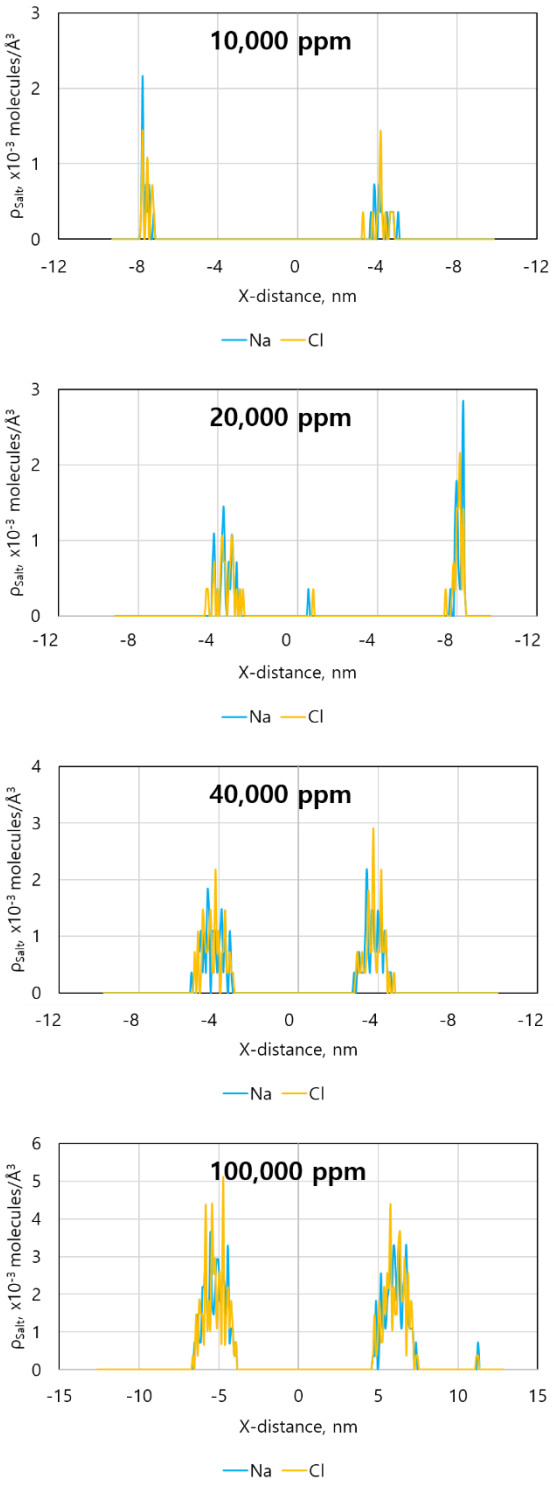

(b) Number density profiles of ions at various salinity levels

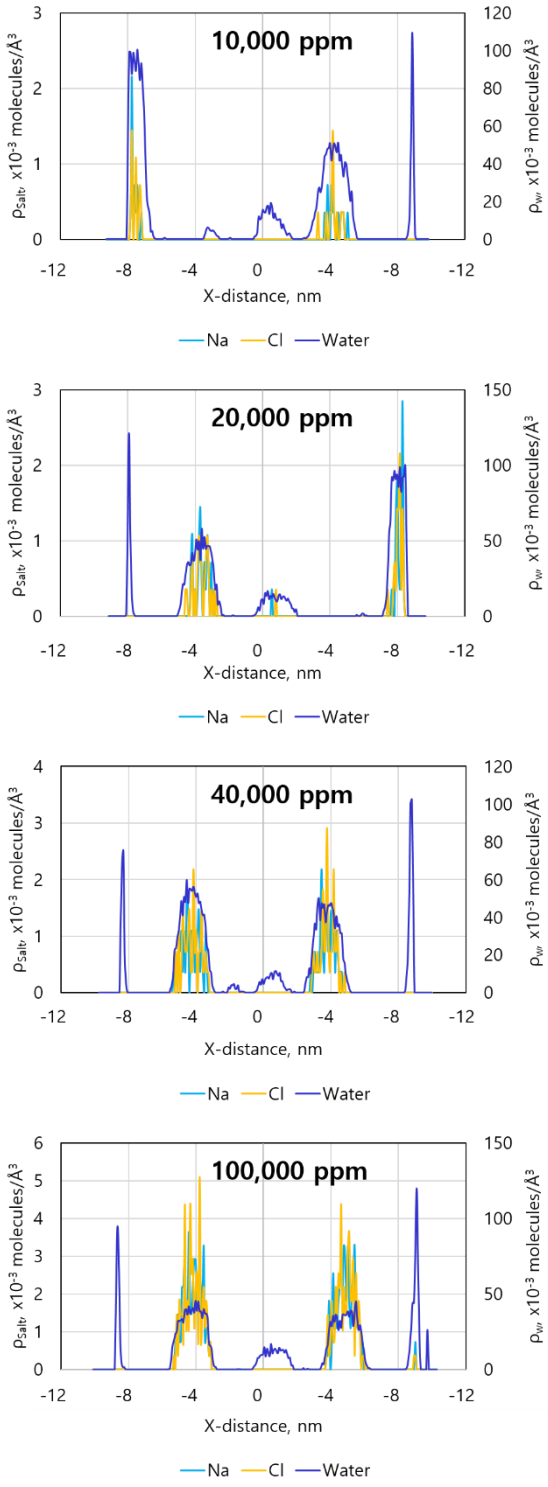

(c) Number density profiles of ions and water at various salinity levels

Figure 4.6. Distribution analysis of ions and water molecules at various salinity levels in the simulation box with P-P clay surfaces.

Figure 4.7 shows the distribution of water in the simulation box with P-P clay surfaces for different salinity levels. With pure water, as shown in Figures 3.8 and 3.9, water molecules adjacent to the charged clay surface form water films by hydrophilic attraction. At low salinity levels (10,000 and 20,000 ppm), water films are seen to form on the clay surfaces with a few water droplets within the pore spaces. We do not observe proportionally higher adsorption at higher salinity levels (40,000 and 100,000 ppm). The large number of salt ions combined with water form stable, large droplets with little adsorption. Figure 4.8 shows the distribution of asphaltene/resin molecules in the system with P-P clay surfaces. The simulation results indicate that a few of the heavier molecules are adjacent to the adsorbed water film and the remaining molecules are adsorbed on the kerogen surfaces.

This chapter provides more realistic observation of hydrocarbon storage in mixed-wet shale pores by considering brine at different salinity levels. Salinity of the brine promotes movement of the salt ions adjacent to the clays, forming water films dissolving the ions. At lower salinity levels, prior studies have shown that the hydrophilicity of clay surfaces is reinforced (Lee et al., 2010; Nasralla et al., 2011; Chen et al., 2018). I do not observe this phenomenon. I observe the attraction of asphaltene/resin fraction to the water films on clay surfaces which reduces the hydrophilicity of clay surfaces, regardless of salinity levels.

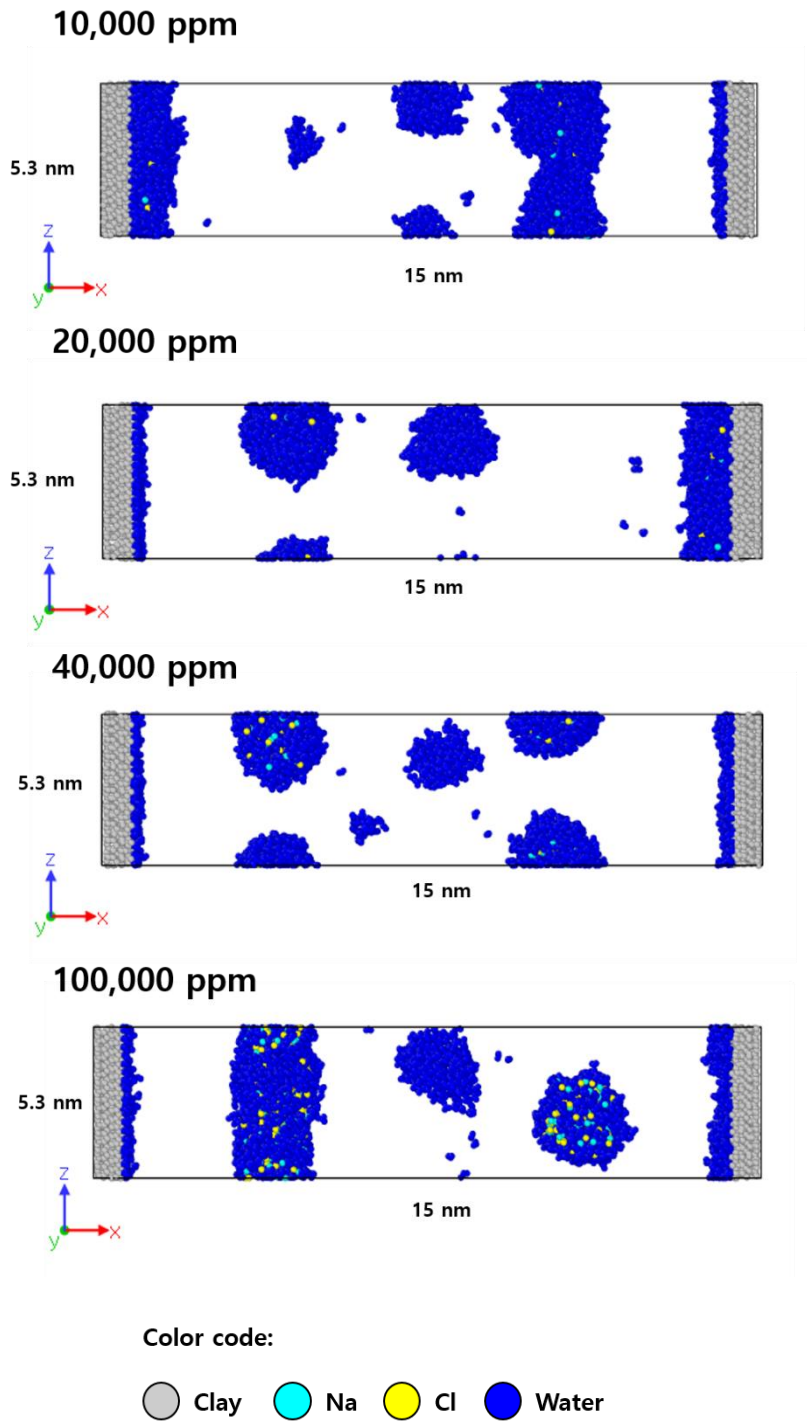

Figure 4.7. Spatial distribution of ions and water molecules at various salinity levels in the simulation box with P-P clay surfaces. Kerogen and hydrocarbon molecules are not shown for clarity.

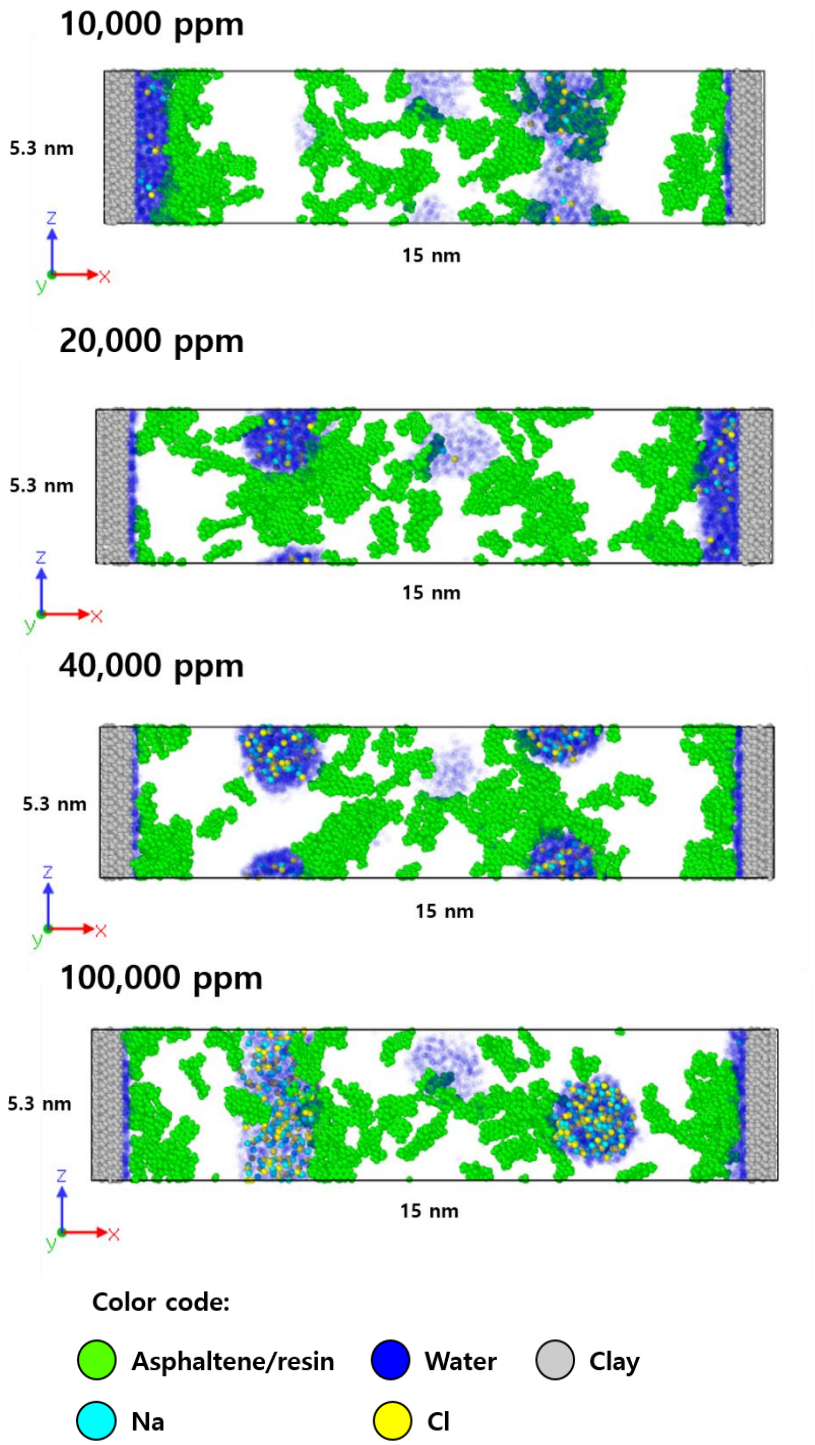

Figure 4.8. Spatial distribution of water and asphaltene/resin molecules in the simulation box with P-P clay surfaces. Kerogen and other hydrocarbon molecules are not shown for clarity.

CHAPTER 5. CONCLUSIONS

In this study, I constructed a molecular model of a mixed-wet pore by placing kerogen in between two opposing clay surfaces. The pore spaces were filled with a mixture of water and hydrocarbons in order to study the distribution of various hydrocarbon components and water in the system. I also evaluated the impact of salinity on fluid distribution. The following are the conclusions that can be drawn from this study:

- The computation of fluid-fluid and solid-fluid molecular interactions indicate that the heavy components have a strong affinity towards the organic surfaces and water has a strong affinity towards the clay surfaces, as expected. However, the polar constituents of the asphaltene/resin fraction also show an affinity towards water and the clay surfaces due to electrostatic interactions.
- Throughout the study, irrespective of the salinity levels or the surface charge on the clay surface, a fraction of the asphaltene/resin molecules adhere to the adsorbed water layer. This creates conditions where the clay surface is oil-wetting instead of water-wetting because of the adsorption of the asphaltene/resin fraction.
- With pure water in the mixed-wet pore system, water is seen to occur in the form of water bridges and as an adsorbed phase. With even moderate salinity, water is only seen to be adsorbed. It is unlikely that water bridges will occur naturally unless the formation water is extremely fresh.
- With H-P clay surfaces, salt ions are seen to be adsorbed on to the clay surface. This has the effect of enhancing the hydrophilicity of the clay. With P-P clay surfaces, we do not see

appreciable adsorption of the salt. Instead, the salt is dissolved in water droplets within the pore spaces. Very little water is adsorbed.

REFERENCES

Accelrys, (2016). Materials Studio. http://accelrys.com/products/collaborative-science/biovia-materials-studio/.

Alharthy, N.S., Weldu, T., Teklu, W., Nguyen, T.N., Kazemi, H., and Graves, R.M. (2016). Nanopore Compositional Modeling in Unconventional Shale Reservoirs. *SPE Reservoir Evaluation & Engineering* 19 (3), 415-428. SPE-166306-PA.

Allen, M. P. and D. J. Tildesley (2017). *Computer Simulation of Liquids* (Second ed.). Oxford University Press.

Ambrose, R.J., Hartman, R.C., Diaz-Compos, M., Akkutlu, I.Y., and Sondergeld, C.H., (2012). Shale Gas-In-Place Calculations Part I: New Pore-Scale Considerations. *SPE Journal* 17 (1), 219-229.

Baek, S. and Akkutlu, Y.I., (2019). Produced-Fluid Composition Redistribution in Source Rocks for Hydrocarbon-In-Place and Thermodynamic Recovery Calculations. *SPE Journal* 24 (3), 1395-1414. SPE-195578-PA.

Berendsen, H.J.C., Postma, J.P.M., van Gunsteren, W.F., and Hermans, J., (1981). *Interaction Models for Water in Relation to Protein Hydration*. In: Pullman B, editor. Intermolecular Forces: Proceedings of the Fourteenth Jerusalem Symposium on Quantum Chemistry and Biochemistry. Reidel Publishing Company, Dordrecht, Netherlands, 14, 331–342.

Blatt, H. and R.J. Tracy (1996). *Petrology: Igneous, Sedimentary and Metamorphic*, (Second ed.). Macmillan.

Bogue, R., 2011. Nanoscale Fabrication: Techniques, Limitations and Future Prospects. *Assembly Automation* 31 (4), 304–308.

Bourg, I.C. and Steefel, C.I., (2012). Molecular Dynamics Simulations of Water Structure and Diffusion in Silica Nanopores. *Journal of Physical Chemistry C* 116 (21), 11556-11564.

Brady, P.V., Morrow, N.R., Fogden, A., Deniz, V., and Loahardjo, N., and Winoto, (2015). Electrostatics and the Low Salinity Effect in Sandstone Reservoirs. *Energy Fuels* 29 (2), 666−677.

Brady, P.V., Bryan, C.R., Thyne, G., and Li, H., (2016). Altering Wettability to Recover More Oil from Tight Formations. *Journal of Unconventional Oil and Gas Resources* 15, 79-83.

Bui, K., Akkutlu, I.Y., Zelenev, A., and Hill, W.A., 2018. Kerogen Maturation Effects on Pore Morphology and Enhanced Shale Oil Recovery. In *SPE Europec featured at 80th EAGE Conference and Exhibition*, 11-14 June, Copenhagen, Denmark. Society of Petroleum Engineers. SPE-190818-MS.

Chalmers, G.R.L. and Bustin, R.M., (2007). The Organic Matter Distribution and Methane Capacity of the Lower Cretaceous Strata of Northeastern British Columbia, Canada. *International Journal of Coal Geology* 70 (1–3), 223-239.

Chen, Y., Xie, Q., Sari, A., Brady, P.V., and Saeedi, A., (2018). Oil/Water/Rock Wettability: Influencing Factors and Implications for Low Salinity Water Flooding in Carbonate Reservoirs. *Fuel* 215, 171−177.

Collell, J., Ungerer, P., Galliero, G., Yiannourakou, M., Montel, F., and Pujol, M., (2014a). Molecular Simulation of Bulk Organic Matter in Type II Shales in the Middle of the Oil Formation Window. *Energy Fuels* 28 (12), 7457-7466.

Collell, J., Galliero, G., Gouth, F., Montel, F., Pujol, M., Ungerer, P., and Yiannourakou, M., (2014b). Molecular Simulation and Modelisation of Methane/Ethane Mixtures Adsorption onto

a Microporous Molecular Model of Kerogen under Typical Reservoir Conditions. *Microporous and Mesoporous Materials* 197, 194−203.

Cornell, W.D., Cieplak, P., Bayly, C.I., Gould, I.R., Merz, K.M., Ferguson, D.M., Spellmeyer, D.C., Fox, T., Caldwell, J.W., Kollman, P.A., (1995). A Second Generation Force Field for the Simulation of Proteins, Nucleic Acids, and Organic Molecules. *Journal of the American Chemical Society* 117 (19), 5179-5197.

Curtis M.E., Ambrose, R.J., Sondengeld, C.H., and Rai, C.S. (2010). Structural Characterization of Gas Shales on the Micro- and Nano-Scales. In *Canadian Unconventional Resources and International Petroleum Conference*, 19-21 October, Calgary, Alberta, Canada. Society of Petroleum Engineers. SPE-137693-MS.

Cygan, R.T., Liang, J.J., and Kalinichev, A.G., (2004). Molecular Models of Hydroxide, Oxyhydroxide, and Clay Phases and the Development of a General Force Field. *Journal of Physical Chemistry B* 108 (4), 1255−1266.

Cygan, R.T., Romanov, V.N., and Myshakin, E.M., (2012). Molecular Simulation of Carbon Dioxide Capture by Montmorillonite Using An Accurate and Flexible Force Field. *Journal of Physical Chemistry C*, 116 (24), 13079–13091.

Dang, S.T., Sondergeld, C.H., and Rai, C.S., (2016). A New Approach to Measuring Organic Density. *Petrophysics* 57 (2), 112-120.

Dang, S.T., (2019). *Understanding Fundamental Drive Mechanisms of Huff-N-Puff EOR in Tight Formation*. PhD Dissertaion, University of Oklahoma.

Dauber-Osguthorpe, P., Roberts, V.A., Osguthorpe, D.J., Wolff, J., Genest, M., and Hagler, A.T., (1988). Structure and Energetics of Ligand Binding to Proteins: Escherichia Coli Dihydrofolate

Reductase-Trimethorprim, a Drug-Receptor System. Proteins: Structure, *Function and Bioinformatics* 4 (1), 31–47.

Desiraju, G.R. and Steiner, T. (2001). *The Weak Hydrogen Bond: In Structural Chemistry and Biology (International Union of Crystallography Monographs on Crystallography)*, Oxford University Press.

Devegowda, D., Sapmanee, K., Civan, F., Sigal, R.F., (2012). Phase Behavior of Gas Condensates in Shales Due to Pore Proximity Effects: Implications for Transport, Reserves and Well Productivity. In *SPE Annual Technical Conference and Exhibition*, 8-10 October, San Antonio, Texas, USA. Society of Petroleum Engineers. SPE-160099-MS.

Didar, B.R. and Akkutlu, I.Y., (2013). Pore-size Dependence of Fluid Phase Behavior and Properties in Organic-Rich Shale Reservoirs. In *SPE International Symposium on Oilfield Chemistry*, 8-10 April, The Woodlands, Texas, USA. Society of Petroleum Engineers. SPE-164099-MS.

Donaldson, E.C. and Alam, W., (2008). *Wettability*. Gulf Publishing Company

Doudrick, K., Liu, S., Mutunga, E.M., Klein, K.L., Damle, V., Varanasi, K.K., and Rykaczewski, K., 2014. Diffeerent Shades of Oxide: From Nanoscale Wetting Mechanisms to Contact Printing of Gallium-Based Liquid Metals. *Langmuir* 30 (23), 6867–6877.

Fang, C.H., Huang, Z.L., Wang, Q.Z., Zheng, D.W., and Liu, H.L., (2014). Cause and Significance of the Ultra-Low Water Saturation in Gas-Enriched Shale Reservoir. *Natural Gas Geoscience* 25 (3), 471-476.

Feng, F. and Akkutlu, Y.I., (2019). A Simple Molecular Kerogen Pore-Network Model for Transport Simulation in Condensed Phase Digital Source-Rock Physics. *Transport in Porous Media* 126, 295-315.

Ferez, P. and Devegowda, D., (2019). Spatial Distribution of Reservoir Fluids in Mature Kerogen Using Molecular Simulations. *Fuel* 235, 448-459.

Frenkel, D. and Smit, B., (2002). *Understanding Molecular Simulation (Second Ed)*. San Diego: Academic Press.

Gaudette, H.E., Eades, J.L., and Grim, R.E., (1966). The Nature of Illite. *Clays & Clay Minerals* 13, 165–166.

Galán, E. and Ferrell, R.E., (2013). Genesis of Clay Minerals. *Developments in Clay Science* 5, 83−126.

Goudie, A.S., (2004). *Encyclopedia of Geomorphology*. Psychology Press, Routledge, London.

Gray, M.R., Tykwinski, R.R., Stryker, J.M., and Tan, X., (2011). Supramolecular Assembly Model for Aggregation of Petroleum Asphaltenes. *Energy Fuels* 25 (7), 3125-3134.

Gualtieri, A.F., Ferrari, S., Leoni, M., Grathoff, G., Hugo, R., Shatnawi, M., Paglia, G., and Billinge, S., (2008). Structural Characterization of the Clay Mineral Illite-1M. *Journal of Applied Crystallography* 41, 402−415.

Haji-Akbari, N., Teeraphapkul, P., and Fogler, H.S., (2014). Effect of Asphaltene Concentration on the Aggregation and Precipitation Tendency of Asphaltenes. *Energy Fuels* 28 (2), 909–919.

Hantel, G., Brochard, L., Pellenq, R.J.M., Ulm, F.J., and Coasne B., 2017. Role of Interfaces in Elasticity and Failure of Clay−Organic Nanocomposites: Toughening upon Interface Weakening? *Langmuir* 33 (42), 11457-11466.

Hao, Y., Yuan, L., Li, P., Zhao, W., Li, D., and Lu, D., (2018). Molecular Simulations of Methane Adsorption Behavior in Illite Nanopores Considering Basal and Edge Surfaces. *Energy Fuels* 32 (4), 4783-4796.

Hassenkam, T., Skovbjerg, L., and Stipp, S., 2009. Probing the Intrinsically Oil-Wet Surfaces of Pores in North Sea Chalk at Subpore Resolution. *Proceedings of the National Academy of Sciences of the United States of America* 106 (15), 6071–6076.

Hestenes, M.R. and Stiefel, E., (1952). Methods of Conjugate Gradients for Solving Linear Systems. *Journal of Research of the National Bureau of Standards* 49 (6), 409-436.

Ho, T.A., Wang, Y., and Criscenti, L.J., (2018). Chemo-Mechanical Coupling in Kerogen Gas Adsorption/Desorption. *Physical Chemistry Chemical Physics* 20 (18), 12390−12395.

Ho, T.A. and Wang, Y., (2019). Enhancement of Oil Flow in Shale Nanopores by Manipulating Friction and Viscosity. *Physical Chemistry Chemical Physics* 21 (24), 12777-12786.

Hockney, R.W. and Eastwood, J.W., (1988). *Computer Simulation Using Particles*. CRC Press, Boca Raton, Florida, USA.

Hu, Y., Devegowda, D., and Sigal, R.F., (2014). Impact of Maturity on Kerogen Pore Wettability: A Modeling Study. In *SPE Annual Technical Conference and Exhibition*, 27-29 October, Amsterdam, The Netherlands. Society of Petroleum Engineers. SPE-170915-MS.

Jagadisan, A. and Heidari, Z., (2019). Demystifying Wettability Alteration in Kerogen as a Function of its Geochemistry and Reservoir Temperature and Pressure Using Molecular Dynamics Simulations. In *SPE Annual Technical Conference and Exhibition*, 30 September - 2 October, Calgary, Alberta, Canada. Society of Petroleum Engineers. SPE-195863-MS.

Jahediesfanjania, H., Anderson, S.T., and Warwick, P.D., (2019). Improving Pressure-Limited CO_2 Storage Capacity in Saline Formations by Means of Brine Extraction. *International Journal of Greenhouse Gas Control* 88, 299-310.

Jin, B. and Nasrabadi, H., 2017. Phase Behavior in Shale Organic and Inorganic Nanopores From Molecular Simulation. In *SPE Annual Technical Conference and Exhibition*, 9-11 October, San Antonio, Texas, USA. Society of Petroleum Engineers. SPE-187307-MS.

Jin, L., Jamili, A., Huang, L., and Perez, F., (2017). Modeling the Mechanisms of Clay Damage by Molecular Dynamic Simulation. *Geofluids* 2017, 1747068.

Jones, J.E., (1924) On the Determination of Molecular Fields. II. From the Equation of State of a Gas. *Proceedings of the Royal Society A* 106 (738), 463-477.

Joonaki, E., Buckman, J., Burgass, R., and Tohidi, B., (2019). Water versus Asphaltenes; Liquid–Liquid and Solid–Liquid Molecular Interactions Unravel the Mechanisms behind an Improved Oil Recovery Methodology. *Scientific Reports* 9, 11369.

Jorgensen, W.L., Maxwell, D.S., and Tirado-Rives, J., (1996). Development and Testing of the OPLS All-Atom Force Field on Conformational Energetics and Properties of Organic Liquids. *Journal of the American Chemical Society* 118 (45), 11225-11236.

Katti, D.R., Thapa, K.B., and Katti, K.S., (2017). Modeling Molecular Interactions of Sodium Montmorillonite Clay with 3D Kerogen Models. *Fuel* 199, 641-652.

Keffer D.J., (2002). The Working Man's Guide to Obtaining Self Diffusion Coefficients from Molecular Dynamics Simulations. Course website: Modeling and Simulation in Materials Science and Engineering: Classical Mechanics. http://utkstair.org/clausius/docs/mse614/text/notes.html. University of Tennessee, Knoxville.

Keffer, D.J. and Adhangale P., (2004). The Composition Dependence of Self and Transport Diffusivities from Molecular Dynamics Simulations. *Chemical Engineering Journal* 100 (1–3), 51–69.

Kelemen, S.R., Afeworki, M., Gorbaty, M.L., Sansone, M., Kwiatek, P.J., Walters, C.C., Freund, H., Siskin, M., Bence, A.E., Curry, D.J., Solum, M., Pugmire, R.J., Vandenbroucke, M., Leblond, M., and Behar, F., (2007). Direct Characterization of Kerogen by X-ray and Solid-State 13C Nuclear Magnetic Resonance Methods. *Energy Fuels* 21 (3), 1548-1561.

Kim, T.I., Tahk, D., and Lee, H.H., 2009. Wettability-Controllable Super Water-and Moderately Oil-Repellent Surface Fabricated by Wet Chemical Etching. *Langmuir* 25 (11), 6576–6579.

Kovscek, A., Wong, H., and Radke, C., 1993. A Pore-Level Scenario for the Development of Mixed Wettability in Oil Reservoirs. *Environmental and Energy Engineering* 39 (6), 1072–1085.

Lagache, M.H., Ungerer, P., and Boutin, A., (2004). Prediction of Thermodynamic Derivative Properties of Natural Condensate Gases at High Pressure by Monte Carlo Simulation. *Fluid Phase Equilibria* 220 (2), 211-223.

Lee, S.Y., Webb, K.J., Collins, I., Lager, A., Clarke, S., Sullivan, M., Routh, A., and Wang, X., (2010). Low Salinity Oil Recovery: Increasing Understanding of the Underlying Mechanisms. In *SPE Improved Oil Recovery Symposium*, 24-28 April, Tulsa, Oklahoma, USA. Society of Petroleum Engineers. SPE-129722-MS.

Liu, M.B. and Liu, G.R. (2015). *Particle Methods for Multi-Scale and Multi-Physics*. World Scientific.

Liu, S., Li, H., and Valkó, P.A., (2018). A Production Decline Model Based on Anomalous Diffusion Stemming From Complex Fracture Network. In *SPE/AAPG/SEG Unconventional Resources Technology Conference*, 23-25 July, Houston, Texas, USA. Society of Petroleum Engineers. URTEC-2902890-MS.

Lorentz, H.A., (1881). Ueber die Anwendung des Satzes vom Virial in der kinetischen Theorie der Gase. *Annalen der Physik* 12, 127-136.

Loucks, R.G., Reed, R.M., Ruppel, S.C., and Jarvie, D.M. (2009). Morphology, Genesis, and Distribution of Nanometer-Scale Pores in Siliceous Mudstones of the Mississippian Barnett Shale. *Journal of Sedimentary Research* 79 (12), 848–861.

Lu, Y., Zeng, L., Sari, A., Chen, Y., Jin, Y., and Xie, Q., 2019. Wetting Behavior of Shale Rocks and Its Relationship to Oil Composition. *Energy Fuels* 33 (12), 12270-12277.

Mani, S., Khabaz, F., Godbole, R.V., Hedden, R.C., and Khare, R., (2015). Structure and Hydrogen Bonding of Water in Polyacrylate Gels: Effects of Polymer Hydrophilicity and Water Concentration. *Journal of Physical Chemistry B* 119 (49), 15381–15393.

Martínez, L., Andrade, R., Birgin, E.G., and Martínez, J.M., (2009). PACKMOL: A Package for Building Initial Configurations for Molecular Dynamics Simulations. *Journal of Computational Chemistry* 30 (13), 2157–2164.

Merriman, R.J., Highley, D.E. and Cameron, D.G. (2003). *Definition and Characteristics of Very-Fine Grained Sedimentary Rocks: Clay, Mudstone, Shale and Slate*. British Geological Survey Commissioned Report, p. 20.

Mitchell, D.L. and Speight, J.G., (1973). The Solubility of Asphaltenes in Hydrocarbon Solvents. *Fuel* 52 (2), 149-152.

Mosher, K., He, J.J., Liu, Y.Y., Rupp, E., and Wilcox, J., (2013) Molecular Simulation of Methane Adsorption in Micro- and Mesoporous Carbons with Applications to Coal and Gas Shale Systems. *International Journal of Coal Geology* 109, 36−44.

Nasralla, R.A., Bataweel, M.A., and Nasr-El-Din, H.A. (2011). Investigation of Wettability Alteration by Low Salinity Water. SPE In *Offshore Europe Oil and Gas Conference and Exhibition*, 6-8 September, Aberdeen, UK. Society of Petroleum Engineers. SPE-146322-MS.

Nasralla, R.A. andNasr-El-Din, H.A. (2012). Double-Layer Expansion: Is It A Primary Mechanism of Improved Oil Recovery by Low-Salinity Waterflooding? In *SPE Improved Oil Recovery Symposium*, 14-18 April, Tulsa, Oklahoma, USA. Society of Petroleum Engineers. SPE-154334-MS.

Nosé S., (1984a). A Molecular Dynamics Method for Simulations in the Canonical Ensemble. *An International Journal at the Interface between Chemistry and Physics* 52 (2), 255–668.

Nosé, S., (1984b). A Unified Formulation of the Constant Temperature Molecular Dynamics Methods. *Journal of Chemical Physics* 81 (1), 511–519.

Nosé, S., (1991). Constant Temperature Molecular Dynamics Methods. *Progress of Theoretical Physics Supplement*, 103, 1–46.

Obliger, A., Valdenaire, P.L., Capit, N., Ulm, F.J., Pellenq, R.J.M., and Leyssale, J.M., (2018). Poroelasticity of Methane-Loaded Mature and Immature Kerogen from Molecular Simulations. *Langmuir* 34 (45), 13766−13780.

Ougier-Simonin, A., Renard, F., Boehm, C., Vidal-Gilbert, S. (2016). Microfracturing and Microporosity in Shales. *Earth-Science Review* 162, 198-226.

Pak, T., Butler, I., Geiger, S., van Dijke, M., and Sorbie, K., 2015. Droplet Fragmentation: 3D Imaging of a Previously Unidentified Pore-Scale Process during Multiphase Flow in Porous Media. *Proceedings of the National Academy of Sciences of the United States of America* 112 (7), 1947–1952.

Palmer, J.C. and Debenedetti, P.G., 2014. Recent Advances in Molecular Simulation: A Chemical Engineering Perspective. *AlChE Journal* 61 (2), 370–383.

Parrinello, M. and Rahman, A., (1981). Polymorphic Transitions in Single Crystals: A New Molecular Dynamics Method. *Journal of Applied Physics* 52 (12), 7182–7190.

Passey, Q.R., Bohacs, K., Esch, W.L., Klimentidis, R. and Sinha S. (2010). From Oil-Prone Source Rock to Gas-Producing Shale Reservoir - Geologic and Petrophysical Characterization of Unconventional Shale Gas Reservoirs. In *International Oil and Gas Conference and Exhibition in China*, 8-10 June, Beijing, China. Society of Petroleum Engineers. SPE-131350-MS.

Pathak, M., Kweon, H., Deo, M., and Huang, H., (2017). Kerogen Swelling and Confinement: Its Implication on Fluid Thermodynamic Properties in Shales. *Scientific Reports* 7, 12530.

Perez, F. and Devegowda, D., (2019). Spatial Distribution of Reservoir Fluids in Mature Kerogen Using Molecular Simulations. *Fuel* 235, 448-459.

Perez, F. and Devegowda, D., (2020). A Molecular Dynamics Study of Primary Production from Shale Organic Pores. *SPE Journal* 25 (5), 2521-2533.

Perez, F., (2020). *Production of Hydrocarbons from Organic Nanopores: A Comprehensive Study Using Molecular Simulations*. PhD Dissertaion, University of Oklahoma.

Pitakbunkate, T., Balbuena, P., Moridis, G.J., and Blasingame, T.A., 2014. Effect of Confinement on PVT Properties of Hydrocarbons in Shale Reservoirs. In *SPE Annual Technical Conference and Exhibition*, 27-29 October, Amsterdam, The Netherlands. Society of Petroleum Engineers. SPE-170685-MS.

Rae, P., Lullo, G.D., and Ahmad, A.B., (2001). Towards Environmentally-Friendly Additives for Well Completion and Stimulation Operations. In *SPE Asia Pacific Oil and Gas Conference*

and Exhibition, 17-19 April, Jakarta, Indonesia. Society of Petroleum Engineers. SPE-68651-MS.

Santos, M.S., Franco, L.F.M., Castier, M., and Economou, I.G., (2018). Molecular Dynamics Simulation of n -Alkanes and CO_2 Confined by Calcite Nanopores. *Energy Fuels* 32 (2), 1934-1941.

Sapmanee, K., (2011). *Effects of Pore Proximity on Behavior and Production Prediction of Gas/condensate*. M.S. Thesis, University of Oklahoma.

Schneider, C.A., Rasband, W.S., and Eliceiri, K.W., 2012. NIH Image to ImageJ: 25 years of Image Analysis. *Nature Methods* 9 (7), 671-675.

Sedghi, M., Piri, M., and Goual, L., 2014. Molecular Dynamics of Wetting Layer Formation and Forced Water Invasion in Angular Nanopores with Mixed Wettability. *Journal of Chemical Physics* 141, 194703.

Sedghi, M. and Goual, L., (2016). Molecular Dynamics Simulations of Asphaltene Dispersion by Limonene and PVAc Polymer During CO_2 Flooding. In *SPE International Conference and Exhibition on Formation Damage Control*, 24-26 February, Lafayette, Louisiana, USA. Society of Petroleum Engineers. SPE-179040-MS.

Shedid, S.A. and Zekri, A.Y., (2006).Formation Damage Caused by Simultaneous Sulfur and Asphaltene Deposition. *SPE Production & Operations* 21(1), 58-64.

Shi, J., Zhang, L., Li, Y. Yu, W., He, X., Liu, N., Li, X., and Wang, T. (2013). Diffusion and Flow Mechanisms of Shale Gas through Matrix Pores and Gas Production Forecasting. In *SPE Unconventional Resources Conference*, Canada, 5-7 November, Calgary, Alberta, Canada. Society of Petroleum Engineers. SPE-167226-MS.

Shirono, K. and Daiguji, H., (2007). Molecular Simulation of the Phase Behavior of Water Confined in Silica Nanopores. *Journal of Physical Chemistry C* 111 (22), 7938-7946.

Shroder, J.F., (2013). *Treatise on Geomorphology*. San Diego: Academic Press.

Singh, S.K., Sinha, A., Deo, G., and Singh, J.K., (2009). Vapor−Liquid Phase Coexistence, Critical Properties, and Surface Tension of Confined Alkanes. *Journal of Physical Chemistry C* 113 (17), 7170-7180.

Sun, H., (1998). COMPASS: An Ab Initio Force-Field Optimized for Condensed-Phase Applications Overview with Details on Alkane and Benzene Compounds. *Journal of Physical Chemistry B* 102 (38), 7338–7364.

Sun, Y., Wang, D., Tsang, C.W., Wang, L., Ok, Y.S., and Feng, Y., (2019). A Critical Review of Risks, Characteristics, and Treatment Strategies for Potentially Toxic Elements in Wastewater from Shale Gas Extraction. *Environmental International* 125, 452-469.

Tan, Z.M. and Gubbins, K.E. (1990) Adsorption in Carbon Micropores at Supercritical Temperatures. *Journal of Physical Chemistry* 94 (15), 6061–6069.

Tesson, S. and Firoozabadi, A., (2018). Methane Adsorption and Self-Diffusion in Shale Kerogen and Slit Nanopores by Molecular Simulations. *Journal of Physical Chemistry C* 122 (41), 23528−23542.

Tissot, B.P. and Welte, D.H., (1984). *Petroleum Formation and Occurrence: A New Ppproach to Oil and Gas Exploration*. Springer-Verlag Berlin Heidelberg, Berlin, Germany.

Tunega, D., Gerzabek, M.H., and Lischka, H., (2004). Ab Initio Molecular Dynamics Study of a Monomolecular Water Layer on Octahedral and Tetrahedral Kaolinite Surfaces. *Journal of Physical Chemistry B* 108 (19), 5930−5936.

Underwood, T., Erastova, V., Cubillas, P., and Greenwell, H.C., (2015). Molecular Dynamic Simulations of Montmorillonite–Organic Interactions under Varying Salinity: An Insight into Enhanced Oil Recovery. *Journal of Physical Chemistry C* 119 (13): 7282-7294.

Ungerer, P. and Lachet, V. (2006). Application of Molecular Simulation in OIl and Gas Production and Processing. *Oil and Gas Science and Technology* 61 (3), 387-403.

Ungerer, P., Collell, J., and Yiannourakou, M., (2015). Molecular Modeling of the Volumetric and Thermodynamic Properties of Kerogen: Influence of Organic Type and Maturity. *Energy Fuels* 29 (1), 91–105.

Wang, S. and Civan, F., (2005). Modeling Formation Damage by Asphaltene Deposition During Primary Oil Recovery. *Journal of Energy Resources Technology* 127 (4), 310-317.

Wang J., Kalinichev, A.G., Kirkpatrick, R.J., and Cygan, R.T., (2005). Structure, Energetics, and Dynamics of Water Adsorbed on the Muscovite (001) Surface: A Molecular Dynamics Simulation. *Journal of Physical Chemistry B* 109 (33), 15893-15905.

Wang, S., Feng, Q., Javadpour, F., Xia, T., and Li, Z., (2015a). Oil Adsorption in Shale Nanopores and Its Effect on Recoverable Oil-In-Place. *International Journal of Coal Geology* 147-148, 9-24.

Wang, S., Feng, Q., Zha, M., Lu, S., Qin, Y., Xia, T., Zhang, C., (2015b). Molecular Dynamics Simulation of Liquid Alkane Occurrence State in Pores and Slits of Shale Organic Matter. *Petroleum Exploration and Development* 42 (6), 844-851.

Wei, C. and Qin, G. (2013). Microstructure Characterization for a Shale Gas Reservoir by Combining Visualization Technique and Physical Measurement. In *SPE Unconventional Resources Conference and Exhibition-Asia Pacific*. November 11-13, Brisbane, Australia. Society of Petroleum Engineers. SPE-167610-MS.

Welch, W.R.W. and Piri, M., (2015). Molecular Dynamics Simulations of Retrograde Condensation in Nanoporous Shale. In *Unconventional Resources Technology Conference*, 20-22 July, San Antonio, Texas, USA. Society of Petroleum Engineers. URTEC-2172738-MS.

Wu, H., Chen, J., and Liu, H., (2015) Molecular Dynamics Simulations about Adsorption and Displacement of Methane in Carbon Nanochannels. *Journal of Physical Chemistry C* 119 (24), 13652–13657.

Wu, T. and Firoozabadi, A., (2019). Effect of Microstructural Flexibility on Methane Flow in Kerogen Matrix by Molecular Dynamics Simulations. *Journal of Physical Chemistry C* 123 (17), 10874-10880.

Xiong, H., Devegowda, D., and Huang, L., (2020a). Water Bridges in Clay Nanopores: Mechanisms of Formation and Impact on Hydrocarbon Transport. *Langmuir* 36 (3), 723-733.

Xiong, H., Devegowda, D., and Huang, L., (2020b). EOR in Clay-Hosted Pores: Effects of Brine Salinity, Water Saturation, Pore Surface Chemistry and Pore Width. In *SPE/AAPG/SEG Unconventional Resources Technology Conference*, 20-22 July, Virtual. Society of Petroleum Engineers. URTEC-2020-2911-MS.

Yang, Z. and Guo, T., (1997). Review: Asphaltene Deposition in Oil Production and Processing. *Petroleum Exploration and Development* 24 (5), 98-103.

Yang, L., Zhou, X., Zhang, K., Zeng, F., and Wang, Z., (2018). Investigation of Dynamical Properties of Methane in Slit-Like Quartz Pores Using Molecular Simulation. *RSC Advances* 8 (59), 33798-33816.

Yaseen, S. and Mansoori, G.A., (2017). Molecular Dynamics Studies of Interaction between Asphaltenes and Solvent. *Journal of Petroleum Science and Engineering* 156, 118-124.

Yaseen, S. and Mansoori, G.A., (2018). Asphaltene Aggregation due to Waterflooding (A Molecular Dynamics Study). *Journal of Petroleum Science and Engineering* 170, 177–183.

Yu, Z., Chen, L., Wu, W., Ge, H., and Chou, S.Y., 2003. Fabrication of Nanoscale Gratings with Reduced Line Edge Roughness Using Nanoimprint Lithography. *Journal of Vacuum Science & Technology B* 21 (5), 2089–2092.

Yu, H., Fan, J.C., Xia, J., Liu, H., and We, H., 2019. Multiscale Gas Transport Behavior in Heterogeneous Shale Matrix Consisting of Organic and Inorganic Nanopores. *Journal of Natural Gas Science and Engineering* 75, 103139.

Zeng, L., Chen, Y., Hossain, M.M., Saeedi, A., and Xie, Q., (2019). Wettability Alteration Induced Water Uptake in Shale Oil Reservoirs: A Geochemical Interpretation for Oil-Brine-OM Interaction during Hydraulic Fracturing. *International Journal of Coal Geology* 213, 103277.

Zhan, S., Su, Y., Jin, Z., Wang, W., Wang, and Li, L., (2020). Oil-Water Two-Phase Flow Behavior in Shale Inorganic Nanopores: From Molecule Level to Theoretical Mathematical Model. In *SPE/AAPG/SEG Unconventional Resources Technology Conference*, 20-22 July, Virtual. Society of Petroleum Engineers. URTEC-2020-3330-MS.

Zhang, L., Lu, X., Liu, X., Yang, K., and Zhou, H., (2016). Surface Wettability of Basal Surfaces of Clay Minerals: Insights from Molecular Dynamics Simulation. *Energy Fuels* 30 (1), 149-160.

Zhang, B., Kang, J., Kang, T., Kang, G., and Zhao, G., (2019). Molecular Dynamics Simulations of CH4 Diffusion in Kaolinite: Influence of Water Content. *International Journal of Coal Science & Technology* 6 (8), 556-563.

Zhang, Q., Wang, W.D., Kade, Y., Wang, B.T., and Xiong, L., (2020). Analysis of Gas Transport Behavior in Organic and Inorganic Nanopores based on a Unified Apparent Gas Permeability Model. *Petroleum Science* 17, 168–181.

Zhao, H., Liu, C., Jiang, S., and Ge, Y., (2019). Molecular Dynamics Simulation of Water Molecules Adsorption by Different Cations based Montmorillonite. *Scientia Sinica Technologica* 49 (6), 703-715.

Zhu, X. and Zhao, Y.P. (2014). Atomic Mechanisms and Equation of State of Methane Adsorption in Carbon Nanopores. *Journal of Physical Chemistry C* 118 (31), 17737-17744.